APPLAuSE

review letters

Neutronics Simulations for new channel in DEMO's blanket

Investigation of fluctuations coupling during density ramp in AUG

A review of the MARTe control framework

Carbon monoxide electron-neutral scattering cross sections

Magnetic Control for Tokamak Plasma Position: Modeling, Instrumentation and Control Techniques

Update of the IPFN High-temperature Spectral database for CO_2

Edge instabilities between ELMs at JET

Alfvén waves in magnetized plasmas: the bounce drift resonance

Wave and particle spectra of subrelativistic magnetized collisionless shocks

Complete characterization of L2I laser system ultra short pulse

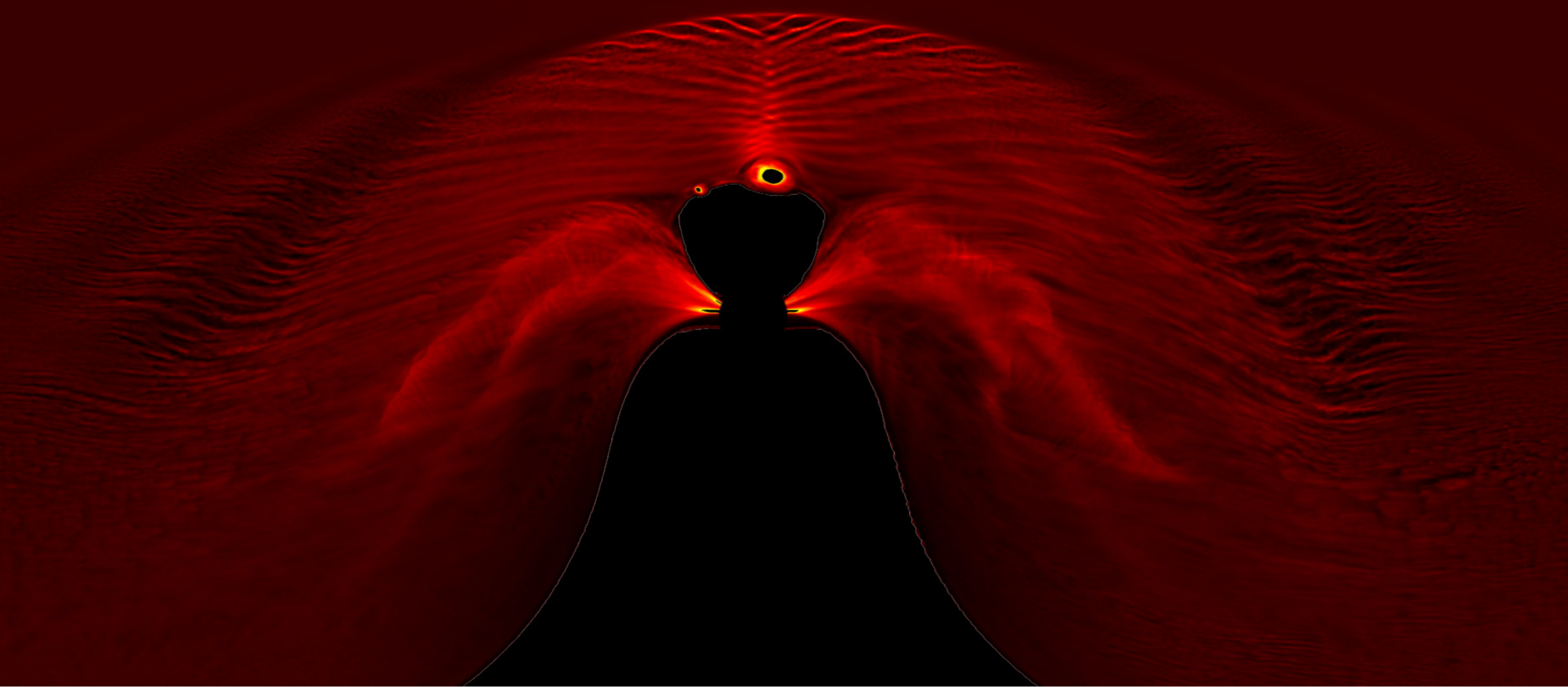

APPLAuSE Review Letters

~

As part of the intensive course on
SOFT SKILLS

Organized and Supervised by
Professor Marta Fajardo

Guest editor
Fábio Cruz

Cover figure

Plasma waves in magnetized bow shock, Fábio Cruz

When plasma flows (e.g. the solar wind) interact with dipolar magnetic obstacles (e.g. planetary magnetospheres), bow-shaped boundary layers can be generated. These layers, or shocks, separate the unperturbed flow (upstream) from turbulent plasma regions (downstream). This figure depicts the plasma density in a magnetized bow shock and was obtained in an *ab initio* simulation with parameters relevant for space scenarios (F. Cruz *et al.*, in preparation). The density modulations excited at the bow-shock correspond to lower-hybrid waves. A detailed characterisation of these waves is presented in **F. Cruz, APPLAuSE Review Letters pp: 22-29 (2016)**.

~

ARL 2016

Editor foreword

Welcome to the second issue of APPLAuSE Review Letters, our Doctoral Program's peer-reviewed academic journal. As in the previous years of the Softs Skills course, APPLAuSE students were able to practise the important job of article writing, refereeing, and editing of scientific works. The articles presented here are the culmination of this work. In contrast to the first edition, in which review articles were also submitted, this year's contents are more closely linked to the students individual thesis plan, and represent the advances made by this cohort during the first short-term trainings in their plasma physics topic of choice. In that respect, I would like to thank also the teams that hosted those short-term trainings and who authorised the publication of their work in the APPLAuSE Review Letters.

Finally, I would like to thank all the students for the work put into improving their communications skills, and in particular to this year's Guest editor, Fábio Cruz, for the additional effort of organising the magazine edition, and the selection procedure for two distinctions: The Best Figure Award, and the Cover Figure. Congratulations to those awarded.

We hope this edition will once again show the capabilities of our students, and inspire the next generation of APPLAuSE students.

Marta Fajardo
Instituto de Plasmas e Fusão Nuclear, Instituto Superior Técnico, Lisboa
E-mail address: marta.fajardo@tecnico.ulisboa.pt

Guest Editor foreword

It is our pleasure to present the second issue of APPLAuSE Review Letters. This edition gathers a collection of papers prepared by the students of the third cohort (C3) of the Advanced Program in Plasma Science and Engineering, or APPLAuSE. The diversity of subjects in this volume is representative of the wide range of interests of students in this cohort (from magnetically confined fusion plasmas to neutron physics, astrophysics and intense lasers).

On behalf of the students from APPLAuSE-C3, we would like to thank Professor Marta Fajardo for her dedicated work as Editor of this journal, and as mentor during the intensive module on Soft Skills during which the articles on this issue were peer-reviewed and significantly improved. As students, we believe that the work developed during this module was essential to our success as PhD candidates, as well as to our future career as scientists.

Fábio Cruz
Instituto de Plasmas e Fusão Nuclear, Instituto Superior Técnico, Lisboa
E-mail address: fabio.cruz@tecnico.ulisboa.pt

Best figure award

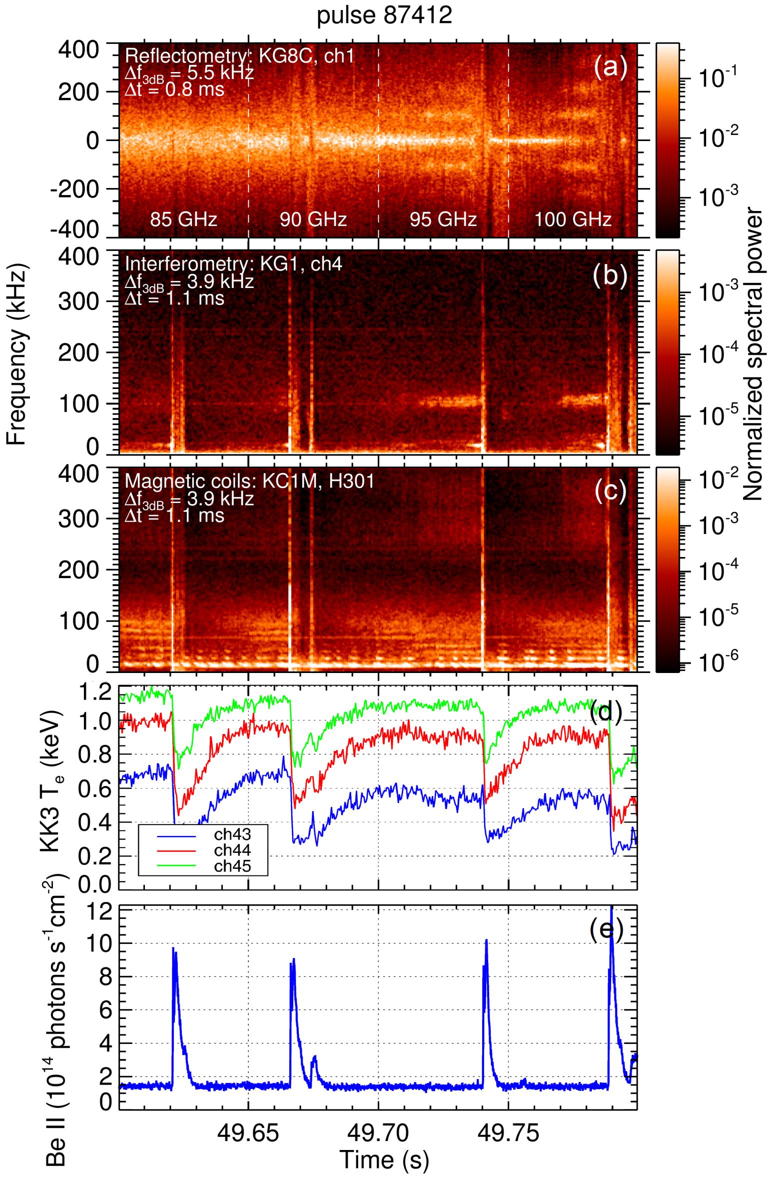

Inter-ELM quasi-coherent mode at JET, Luís Gil

Spectrograms of reflectometry (a), interferometry (b) and magnetic coils (c) and time traces of edge electron temperature (d) and Be II line radiation intensity (e), across three Edge Localized Mode (ELM) cycles of a JET discharge. The reflectometer and interferometer detect a quasi-coherent mode at 110 kHz before the last two ELMs which appears to be correlated with a decrease of temperature and is not observed in the magnetic signal. Read more about this figure in **L. Gil, APPLAuSE Review Letters pp: 43-50 (2016)**.

Table of Contents

Neutronics Simulations for new channel in DEMO's blanket

André Lopes

Instituto de Plasmas e Fusão Nuclear (IPFN), Instituto Superior Técnico, Avenida Rovisco Pais, 1049-001 Lisboa, Portugal

e-mail: andlop15@gmail.com

Abstract. This work is aimed to estimate the neutron flux which reaches the poloidal magnetic coils in DEMO realistic design, when a new cylindrical channel is added in order to allow the possibility of using a diagnostic. MCNP 6 has been used to run a simplistic scenario of a spherically symmetric system and tested several materials in order to benchmark the code. In the end, after incorporating the channel in the original DEMO's schemes provided by Eurofusion, simulations we ran for 10^9 particles from a 500 MW source leading to an expected neutron flux in the magnetic coils of 3×10^{11} neuttrons/m^2s.

Short bio. André is 24 years old and he has joined APPLAuSE this year after finishing his MSc in Engineering Physics at IST. He has been dedicated to Plasma Physics in the last couple of years, successfully concluding his MSc thesis on the topic of radiation tension in nonlinear plasma metamaterials at IPFNs Group for Lasers and Plasmas. During the last year he has been lecturing basic physics for IST undergraduates. This is something that he is passionate about and that he definitely wishes to pursue in his future career. André also tries to spend some time doing volunteering work.

1. Introduction

In the last decades, Plasma Physics and Nuclear Fusion have been highly developed in pursuit, among other things, of two of the biggest projects designed for sustainable production of energy: ITER (International Thermonuclear Experimental Reactor) and DEMO (DEMOnstration Power Station). With such an ambitious goal it is important to understand to what extent precautions, for instance radiological protection, have to be taken to ensure security in the experimental facilities. The study of neutron radiation in fusion devices becomes thus highly vital for the safe development of devices like ITER or DEMO.

It is known, that in most common nuclear fusion reactions that occur in world wide facilities neutrons with high energies are produced, with especial focus on the Deuterium-Tritium reaction

$$ {}^{2}_{1}D + {}^{3}_{1}T \rightarrow {}^{4}_{2}He + {}^{1}_{0}n \; (14 \; MeV) \tag{1.1}$$

where 14 MeV neutrons are released in the reactions. These are called fast neutrons, because they have energies above 100 keV. Since neutrons have no charge, they do not experience Coulomb collisions, but may instead be captured by the nuclei and thus interact with matter. In particular for the particular case of DEMO, neutrons fluxes are going to be determined using Monte Carlo simulations for 14 MeV neutrons.

For neutrons to interact and alter matter, that is to get absorbed, the energy of the neutrons has to be reduced in what it is called the thermalisation process. After the neutrons are considered thermal, they are in conditions of being absorbed (Krane 1988). When a neutron hits a nucleus ${}^{A}_{Z}X$, the nucleus will undergo the simple reaction

$$ {}^{1}_{0}n +^{A}_{Z} X \rightarrow^{A+1}_{Z} X^{*} \tag{1.2}$$

forming an new isotope in an excited state. The way the new nucleus evolves will determine the main reaction is actually taking place (Glasstone & Sesonske 1963): elastic scattering, inelastic scattering or radiative capture. The first two processes lead to the decrease of energy, acting as good moderating processes for neutron radiation. When the neutron is captured by a nucleus leading to the formation of an excited isotope, the deexcitation can be done by emitting a photon, which leads in most cases to the increase of the photon flux coming from the fusion device.

2. Methodology

The main objective of this work is to measure the impact of fast neutrons in the poloidal magnetic coils outside the main vessel, after a new channel has been built in DEMO's blanket. The existence of such channels is vital for the correct functioning of the reactor and most of its diagnostics which are usually inserted in the device using these channels. The nature of this work is purely computational and it will be performed in a realistic structure of DEMO. The study of the flux of neutrons and the amount of energy which gets deposited in the very surface of the channel are the quantities that were measured in this study. All the conducted simulations were made using the software MCNP 6 - Monte Carlo N-Particle transport code, version 6, (Pelowitz 2013).

The work was done through several stages, starting with an initial verification of the simple features of neutrons interacting with matter, for which a spherically symmetric system with dimensions of the order of a realistic fusion reactor has been used. Several materials have been used to test the dependence of the flux and the energy deposition quantities on the atomic number Z of the material in use. Finally, the design of the cylindrical channel was incorporated in DEMO's structured and the final simulations

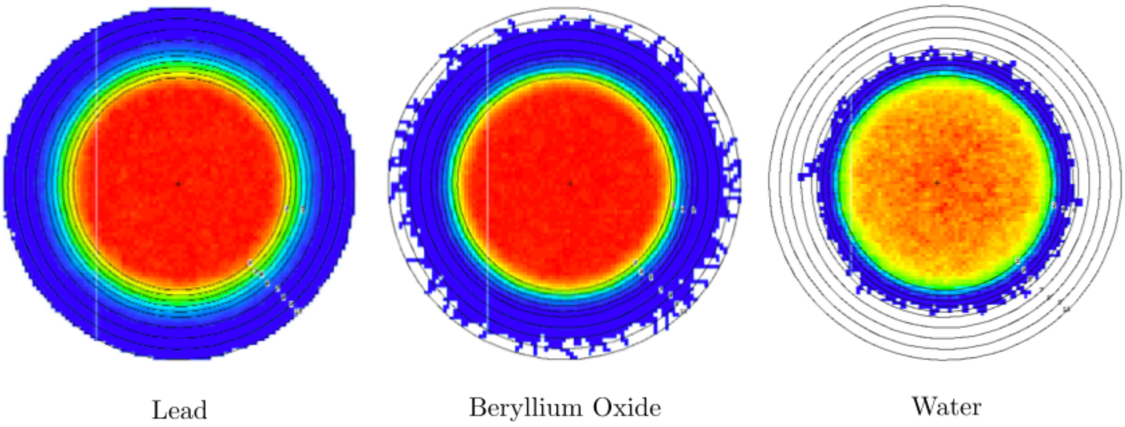

Figure 1: Simple illustration of the neutron fluxes obtained for different shielding materials: Lead (left), Beryllium Oxide (center) and Water (right).

were conducted in order to measure the amount of energy that gets deposited inside of the surface of a possible antenna inside the channel and of neutron flux that reaches the coils outside the channel. In all the simulations, 14 MeV neutron sources have been used in order to obtain quantities which match with values verified in different fusion devices.

3. Preliminary Studies

In order to simulate typical dimensions for a system representing a fusion reator, a spheric system was designed with concentric surfaces up to radii of 6-7m. The studied system was made of ten concentric surfaces, where the first four have a thickness of 20 cm and the last six a thickness of 40 cm. The simulations were conducted for three different shielding materials: Lead, Beryllium Oxide and Water, which are three of the most common neutron moderators, in order to study the known influence of the atomic number in the flux and energy deposition parameters.

An isotropic and spherically symmetric 14 MeV and 500 MW source with radius of 4 m was used to perform the simulations. Only 80% of the total power was consider do be due to neutrons from reaction in equation 1.1, being the remaining 20% responsible for accounting all the competing processes which originate other kind of particles. Additionally, because only a 40° portion of the entire torus is considered in the conducted simulations, only 1/9 of the total power of the source will be used. Considering the real dimensions of the torus, a flux of 1.98×10^{19} neutrons per unit area and per unit time, where real areas have been used.

3.1. *Neutron Flux and Energy Deposition*

Analyzing Figure 1, we can clearly state that light materials (made of light elements) are more suitable for neutron shielding than heavy materials. With Water layers, we see that the inner layers are enough to contain the emitted neutrons inside. On the other hand, Lead allows the neutrons to reach the outer layers, thus being a less effective moderator for 14 MeV neutrons when compared to water. The same can be seen when analysing concrete values in Figures 2 and 3.

When using Water as a shield, as the plot in Figure 2 clearly shows, at approximately 5 m from the center, or 1 m from the source (corresponding to surface number 5) the particle flux drops to zero, which is consistent with the results presented in Figure 1.

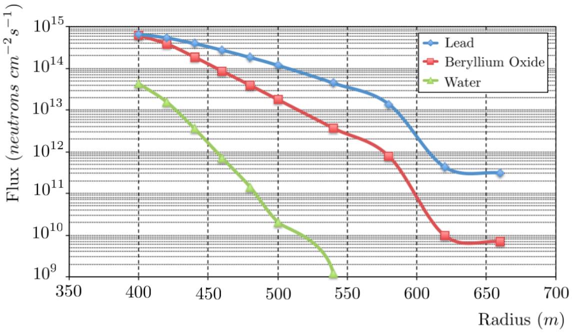

Figure 2: Neutron flux ($n^0/cm^2/s$) across the surfaces of the shielding layers.

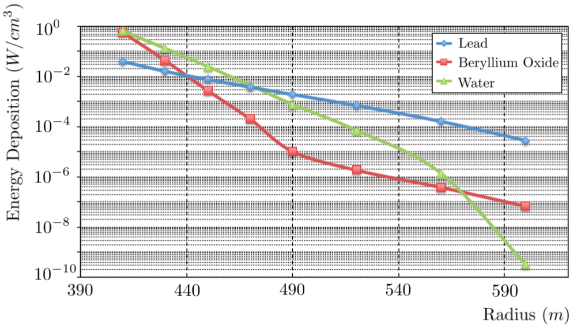

Figure 3: Energy deposition (W/cm^3) in the shielding cells.

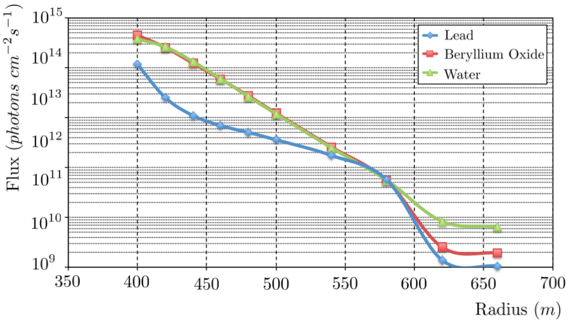

Figure 4: Photon flux ($\gamma/cm^2/s$) across the surfaces of the shielding layers.

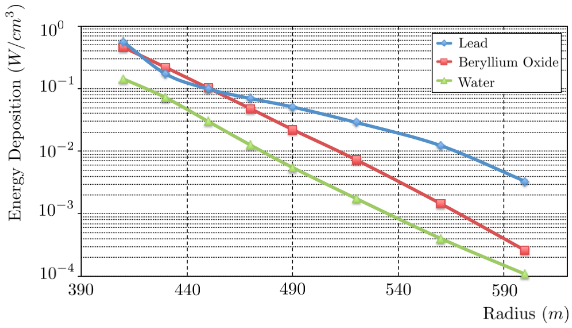

Figure 5: Energy deposition (W/cm^3) in the shielding cells due to photons.

Lead and Beryllium Oxide, on the other hand, are not able to prevent the neutrons from reaching the last surface and escaping the shielding, even though it appears from the simulation that the latter is more efficient in doing so. As predicted, heavier elements are not as efficient in stopping the neutron fluxes coming from the sources inside the shielding (Luis 2013). This can also be seen in the plot of the energy deposition, Figure 3, where we see that for the heavier materials there is more energy deposition in the outer layers, because neutrons can still pass through. As for Water, we see that the energy deposition decreases as we move away from the center because the neutron flux rapidly decreases with the distance from the center.

3.2. *Photon Flux and Energy Deposition*

Besides the neutrons, an additional simulation was performed considering the presence of photons and thus taking into account the radiative capture process mentioned in the Introduction.

As expected for all materials, Figure 4 shows that there is a large flux of photons in the first layers where the neutron flux is also higher, due to the close location to the source. As we move outwards the flux of photons we start to see the difference in the amount of photons which pass through the outer layers. Since the flux of neutrons starts to be neglectable in Water after the 4th/5th layer, then we expect a higher flux of photons instead, due to the fast absorption of neutrons and the deexcitation of the Water nuclei which will emit large amounts of photons. Also, contrary to what happens in the neutron case, the heavier elements will be more efficient in stopping the photons, as we can see when Lead is the shielding material.

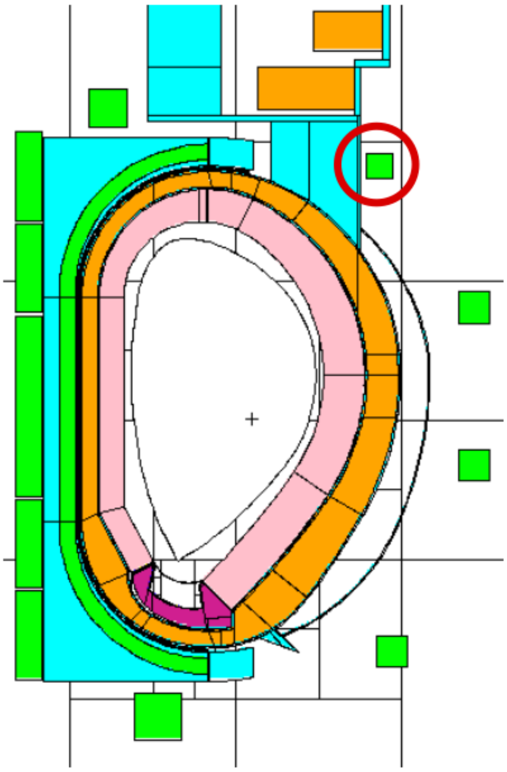

Figure 6: Complete section of the DEMO reactor. The red circle identifies the magnetic coil, where we want to measure the neutron flux and the energy deposition with the incorporation of the cylindrical channel.

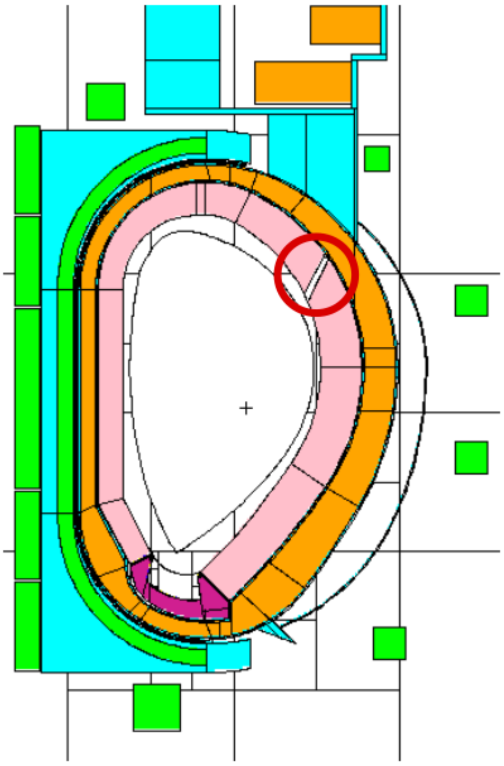

Figure 7: The same section but with an additional channel in the blankets. The red circle identifies the newly designed cylindrical channel.

4. Results in the real DEMO reactor

With some of the main features of neutron physics verified before, we proceeded to understand how neutrons play a role in a realistic design of the future DEMO reactor which will have about 6-7m of radius (Federici 2015). The schematics correspond to the ones used by the Eurofusion programme for the studies related to DEMO. The input files already incorporate a 500 MW source and an flux of 1.98×10^{19} neutrons per squared metre and per second. Figure 6 shows the original section of the torus, corresponding each of the colours to one different material, with a distinct atomic number Z and density ρ. It is also shown the poloidal magnetic coils where we want to estimate the incoming neutron flux, when in the presence of a new channel which is directed towards the coil. Figure 7 shows the built channel across the blanket of the reactor. The purpose of the channel is to account for the possibility of inserting diagnostics and antennas to measure plasma quantities. Moreover, in the design a thin cylindrical layer has been included. This layer has the typical thickness of an antenna (2 mm), and its purpose is to estimate the energy deposition in an antenna if it were inserted at that position.

4.1. *Results*

The simulations, ran during five full days, shown in Figure 8 were performed with 10^9 particles. Figure 8 shows that for the radius r = 10 cm, the flux reaching the coil appears to be bigger than in the other two cases, something that can be better seen in the plot in Figure 9, where we see an increase of the amount of neutrons per unit area and unit

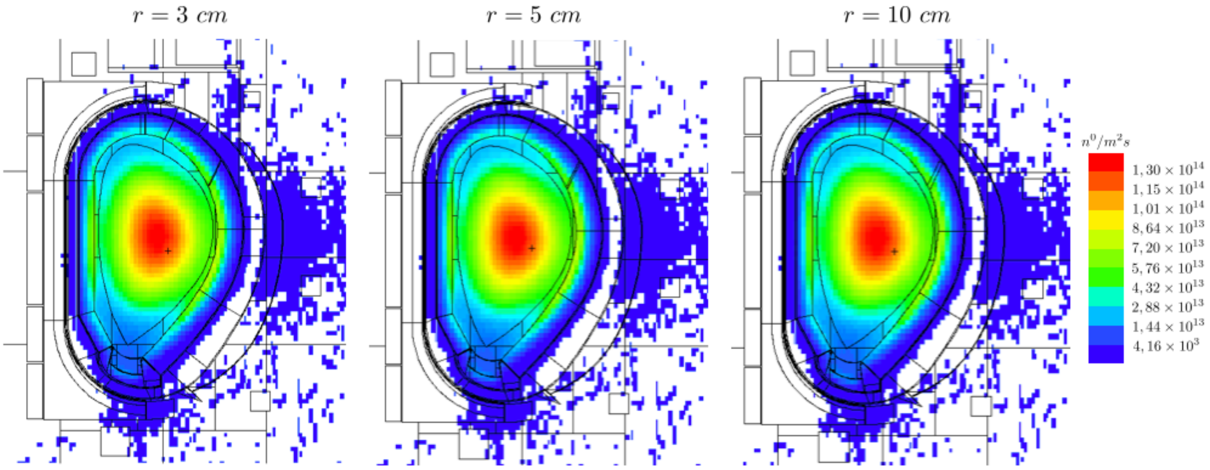

Figure 8: Simulation for the DEMO reactor for different radii of the cylindrical channel. From left to right: 3 cm, 5 cm and 10 cm.

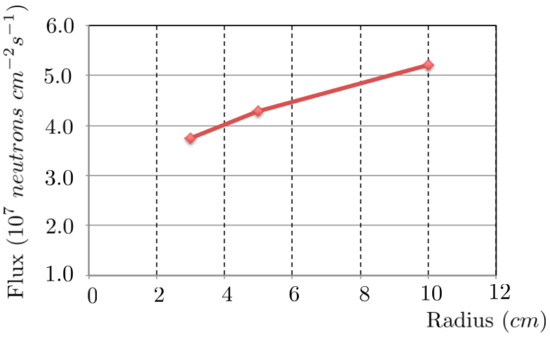

Figure 9: Neutron flux ($n^0/cm^2/s$) reaching the surface of the poloidal coil.

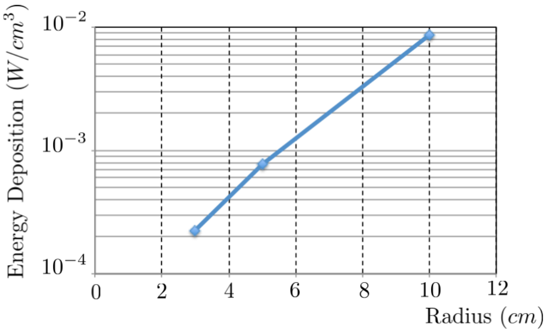

Figure 10: Energy deposition by the neutrons in the layer inside the channel.

time that reach the surface of the poloidal coil with the increasing of the radius of the channel. This plot also shows that we should expect a neutron flux bigger than at least 3×10^{11} neutrons/m^{2}s.

The energy deposition in the volume of the thin layer located on the top end of the channel has been estimated for all the three radii and the obtained results are shown in Figure 10. As expected, since the volume and area of contact both increase, the amount of energy deposited in the cell keeps increasing as the radius increases. This is due to the fact that higher radii leads to the increase of the neutron fluxes in the layer.

5. Conclusions

This work clearly shows an increasing of the amount of neutrons reaching the poloidal magnetic coil outside of the main chamber. For the simulations that were performed, fluxes of the order and bigger than 3×10^{11} neutrons per unit area and unit time can be expected, regardless of the radius of the cylindrical channel. Still, it is understandable that bigger radius will increase the neutron flux, as well as the energy deposited in any antenna that might be put inside the channel.

Even though the simulations took around five days and were performed with 10^9 particles, bigger simulations should be made for a better and deeper knowledge about the values we should expect for a realistic scenario. Also, the lack of an antenna in the simulation scheme may have enabled the possibility of greater neutron fluxes than the ones we might have in reality. Having in place an antenna, made of different materials might influence the obtained results for the better, leading to a slightly lower value of the expected neutron flux.

REFERENCES

Federici, G. 2015 Overview of the design approach and prioritization of R and D activities towards an EU DEMO. *Fusion Engineering and Design* **8367**.

Glasstone, S. & Sesonske, A. 1963 Nuclear reactor engineering. D. Van Nostrand Company.

Krane, K. S. 1988 Introductory nuclear physics. John Wiley and Sons.

Luis, R. 2013 Radiological protection and nuclear engineering studies in multi-mw target systems. PhD thesis, Universidade de Lisboa.

Pelowitz, D. B. 2013 Mcnp6 user's manual version 1.0. Los Alamos National Laboratory.

Magnetic Control for Tokamak Plasma Position: Modeling, Instrumentation and Control Techniques

Doménica Corona

Instituto de Plasmas e Fusão Nuclear (IPFN), Instituto Superior Técnico, Avenida Rovisco Pais, 1049-001 Lisboa, Portugal

e-mail: sacbecorona@hotmail.com

Abstract. Tokamak control engineering has an important goal for present and future devices which is to achieve increasingly better performance on the plasma stability. Control position in Tokamaks represents a challenge in terms of theory and instrumentation. First it will be explained the actual control system in IPFN tokamak "ISTTOK" and the future modifications on it. Afterwards the control results in new controller implementation in TCV will be showed, finally a review of models and control theories for JT-60SA.

Short bio. A Mexican national, Doménica received her diploma degree in Electric and Electronic Engineering at the Universidad Nacional Autónoma de México in 2014. She specialized in control engineering and robotics with a thesis work called Position control of the plasma column in a circular cross-section Tokamak. She started working while an undergraduate, having spent two years as a Field Services Engineer at the industrial sector in Siemens Mexico in the area of automation systems and SCADAs.

1. Basics Concepts

In a tokamak, the plasma is confined by the action of the electromagnetic forces which balance the internal kinetic pressure. The dynamics of the quantities of interest for position and shape control in a tokamak are governed by the ideal magnetohydrodynamics theory, related to the equilibrium described in Grad-Shafranov equation. See Miyamoto (2007).

In general, two different problems must be solved to achieve a toroidal equilibrium. The first involves radial pressure balance, because the hot core of the plasma tends to expand radially outward along the minor radius. In a tokamak configuration this pressure is balanced by the forces produced by an externally generated toroidal magnetic field, and by passing a toroidal current through the plasma itself. Indeed, by using the plasma as secondary winding of a transformer, the plasma current I_p and the related poloidal magnetic field are generated. The combined (toroidal and poloidal) magnetic fields results into an helical field.The second problem involves toroidal force balance, because the toroidicity generates a force that tends to expand the plasma outward along the major radius. In this case an externally applied vertical field is required to balance the forces. This vertical field is generated by the poloidal field (PF) coils, fig.1. This additional field is used both to achieve the desired plasma equilibrium and to control the plasma shape and position. See TOMMASI (2010).

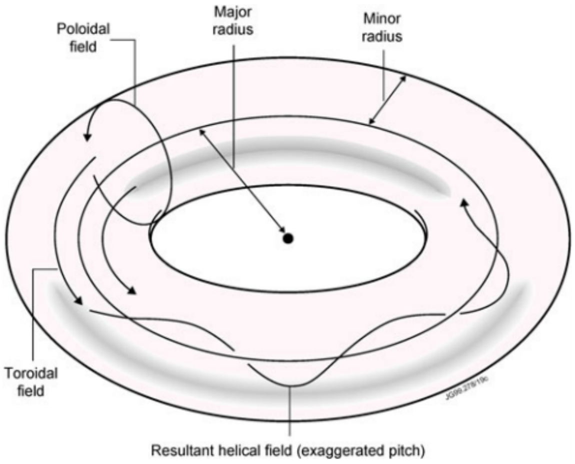

Figure 1: Description of toroidal and poloidal components of the magnetic field used in a tokamak to counteract the plasma pressure.A. Pironti (2008)

2. ISTTOK CODAC(Control, Data Access and Communication) and Real-Time Framework

ISTTOK has a set of 12 Mirnov coils for determine plasma centroid, which are then used in control. The magnetic probes are placed inside the graphite blocks of the limiter and they are oriented in order to measure the poloidal field created by the plasma current, so the coil winding is in the poloidal direction (each coil has 50 turns with an area of 25 [mm^2]). See fig.2.

From the position reconstruction made by the ISTTOK diagnostics control is applied

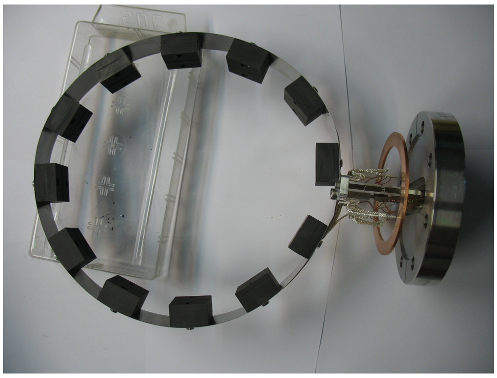

Figure 2: Mirnov coils and ISTTOK limiter for position reconstruction, acquisition port is located on the right side of the view, for the instrumentation of the 12 mirnov signals.

by the current set in the Poloidal Field Coils which are integrated by the Primary , Vertical and Horizontal coils as shown in fig.3. The plasma parameters are controlled using PID (proportionalintegralderivative controller) algorithms for feedback applied in the Poloidal Field Coils current set-point. The process variable is the plasma parameter to be controlled, the plasma parameter waveform is programmed in the main control system prior to the discharge and the result of this PID algorithm is the current reference that is sent to the respective actuator.

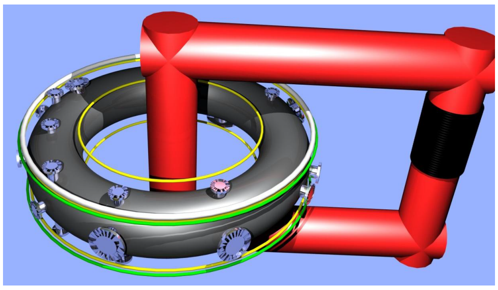

Figure 3: ISTTOK CAD Control Coils (Primary(black and white),Vertical (yellow) and Horizontal(green) Carvalho (2013)

The ISTTOK real-time control system was programmed in C++ on top of the Multi-threaded Application Real-Time executor (MARTe). MARTe is responsible for creating one or more real-time threads (according with the configuration database file provided by the user), each of these threads runs a sequence of code blocks named generic application module (GAM) each control cycle, one of these GAMs is the responsible to do the feedback PID control for the plasma position.

A PID controller is a control loop feedback mechanism, which continuously calculates an error value $e(t)$ as the difference between a desired setpoint and the measured process variable. The controller attempts to minimize the error over time by adjustment of a control variable $u(t)$, such as the position of the plasma column. In eq.2.1 is shown the equation describing this process with three constants to be defined in base of some criteria like the Ziegler-Nichols rules, which is a method for tuning a PID controller setting the I and D gains to zero. The P gain, is increased from zero until it reaches the ultimate gain, at which the output of the control loop has stable and consistent oscillations.

$$u(t) = K_p e(t) + K_i \int_0^t e(t)dt + K_d \frac{de(t)}{dt} \tag{2.1}$$

The usefulness of PID controls lies in their general applicability to most control systems. In particular, when the mathematical model of the plant is not known and therefore analytical design methods cannot be used, PID controls prove to be most useful. In the field of process control systems, it is well known that the basic and modified PID control schemes have proved their usefulness in providing satisfactory control, although in many given situations they may not provide optimal control.See Ogata (2002). In fig.4 is shown the MARTe HTML interface screen where the parameters of each coil PID are set(constants from eq.2.1).

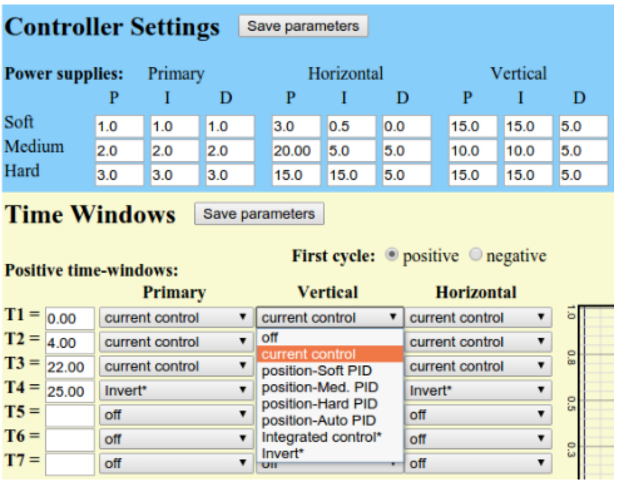

Controller Settings

Power supplies:	Primary P	Primary I	Primary D	Horizontal P	Horizontal I	Horizontal D	Vertical P	Vertical I	Vertical D
Soft	1.0	1.0	1.0	3.0	0.5	0.0	15.0	15.0	5.0
Medium	2.0	2.0	2.0	20.00	5.0	5.0	10.0	10.0	5.0
Hard	3.0	3.0	3.0	15.0	15.0	5.0	15.0	15.0	5.0

Time Windows

First cycle: ● positive ○ negative

Positive time-windows:

		Primary	**Vertical**	**Horizontal**
T1 =	0.00	current control	current control	current control
T2 =	4.00	current control		current control
T3 =	22.00	current control		current control
T4 =	25.00	Invert*		Invert*
T5 =		off		off
T6 =		off		off
T7 =		off		off

Figure 4: Selection of unable/enable PID control and constants setting

2.1. *Future work in ISTTOK*

A new GAM with an optimal Multiple input-Multiple output system (MIMO) control based on a state space model is programmed to be adapted in the MARTe framework in order to compare the results obtained for the control position with the PID controllers. Experimental results for Tokamak DIII-D via LQR optimal control are reported in Boyer (2013). New state-space controller to be adapted is a linear quadratic regulator (LQR) which is a well-known design technique that provides practical feedback gains.For controller design, it is necessary to propose two matrices both Q and R are positive definite, Q will be related with the penalties in time and transient response while R with the inputs. The values of these matrix should be substitute into the Riccati equation for LQR design (eq.2.2). See Chaooki (1995).Experimental results for Tokamak DIII-D via LQR optimal control are reported in Boyer (2013).

$$PA + A^T P + Q - PBR^{-1}B^T P = 0 \tag{2.2}$$

This equation is the matrix algebraic Riccati equation , whose solution P is required for computing the optimal feedback gain K. The Riccati equation is easily solved by standard numerical tools in linear algebra.

3. Model and Control Systems

The simpler models consider the plasma as a filament or non-deformable matrix of conducting filaments. The more complex models include nonlinear codes, which permit the simulation of nonlinear behaviors such as large vertical position displacements.

MHD theory provides a macroscopic dynamical description of an electrically conducting fluid in the presence of magnetic fields. Starting from MHD, the behavior of the system, consisting of the plasma, the surrounding passive structures, and the external PF coils, can be described by a set of nonlinear partial differential equations. Neglecting the plasma mass, the system dynamic can be regarded as a sequence of equilibria and the system may be model as a plasma linearized state space model. See A. Coutlis (1999).

State-space models are models that use state variables to describe a system by a set of first-order differential or difference equations, rather than by one or more nth-order differential or difference equations. They are described by the set of matrices equations 3.1 and 3.2.See Chen (1999).The meaning of each variable is written below.

$$\dot{x} = Ax + Bu \tag{3.1}$$

$$y = Cx + Du \tag{3.2}$$

►A state or system matrix
►B input matrix
►C output matrix
►D feedforward matrix
►x states vector
►y outputs vector
►u inputs vector

In terms of data acquisition, for the reconstruction of inputs and outputs from the system, several magnetic diagnostics must be integrated numerically through special boards and programming blocks including ADC(digital-analog converter) controllers and FPGA's, so the real time control can be implemented successfully, fig.5 shows more magnetic probes aside from the Mirnov coils.

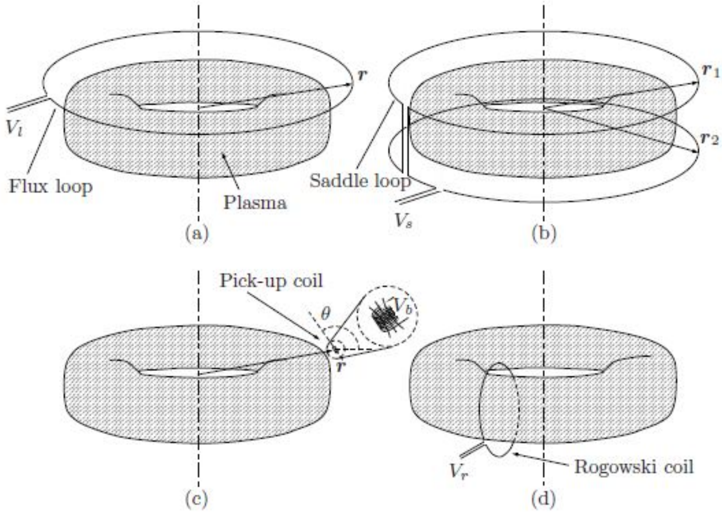

Figure 5: Typical magnetic sensors in a tokamak. All of these sensors operate on the principle that a flux change induces a voltage in a coil. This voltage is time integrated to determine the flux linked with the coil. A. Pironti (2008)

3.1. *TCV control*

TCV plasma experiments have used a PID algorithm based controller to correct the plasma vertical position. In 2013, TCV experiments employed a new optimal real-time controller, it was tested improving the stability of the plasma.A closed loop controller simulation tool was developed to test different possible algorithms and the results were used to improve the controller parameters. See Cruz (2015)

The controller was implemented based on the simulation results and tested during plasma discharges at TCV(discharge # 49567), with improvement in the overall stability of the plasma. The problem of finding the control law that drives the plasma position from an initial position X_0 to a final position X_1 in the minimum amount of time, is easier with the definition of a new system state X_N and the redefinition of the state system equations. Using Pontryagins Minimum Principle (used in optimal control theory to find the best possible control for taking a dynamical system from one state to another, especially in the presence of constraints for the state or input controls), the aim is to minimize the cost function given by the time to achieve the set point in order to complete the control for the state-space model shown in Cruz (2015) and A. Coutlis (1999). In fig.6 is shown the vertical position in a TCV discharge as predicted and measured for the new controller.

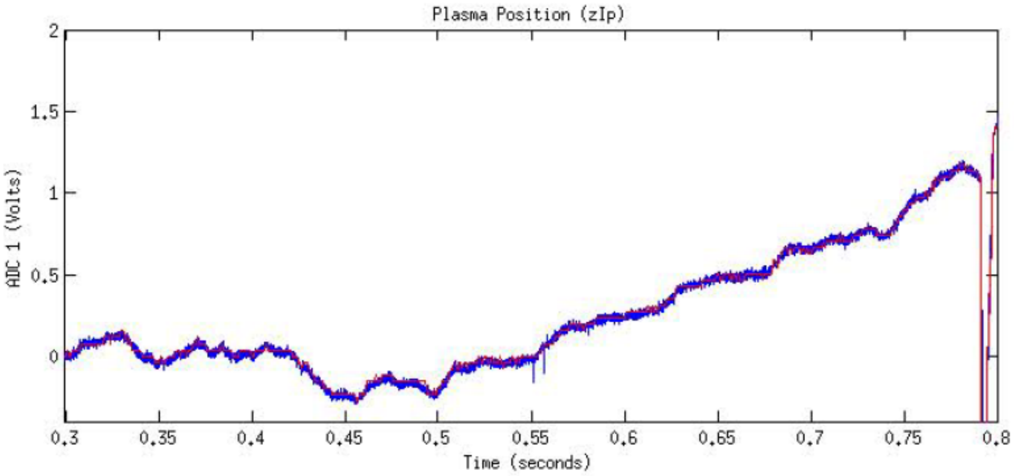

Figure 6: Plasma vertical position predicted (red) and measured(blue) using new optimal controller in TCV Cruz (2015)

3.2. *JT-60SA control*

JT-60SA is a fusion experiment designed to support the operation of ITER. Tokamak simulator has modules for simulated plasma, actuators and diagnostics. The simulator consist of an equilibrium solver and an "isoflux" controller that incorporates the effect of eddy currents induced on the vacuum vessel. Controlled parameters include the plasma current (I_P), the radial plasma position (R), the vertical plasma position (z), the height of the X-point from the divertor (X_P), and the triangularity (δ).See Miyata (2012).

A magnetohydrodynamic equilibrium control simulator (MECS) has been developed to study the techniques of plasma equilibrium control in JT-60SA, fig.7. The new modules of the plasma shape reconstruction, power supply,and simulated poloidal field coils are incorporated into MECS to simulate plasma equilibrium control. The equilibrium solver predicts plasma equilibrium and unknown eddy current under the given coil current by iteration. The simulator uses an isofluxcontroller for plasma equilibrium control, which modifies the coil currents to reduce the residual between the poloidal magnetic flux at the LCFS (Last Closed Flux Surface) and that at the control points which specify the plasma position and shape. The controller also changes the poloidal flux equally at all control points to reduce the difference between the actual and reference values of I_p.

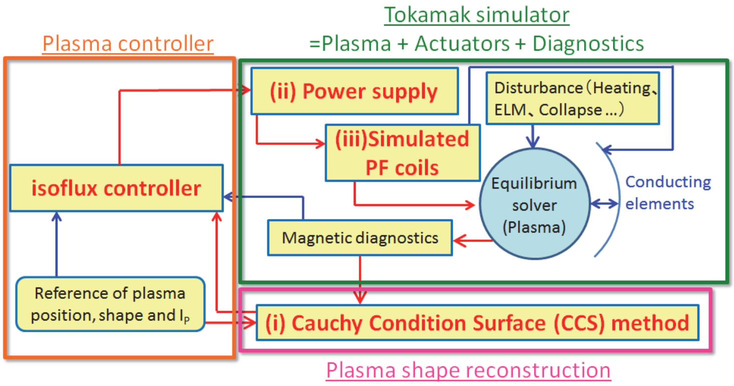

Figure 7: Diagram of Equilibrium reconstruction and control simulation for JT-60SA Miyata (2014)

4. Conclusions

Since the bigger devices have a large number of actuators and diagnostics for the control and reconstruction of the plasma position, MIMO controllers must be implemented on them. This means PID controllers used for almost all tokamaks in the past should be replaced for new control techniques including in a single algorithm all inputs and output,so better results for shape and position shall be achieved. Control based on State-space models is related with a plasma approximation including the MHD equilibrium description and an aproximation for Grad-Shafranov equation, which means also theoretical models should be improved.

REFERENCES

A. Coutlis, R. Albanese 1999 Measurement of the open loop plasma equilibrium response in TCV. *Nuclear Fusion* **39**.

A. Pironti, M. Ariola 2008 *Magnetic Control of Tokamak Plasmas*. Springer.

Boyer, D. 2013 First-principles-driven model-based current profile control for the DIII-D tokamak via LQI optimal control. *Plasma Physics and Control Fusion* **55**.

Carvalho, I. 2013 Real-time control for long ohmic alternate current discharges. PhD thesis, Universidade de Lisboa.

Chaooki, A. 1995 *Linear quadratic Control, An Introductions*. Prentice-Hall.

Chen, C. 1999 *Linear System Theory and Design*. Oxford University Press.

Cruz, N. 2015 An optimal real-time controller for vertical plasma stabilization. *IEEE Transactions on Nuclear Science* **62**.

Miyamoto, K. 2007 *Controlled fusion and plasma physics*. Taylor & Francis.

Miyata, Y. 2012 Development of a simulator for plasma position and shape control in JT-60SA. *Plasma and Fusion Research* **7**.

Miyata, Y. 2014 Study of plasma equilibrium control for JT-60SA using MECS. *Plasma and Fusion Research* **9**.

Ogata, K. 2002 *Modern Control Engineering*. Prentice Hall.

TOMMASI, G. DE 2010 Current, position, and shape controlin tokamaks. *FUSION SCIENCE AND TECHNOLOGY* **59**.

Investigation of fluctuations coupling during density ramp in AUG

Egor Seliunin

Instituto de Plasmas e Fusão Nuclear (IPFN), Instituto Superior Técnico, Avenida Rovisco Pais, 1049-001 Lisboa, Portugal

e-mail: eseliunin@ipfn.tecnico.ulisboa.pt

Abstract. In density ramp discharge, the SOL turbulence power spectrum shows time variation of power density in high and low-frequency ranges. These changes might be caused non-linear coupling between those frequency bands. The bicoherence analysis has revealed this interaction and has shown the dependence of the phenomenon on the diverter condition and on the radial position.

Short bio. Egor studied at St. Petersburgs State Polytechnical University, Russia, where he obtained his first MSc degree in Plasma Physics in 2013 while working with the reflectometry group at the FT-2 tokamak. The goal of his thesis was to investigate the interaction between microwave turbulence with GAM in plasmas by using bicoherence analysis. In order to broaden his knowledge he took part in the Erasmus Mundus Fusion EP programme from 2013 to 2015, where he obtained his second MSc degree in Engineering Physics and Nuclear Fusion, at Universitat Stuttgart and CIEMAT University (Madrid). His research was focused on studies of suprathermal ions in the TJ-II stellarator using spectroscopical methods. During this programme he also had a chance to work at IPP in Prague and CEA in Cadarache.

1. Introduction

The "anomalous" transport is an essential problem for the efficiency of fusion reactors (Wootton *et al.* 1990). Small-scale turbulence might cause this transport. The largest level of turbulence, observable in scrape-off layer (SOL), causes perpendicular transport of particles and energy on the walls. This level depends on different plasma parameters, such as a magnetic field configuration, gradients of density, pressure, and temperature. Here we considered discharge with density ramp performed on ASDEX-Upgrade (AUG) tokamak. The set-up with similar conditions is going to be used to perform the diverter detachment experiments in ITER. Power spectrum obtained from frequency modulated continuous wave (FMCW) reflectometry (Manso *et al.* 2001) at the low field side (LFS) in the SOL (see Fig. 1) has shown unusual behavior: the power of low-frequency range (up to 20 kHz) rose with time, in contrary to high-frequency range (20-330 kHz). This phenomenon has been previously observed in TEXTOR and DIII-D tokamaks (Budaev *et al.* 1993; Moyer *et al.* 1999). The effect might point on three-wave non-linear interaction. In order to investigate this phenomenon, we used bicoherence analysis (Kim & Powers 1979). The technique has been successfully used for clarifying the mechanism of turbulent transport inside the separatrix at the plasma edge, usually associated with the interaction between small-scale turbulence and zonal flows (see Tsui *et al.* 1993; Moyer *et al.* 2001; Nagashima *et al.* 2005; Gurchenko *et al.* 2013).

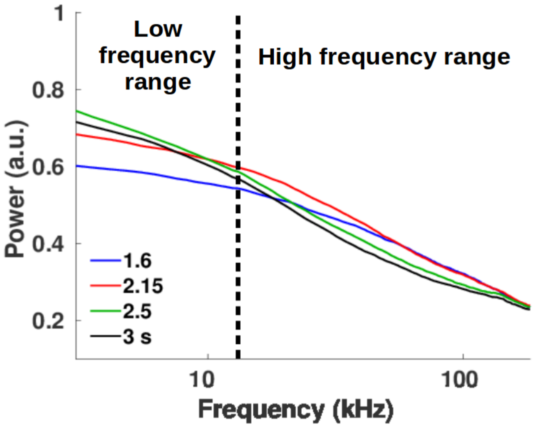

Figure 1: Power spectrum density at different times. The power density in low-frequency rises with time, while it decreases in the high-frequency range.

2. Experimental set-up and analysis method

Density ramp experiment (short #33484) was carried out in AUG (Fig. 2). The measurements of turbulence were performed by frequency modulated continuous wave (FWCW) reflectometry, operated in O-mode fixed frequency with the sampling rate of 2 MHz (Manso *et al.* 2001). The system has antennas at low and high field side (LFS and HFS), with four channels at each side. Those channels operate at following frequencies: 18 GHz (K channel), 26 GHz (Ka channel), 36 GHz (Q channel), and 52 GHz (V channel).

As we used fixed frequency for each channel, the cut-off position was pushed out towards the wall with density ramp. The evolution of cut-off position is shown in Fig. 2(e) in color code corresponding to different channels. The dashed line shows the position of separatrix. One can note that cut-off of K and Ka channels are always in the SOL, while Q channel cut-off at the beginning is inside the plasma and crosses the separatrix only at around 3.3 sec. Here we analysed by bicoherence technique only the data from K, Ka and

Q channels in LFS to investigate the non-linear interaction between frequency ranges in SOL.

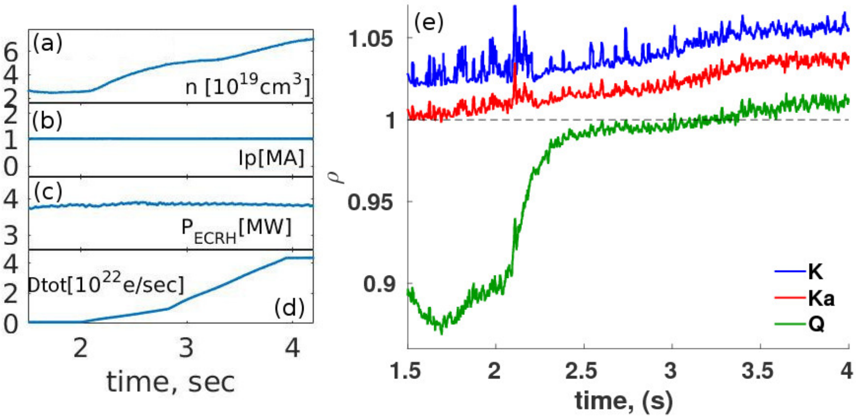

Figure 2: Plasma parameters of the density ramp experiment: (a) plasma density; (b) plasma current; (c) ECRH power; (d) gas puffing. (e) evolution of cut-off of different channels, operating at the fixed frequency, during the density ramp.

Bicoherence is a statistical measurement of the interaction rate between three spectral components by examining the phase coherence. The normalized bicoherence can be written as (see Kim & Powers 1979):

$$b^2(f_k, f_l) = \frac{|\langle X(f_k)Y(f_l)Z^*(f_k+f_l)\rangle|^2}{\langle |X(f_k)Y(f_l)|^2\rangle\langle |Z(f_k+f_l)|^2\rangle}, \tag{2.1}$$

where $X(f_k)$, $Y(f_l)$, $Z^*(f_k+f_l)$ are the Fourier harmonics of X, Y and Z. The bicoherence can vary from zero to one, where zero means three waves are completely independent and one means that Z is a product of the coupling between X and Y.

3. Experimental results

In order to investigate whether there is a non-linear coupling between the high and low-frequency ranges, we calculated the auto-bicoherence spectra. For that, as Fourier harmonics in (2.1) we used only the harmonics of the signal from one channel: K, Ka, or Q. We also applied the band-pass filter 2 - 330 kHz. Here the Nyquist frequency f_N is 1 MHz.

One can see the high level of bicoherence, corresponding for coupling high-frequency range (250 - 330 kHz) and low-frequency range (2 - 20 kHz)in channel Ka and K (Fig. 3(a-b)) and less pronounced in channel Q (Fig. 3(c)). The black line indicates the upper limit of the band-pass filter. Similar phenomena can be seen also in the signal from reciprocated probe, placed at LFS (Fig. 3(d)).

The bicoherence level also evolves in time, that might be caused by changes in the discharge conditions. In particular, the diverter state changes with density ramp to so-called diverter oscillations and then to complete detachment state (Potzel *et al.* 2013). A sign of this phenomenon could be seen in the spectrogram of a bolometer signal from a channel pointed at the X-point (Fig. 4). The power density increases in the time window from 2.4 sec to 3.0 sec, corresponding to diverter oscillations (the area within two red dashed lines). The complete detachment follows the diverter oscillation state.

In order to investigate an evolution of bicoherence between low-frequency range (2 - 20 kHz) and total density diapason, we calculated the bicoherence spectrogram for time

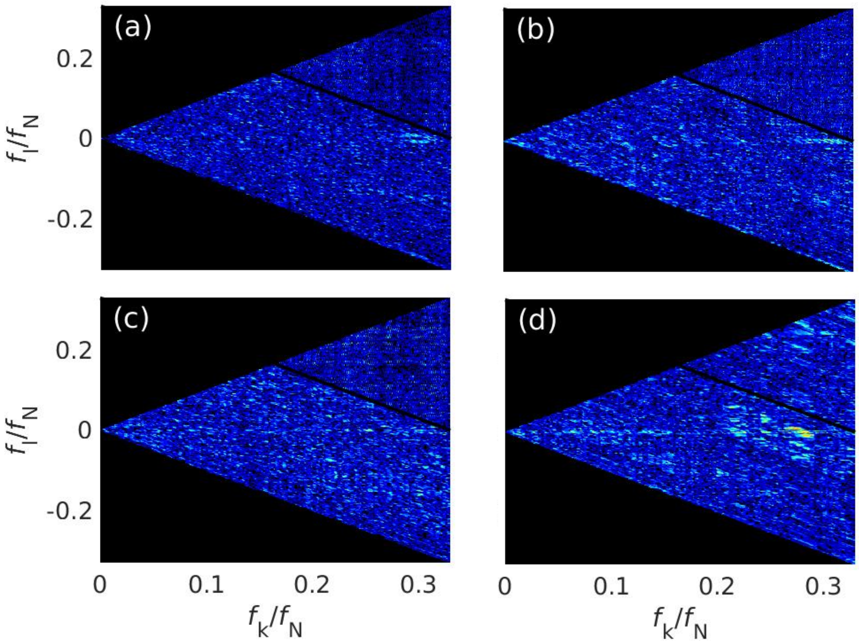

Figure 3: Bicoherence spectra, calculated for the channels: (a) Ka in time range 3.55 - 3.6 sec; (b) K in time range 3.45 - 3.5 sec; (c) Q in time range 3.4 - 3.45 sec. (d) Bicoherence spectra calculated for reciprocating probe at the LFS. The non-linear interaction is noticeable between low (2-20 kHz) and high (250-330 kHz) frequency ranges.

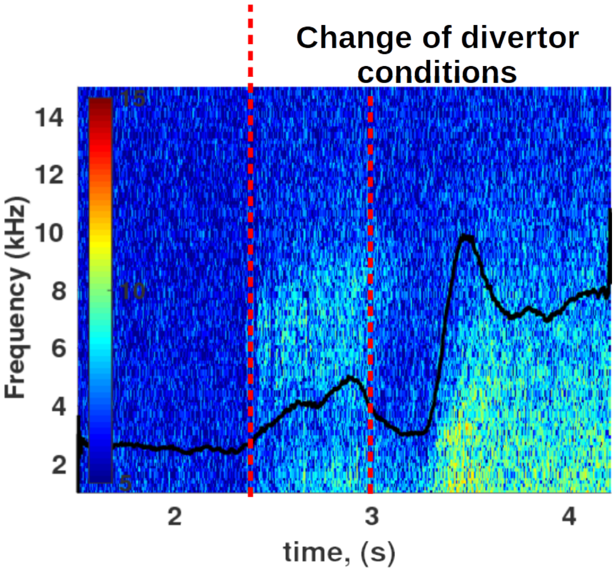

Figure 4: Spectrogram of a bolometer signal from a channel pointed at the X-point from the diverter side. The area within two red dashed lines corresponds to diverter oscillation state and complete detachment correspondingly. The complete detachment follows (3 - 4.3 sec). The black line indicates to total power spectra.

window 1.5 - 4.0 sec for each channel (see Fig. 5). The red dashed lines correspond to the different states of the diverter, as it is indicated in Fig. 4. The evolution of total bicoherence is also shown at the bottom of each figure. The black line corresponds to the average level of total bicoherence, calculated in time window 1.5 - 2.4 sec. The increase of nonlinear interaction is clearly seen throughout the diverter oscillations and complete detachment states (Fig 5(a)). Within the diverter oscillation state (2.4 - 3.0 sec), there is a peak of bicoherence. The non-linear coupling between low and high-frequency ranges is also visible in Fig 5(b). The total bicoherence for Q-channel exceeds the average level only after 3.3 sec (Fig 5(c)), corresponding to the time when cut-off of Q channel crosses the separatrix. Before 3.3 sec the total bicoherence is on the level of its average value calculated in time window 1.5 - 2.4 sec (dashed black line). It may point out on the fact that non-linear coupling of high and low-frequency range take place only in the SOL and disappears inside the separatrix. The peaks of bicoherence occurred before 3.3 sec might be caused by a spontaneous jump of Q channel in the SOL during the diverter oscillations.

4. Conclusion and discussion

In the discharge with density ramp, the variation in power spectrum in low and high frequencies in SOL might be caused (as authors suggest) with non-linear interaction between those diapasons. Bicoherence analysis has shown this coupling in reflectometry signal throughout of the discharge and partly in data, obtained from reciprocated probe. Moreover, the interaction may correlate with changes in diverter state. It is also most probable, that the non-linear coupling occurs only in SOL.

REFERENCES

Budaev, V, Fuchs, G, Ivanov, R & Samm, U 1993 Fractal dimensionality for different transport modes in the turbulent boundary plasma of textor. *Plasma physics and controlled fusion* **35** (3), 429.

Gurchenko, AD, Gusakov, EZ, Altukhov, AB, Selyunin, EP, Esipov, LA, Kantor, M Yu, Kouprienko, DV, Lashkul, SI, Stepanov, A Yu & Wagner, F 2013 Spatial structure of the geodesic acoustic mode in the ft-2 tokamak by upper hybrid resonance doppler backscattering. *Plasma Physics and Controlled Fusion* **55** (8), 085017.

Kim, Young C & Powers, Edward J 1979 Digital bispectral analysis and its applications to nonlinear wave interactions. *IEEE transactions on plasma science* **7** (2), 120–131.

Manso, ME, Varela, P, Nunes, I, Santos, J, Conway, GD, Hirsch, M, Klenge, S, Stober, J & others 2001 Reflectometry in conventional and advanced plasma scenarios on asdex upgrade and perspectives for iter. *Plasma physics and controlled fusion* **43** (12A), A73.

Moyer, RA, Lehmer, R, Boedo, JA, Watkins, JG, Xu, X, Myra, JR, Cohen, R, D'Ippolito, DA, Petrie, TW & Schaffer, MJ 1999 Potentials, e× b drifts, and fluctuations in the diii-d boundary. *Journal of nuclear materials* **266**, 1145–1150.

Moyer, RA, Tynan, GR, Holland, C & Burin, MJ 2001 Increased nonlinear coupling between turbulence and low-frequency fluctuations at the l- h transition. *Physical review letters* **87** (13), 135001.

Nagashima, Y, Hoshino, K, Ejiri, A, Shinohara, K, Takase, Y, Tsuzuki, K, Uehara, K, Kawashima, H, Ogawa, H, Ido, T & others 2005 Observation of nonlinear coupling between small-poloidal wave-number potential fluctuations and turbulent potential fluctuations in ohmically heated plasmas in the jft-2m tokamak. *Physical review letters* **95** (9), 095002.

Potzel, S, Wischmeier, M, Bernert, M, Dux, R, Müller, HW, Scarabosio, A & others 2013 A new experimental classification of divertor detachment in asdex upgrade. *Nuclear Fusion* **54** (1), 013001.

Tsui, HYW, Rypdal, K, Ritz, Ch P & Wootton, AJ 1993 Coherent nonlinear coupling between a long-wavelength mode and small-scale turbulence in the text tokamak. *Physical review letters* **70** (17), 2565.

Wootton, AJ, Carreras, BA, Matsumoto, H, McGuire, K, Peebles, WA, Ritz, Ch P, Terry, PW & Zweben, SJ 1990 Fluctuations and anomalous transport in tokamaks. *Physics of Fluids B: Plasma Physics (1989-1993)* **2** (12), 2879–2903.

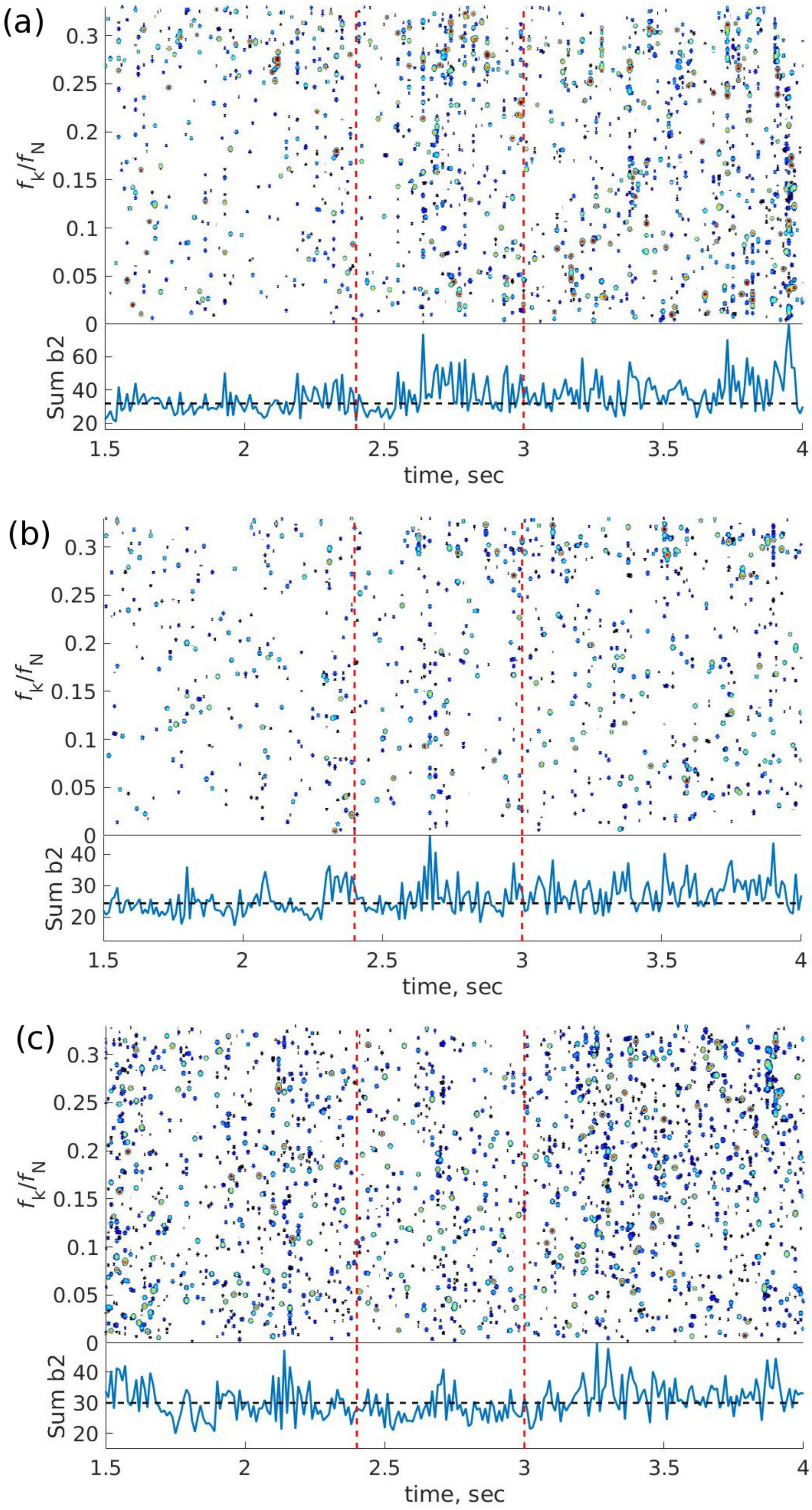

Figure 5: Bicoherence spectrogram and total bicoherence between the low-frequency range of 2 - 20 kHz and entire frequency diapason for channels: (a) K, (b) Ka, (c) Q. Dashed red lines show different diverter states: on-set state, oscillation state, complete detachment correspondingly. Dashed black line shows the average level of bicoherence, calculated in time window 1.5 - 2.4 sec.

Wave and particle spectra of subrelativistic magnetized collisionless shocks

Fábio Cruz

Instituto de Plasmas e Fusão Nuclear (IPFN), Instituto Superior Técnico, Avenida Rovisco Pais, 1049-001 Lisboa, Portugal

e-mail: fabio.cruz@tecnico.ulisboa.pt

Abstract. Efficient particle acceleration in relativistic collisionless shocks is only possible in the presence of an initial seed of energetic particles. Resorting to Particle-in-Cell (PIC) simulations, we identify the nature of the waves excited in sub-relativistic collisionless shocks and discuss their capability of producing high energy populations. We present a systematic method to characterize the wave spectrum of these shocks and show that waves close to the lower-hybrid wave frequency are excited and able to produce highly anisotropic particle distributions for both ions and electrons. A single particle approach is used to study the kinematics of charged particles in these waves from a fundamental perspective. The results show that ions can be stochastically accelerated in the perpendicular direction to the background field, in agreement with the results obtained from PIC simulations.

Short bio. Fábio was born in 1992 in Lisbon, Portugal. He obtained his MSc degree in Engineering Physics in 2015 from IST, under the supervision of Dr. Paulo Alves and Prof. Luís O. Silva. In his thesis project, developed at IPFNs Group for Lasers and Plasmas, he performed large-scale particle-in-cell simulations of magnetized plasma flows interacting with small-scale, magnetic obstacles under astrophysical and laboratory conditions. Understanding the role of the kinetic-scale physics investigated in his work was important, for instance, in the design of laboratory astrophysics experiments to study particle acceleration due to lower-hybrid turbulence developed at planetary/cometary bow shocks. As an undergraduate student, he was a member of Pulsar, a Portuguese science communication magazine nationally distributed. He has also organized several science/physics fairs at IST, visited annually by more than a thousand high school students. During his graduation years he also worked as an assistant lecturer at IST, where he taught problem solving classes and laboratory classes on Classical Mechanics. In his free time, Fábio enjoys playing sports and exploring his creativity in graphic and web design.

1. Introduction

One of the key questions that remain to be answered in astrophysics concerns the acceleration of particles to extremely high energies (up to 10^{20} eV). In the past decade, several works have shown that relativistic shocks created in supernova explosions, gamma-ray bursts and other extreme astrophysical scenarios are able to accelerate particle to such energies (Spitkovsky 2008*a*,*b*; Martins *et al.* 2009). In these shocks, particles are scattered in turbulent electromagnetic structures and are accelerated via multiple order Fermi processes (Blandford & Eichler 1987). However, an effective acceleration can only be attained in these shocks in the presence of an initial population of relativistic particles (Protheroe & Clay 2004). In this work, we discuss the role of sub-relativistic shocks as a candidate mechanism to provide this seed of energetic particles. In particular, we use computer simulations to study sub-relativistic magnetized collisionless shocks, due to their ubiquity in space environments, namely in the interaction between plasma flows (e.g. the solar wind) and large obstacles (e.g. planets, comets). Due to the small-scale character of the processes in study, we use Particle-in-Cell (PIC) simulations, which are capable of accurately resolving the kinetic plasma scales. These simulations are described in detail in section 2. The wave and particle spectra generated in these shocks are then studied using these simulations (section 3). The nature of the waves excited in these shocks is identified and the kinematics of individual charged particles in these waves is solved using a single particle approach (section 4), with the aim of describing the mechanism responsible for the particle acceleration in these shocks.

2. Methods

The PIC simulations shown here were performed with the code OSIRIS (Fonseca *et al.* 2002), a massively parallel, fully relativistic, electromagnetic PIC code. OSIRIS solves the detailed trajectories of the individual charged plasma particles, which interact with each other by their self-generated fields. It operates in normalized units, the independent parameter being the plasma density n_0. Times and lengths are normalized to $1/\omega_{pe} = \sqrt{\varepsilon_0 m_e/e^2 n_0}$ and c/ω_{pe}, respectively, where ε_0 is the vacuum permittivity, e and m_e are electron's charge and mass and c is the speed of light in vacuum. The simulations presented in this work are two-dimensional. In these simulations, a plasma initially filling the full simulation domain is continuously injected from the left boundary of the 2D simulation box. Its profile is constant (a step-like function) in the transverse (longitudinal) direction. This plasma stream is reflected close to the right boundary of the simulation box due to the presence of a second (extremely dense) plasma slab. Periodic boundary conditions are used in the transverse direction. The ion-to-electron mass ratio of the plasma stream is $m_i/m_e = 400$. This stream is injected with a bulk velocity $v_0/c = 0.02$ and a temperature $T_e = T_i = 1$ eV. A magnetic magnetic field, aligned in the simulation plane but perpendicular to the plasma flow, is externally applied in the full simulation domain. Its magnitude B_0 is chosen such that the ion Larmor radius is $\rho_i = v_0 m_i/B_0 e = c/\omega_{pi} = \sqrt{m_i/m_e}\ c/\omega_{pe} \gg c/\omega_{pe}$, i.e. such that the ions are unmagnetized. In these conditions, the electron Larmor radius is $\rho_e = \sqrt{m_e/m_i}\ c/\omega_{pe} \ll c/\omega_{pe}$. The simulation box length is 10 (15) c/ω_{pi} in the transverse (longitudinal) direction, whereas the spatial grid separation is 0.1 (0.05) c/ω_{pe}, with 25 particles per cell.

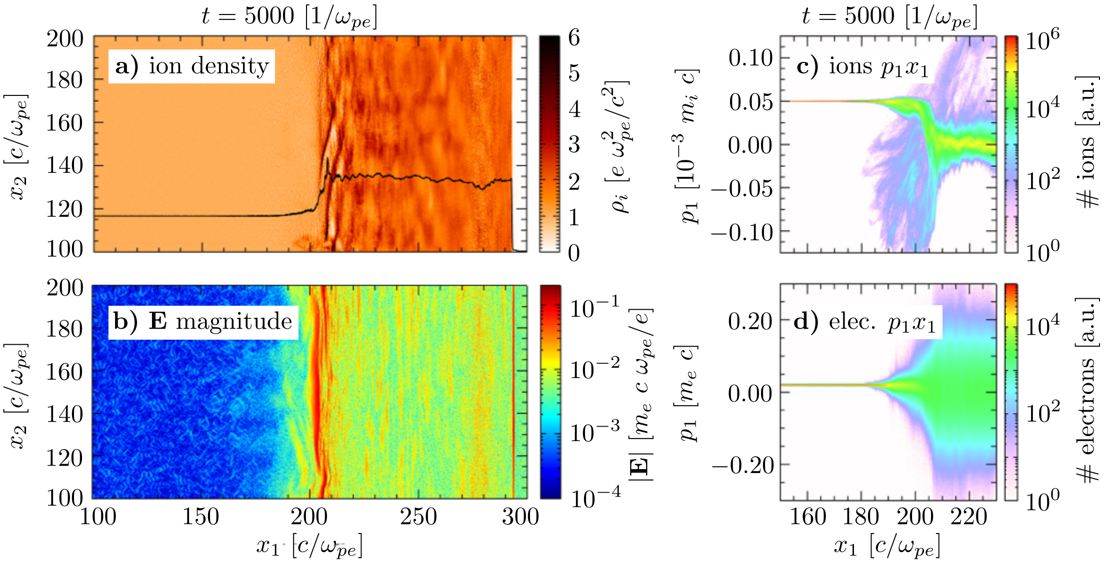

Figure 1: Plasma a) ion density, b) electric field magnitude and c) ion and d) electron phase spaces obtained in the PIC simulation described in the text.

3. Wave and particle spectra

As the plasma stream is reflected, a shock is formed, dividing the plasma in an unperturbed and a turbulent region, corresponding to the upstream and downstream, respectively. Several plasma quantities are represented in figure 1, at a time where the shock is already fully developed. The plasma compression is clear in the ion density and electric field magnitude plots (panels a) and b), respectively). In the phase spaces shown in panels c) and d), one can observe the distinct ion and electron dynamics in these shocks. While ions are reflected off the shock front, travelling in the upstream up to a distance comparable to ρ_i, electrons are magnetized upstream, across the shock front and downstream. In the ion density and electric field magnitude plots, we can also observe modulations at different scales, corresponding to different plasma waves. In the upstream, short modulations are excited in the region where the ions reflected in the shock front counter stream with the unperturbed plasma ions. These waves grow in amplitude close to the shock front, eventually to a nonlinear or even turbulent stage. In this process, they colapse into higher wave lengths (lower wave numbers), forming the large-scale structures observed in the downstream.

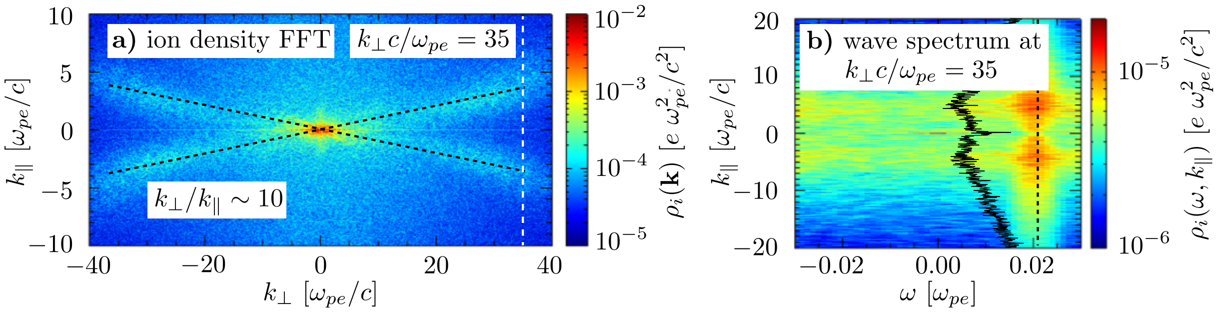

Figure 2: Wave spectrum generated in the collisionless shock studied in this work: a) FFT of the ion density for a fixed time (that shown in figure 1); b) slice of the FFT of the 2D ion density time evolution at $k_\perp c/\omega_{pe} = 35$ (identified with a white dashed line in panel a)).

The spectrum of the waves generated in both the upstream and downstream of the shock described above is shown in figure 2. In panel a), we can observe the Fast Fourier Transform (FFT) of the ion density plot shown in panel a) of figure 1. In this figure we can see that the higher amplitude modes are those with small $\mathbf{k}$ (both in parallel and perpendicular directions), corresponding to the large-scale modulations discussed above. Additionally, it is also clear that high $k_\perp$ modes also exist, corresponding to the small amplitude upstream oscillations. These modes have $k_\perp/k_\parallel \sim 10$ and are identified with a black dashed line in panel a) of figure 2. In order to obtain the frequency of these waves, we proceeded as follows. After performing a three dimensional FFT over a dataset containing the time evolution of the 2D ion density maps, we have taken a slice at $k_\perp c/\omega_{pe} = 35$, corresponding to the white dashed line identified in panel a) of figure 3. This slice is shown in panel b), where clear peaked regions are observed at $\omega/\omega_{pe} \simeq 0.02$ for $k_\parallel c/\omega_{pe} \simeq 5$. This frequency is comparable to that of lower-hybrid (LH) waves, which is $\omega_{\text{th}}/\omega_{pe} \simeq 0.024$ for the parameters used in this simulation. This value can be obtained by the LH waves dispersion relation (Bonoli 1984), given by

$$\omega^2 \simeq \omega_{\text{LH}}^2 \left(1 + \frac{m_i}{m_e}\frac{k_\parallel^2}{k_\perp^2})\right) \quad , \text{with } \ \omega_{\text{LH}}^2 = \frac{\omega_{pi}^2}{1+\omega_{pe}^2/\omega_{ce}^2} \ . \tag{3.1}$$

Since LH waves have a typical frequency $\omega \sim \omega_{\text{LH}}$, it follows that $k_\perp/k_\parallel \sim \sqrt{m_i/m_e}$, which is also consistent with the wave number analysis presented in panel a) of figure 2. An interesting consequence of this ordering is that possible resonant interactions between particles and the electric field of LH waves is highly anisotropic. In particular, and noting that in these waves $\omega_{ci} \ll \omega \ll \omega_{ce}$, ions interact with the perpendicular component of the wave such that $\omega \simeq k_\perp v_{i\perp}$, whereas electrons interact with the parallel component of the wave according to $\omega \simeq k_\parallel v_{e\parallel}$. This means that energy within the ion waves can be transferred to accelerate the electrons parallel to the magnetic field.

Despite the limitations of the method used to characterize the wave spectrum presented here (e.g. assumes periodic datasets), it clearly suggests that waves close to the lower-hybrid frequency are excited in these shocks. Hence, the resonant behaviour between particles and the waves discussed above might be relevant. In particular, and according to results first obtained by Karney (1978) in the context of Magnetic Confinement Fusion (MCF), ions are expected to be stochastically accelerated in the perpendicular direction to the background magnetic field. Such feature can be probed by calculating the temperature anisotropy $T_\perp - T_\parallel$ of the ion species in the simulation. This was done by computing the second moment of the distributions obtained in the respective phase spaces along the longitudinal direction. Since the geometry used in this simulation (slab) does not allow for a stationary shock (it propagates indefinitely to the left), we chose to represent the temperature anisotropy in the shock reference frame, in which the longitudinal coordinate is written as $\xi_1 = x_1 - v_s t$, where v_s is the shock velocity.

The time evolution of the ion temperature anisotropy is represented in panel a) of figure 3. The results show that $T_\perp \gtrsim T_\parallel$ for ions everywhere (i.e. both in the upstream and downstream), which is consistent with the perpendicular stochastic acceleration hypothesis. However, one should note that the ion distribution function cannot be approximated by a single Maxwellian in the close upstream (as shown in panel c) of figure 1) and thus its second moment is not an accurate measurement of the ion temperature in this region. The same method was applied for the electron distribution and the corresponding temperature anisotropy map is represented in panel b) of figure 3. Interestingly, we can observe that $T_\parallel \gtrsim T_\perp$ everywhere for electrons. Note that this is an expected result, as, due to the nature of the LH waves, it is possible that ions and

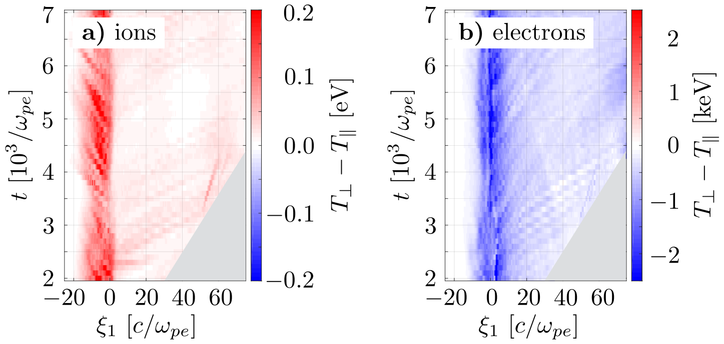

Figure 3: Average temperature anisotropy spatial dependance as a function of time measured in the shock reference frame $\xi_1 = x_1 - v_s t$ for a) ions and b) electrons.

electrons interact resonantly with the waves at the same time when $\omega \sim k_\perp v_{i\perp} \sim k_\parallel v_{e\parallel}$. Together with the wave spectrum analysis presented above, this result suggests that particles can be resonantly accelerated in the waves excited in astrophysical collisionless magnetized shocks in the conditions described in this work. In the next section, we use a single particle approach to study in more detail the mechanisms responsible for the particle acceleration in these scenarios.

4. Acceleration mechanism

In the PIC simulations presented in this work, any wave field is self-consistently evolved in time with the particle distributions. Hence, it is impossible to isolate the particle acceleration process from the wave temporal evolution. In order to perform a more fundamental study of this acceleration process, we solve the kinematics of single charged particles in the fields of a LH wave, namely $\mathbf{B_0} = B_0\mathbf{e_z}$ and $\mathbf{E} = E\cos(k_\perp y - \omega t)\mathbf{e_y}$. We follow the approach introduced by Karney (1978) and consider that the particles do not interact with each other and do not modify significantly the wave field. Intuitively, we can describe the ion trajectory as a combination of the Larmor rotation about the magnetic field direction and the resonant interaction with the electric field. Furthermore, since $\omega \gg \omega_{ci}$ for LH waves, the resonant interaction occurs in a very fast time scale compared to the Larmor rotation period. This means that, while performing the usual gyromotion, an ion initially with $v_\perp > \omega/k_\perp$ can interact resonantly with the wave field multiple times and receives an energy boost, being effectively accelerated.

A quantitative study of the particle trajectory in these fields can be done using an Hamiltonian formalism. In particular, the particle equations of motion can be written using this formalism as

$$\ddot{y} + y = \alpha\cos(y - \nu t) \quad , \quad \dot{x} = y \quad , \tag{4.1}$$

where distances are normalized to $1/k_\perp$ and times to $1/\varOmega$, with $\varOmega = qB_0/m$ for a particle with charge q and mass m. The constants introduced in the equations above are $\alpha = Ek_\perp/B_0\varOmega$, the amplitude of the electric field in normalized units, and $\nu = \omega/\varOmega \gg 1$. Note that equations 4.1 is equivalent to that of a driven harmonic oscillator and a resonant interaction, characteristic of such system, is expected.

A numerical solution of equations 4.1 could be used to determine the particle trajectory for any set of parameters α and ν with given initial conditions. In this work, however, we numerically integrate Newton's second law $m\dot{\mathbf{v}} = \mathbf{F}$, with a total force given by Lorentz Force, $\mathbf{F} = q(\mathbf{E} + \mathbf{v}\times\mathbf{B})$. Naturally, the two systems of equations are equivalent, and the presented choice is only motivated by the fact that the latter is more general and could, thus, be used in future works.

The numerical integration is done in two steps: the Boris method (Boris 1970) is used to advance the particle velocity, i.e. to solve $d\mathbf{v}/dt = \mathbf{F}/m$, and a leapfrog method is used to advance the particle positions according to their definition, $d\mathbf{x}/dt = \mathbf{v}$.

Due to the complexity of the particle trajectories for nonzero amplitudes of the electric field, it is impractical to represent their motion for long periods using phase spaces. Instead, we represent the particle trajectory in a Poincare map. This technique consists, in this particular case, of registering the wave phase seen by the particle (ωt) whenever it completes a cyclotronic period, e.g. when it crosses $y = 0$ when travelling in the negative y direction. The trajectories of 50 particles with different, equally spaced initial velocities were computed for $\alpha = 2$, 3 and 10 and the respective Poincare maps are shown in figure 4. For a small amplitude of the electric field, $\alpha = 2$ (panel a)), we see small perturbations to the particle trajectories, in particular those with initial $v_\perp > \nu$, identified with a dashed line. In this case, it is also possible to observe the initial formation of islands in the Poincare maps. In fact, the formation and overlap of these islands is a critical precursor for the stochastic motion of particles. In his original work, Karney (1978) derived that the critical electric field amplitude for the appearence of such stochasticity is $\alpha_{\text{crit}} = (1/4)\nu^{2/3}$ in normalized units. For the considered ν, $\alpha_{\text{crit}} \simeq 3.061$. Panel b) shows a Poincare map for an electric field amplitude very close to this value, where it is possible to observe larger islands than before. For higher electric field amplitudes, the islands become closer and closer and particles can eventually jump from one to another, acquiring a stochastic behaviour (see panel c) for an amplitude $\alpha = 10$).

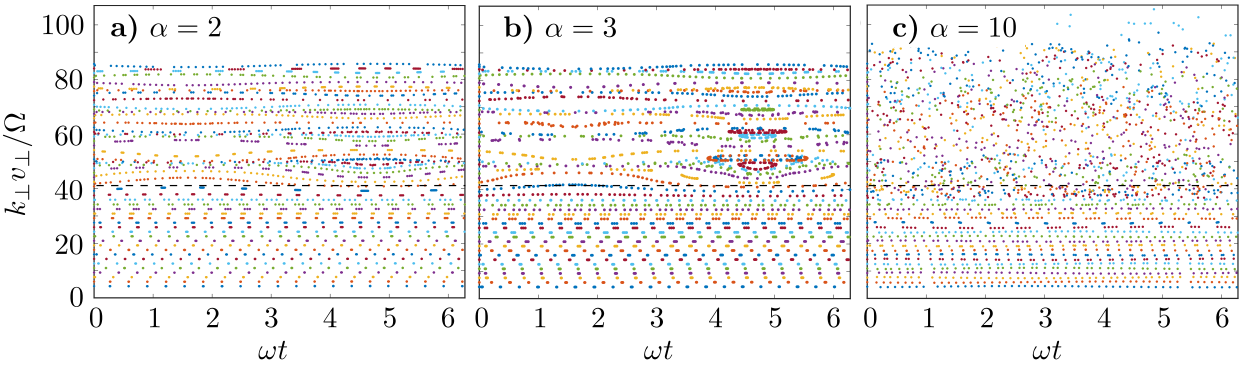

Figure 4: Poincare maps for 50 particles moving in an electric field of ampliude $\alpha = 2$, 3 and 10 (panels a), b) and c), respectively).

In the stochastic trajectories studied with the examples above, particles have access to much broader regions of their phase space. In other words, particles can be effectively accelerated in their stochastic motion. In order to illustrate this acceleration, we followed the time evolution of a collection of 2000 particles over 100 gyroperiods (see figure 5). The initial particle velocities were chosen such that their distribution was a Maxwellian. At the end of the 100 gyroperiods, clear changes are observable for particles with velocities larger than the resonant velocity $v_\perp > \nu$, again shown in a dashed line. In fact, most of the particles with velocities above the wave phase velocity were accelerated, creating a bump in the distribution centered at $v_\perp \simeq 2\nu$. In this case, the considered electric field amplitude was $\alpha = 30$.

The ion acceleration observed here is qualitatively consistent with the results presented in the previous section obtained using PIC simulations. However, it is clear that we are

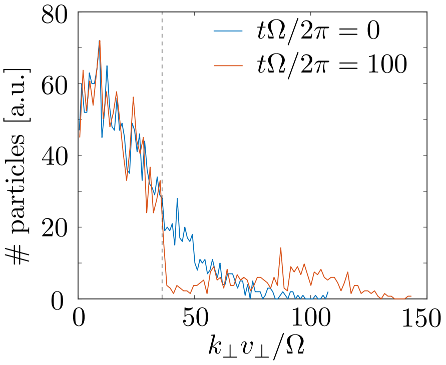

Figure 5: Perpendicular velocity distribution of 2000 particles before and after their interaction with the electric and magnetic fields of a LH wave with $\alpha = 30$.

reaching the limits of applicability of the single particle approach followed until this point. Such modifications to the particles' distribution function may significantly alter the wave fields and only a self-consistent treatment of these (and other) effects can accurately model the long term evolution of the particle spectrum in these waves.

5. Discussion

We have identified plasma waves with spectral properties consistent with LH waves in PIC simulations of subrelativistic magnetized collisionless shocks. These simulations have shown that the LH waves excited at the shock region produce a temperature anisotropy in both electrons and ions. On average, ions (electrons) are more energetic in the direction perpendicular (parallel) to the shock background magnetic field. Electrons are shown to be accelerated to relativistic energies, however further investigation is required to understand if realistic plasma flow parameters would yield similar results. This ion temperature anisotropy is consistent with their stochastic acceleration in LH waves. A single particle approach is used to study the resonant interaction between ions and the fields of these waves. The results show that ions can be stochastically heated. Despite its limitations, this simplified approach provides deeper insight about the kinetic-scale phenomena underlying the acceleration of particles in subrelativistic collisionless shocks.

REFERENCES

Blandford, R. & Eichler, D. 1987 Particle acceleration at astrophysical shocks: A theory of cosmic ray origin. *Physics Reports* **154**, 1–75.

Bonoli, P. 1984 Linear theory of lower hybrid heating. *IEEE Transactions on Plasma Science* **12** (2), 95–107.

Boris, J.P. 1970 *Acceleration calculation from a scalar potential*.

Fonseca, R. A., Silva, L. O., Tsung, F. S., Decyk, V. K., Lu, W., Ren, C., Mori, W. B., Deng, S., Lee, S., Katsouleas, T. & Adam, J. C. 2002 OSIRIS: A Three-Dimensional, Fully Relativistic Particle in Cell Code for Modeling Plasma Based Accelerators. In *Computational Science ICCS 2002*, *Lecture Notes in Computer Science*, vol. 2331, pp. 342–351. Springer Berlin Heidelberg.

Karney, C. F. F. 1978 Stochastic ion heating by a lower hybrid wave. *Physics of Fluids* **21** (9), 1584–1599.

Martins, S. F., Fonseca, R. A., Silva, L. O. & Mori, W. B. 2009 Ion dynamics and acceleration in relativistic shocks. *The Astrophysical Journal Letters* **695** (2), L189.

Protheroe, R. J. & Clay, R. W. 2004 Ultra high energy cosmic rays. *PASA - Publications of the Astronomical Society of Australia* **21**, 1–22.

Spitkovsky, A. 2008*a* On the structure of relativistic collisionless shocks in electron-ion plasmas. *The Astrophysical Journal Letters* **673** (1), L39.

Spitkovsky, A. 2008*b* Particle acceleration in relativistic collisionless shocks: Fermi process at last? *The Astrophysical Journal Letters* **682** (1), L5.

Alfvén waves in magnetized plasmas: the bounce drift resonance

Fabrizio Del Gaudio

Instituto de Plasmas e Fusão Nuclear (IPFN), Instituto Superior Técnico, Avenida Rovisco Pais, 1049-001 Lisboa, Portugal

e-mail: fabrizio.delgaudio@tecnico.ulisboa.pt

Abstract. An extensive study of energetic particles in tokamaks is mandatory especially for their role in sustaining the ignition regime. We contribute to this know-how investigating the interaction of energetic α-particles with shearing Alfvén modes expected in large machines such as ITER or DEMO. In these large machines, shearing Alfvén waves can propagate not only along the magnetic field lines but also along the perpendicular direction, the electric field of such waves is capable to interact with energetic particles. We characterise this phenomenon from first principles, in a screw-pinch geometry using a test particle approach to compute the resonant condition and the energy growth rate for resonant particles.

Short bio. Fabrizio studied Energy and Nuclear Engineer at Politecnico di Torino, Italy. He obtained his master degree in 2015 with a thesis work on electron positron beams collision, in particular on disruption effect, hard photon emission and pair production. This topic has been developed at IST at IPFNs Group for Lasers and Plasmas.

He joined APPLAuSE following a passion for physics that comes from his childhood. His scientific education was originally oriented to technological problems associated to applied physics in Energy and Nuclear related topics, namely the design and project of energy related systems. More recently his interests shifted towards theoretical plasma physics. He is also interested in quantum electrodynamics, quantum physics, general relativity and plasma physics related to astrophysics.

Fabrizio gave private lessons to high school students, with whom he learnt how to explain concepts in a simple manner and to be patient. He enjoys sports, chess, guitar and photography.

1. Introduction

In burning plasmas relevant fraction of the total energy density belongs to charged fusion products. Tokamaks forecast for the future like ITER and DEMO will operate in this regime, where there is the need to address two major problems related to energetic particles: i) their confinement to maximize the energy transfer efficiency to the thermal plasma ii) how their interaction with collective plasma modes and turbulence may reduce the overall efficiency of the system (Chen & Zonca 2007). Energetic α particles are also capable of driving instabilities through their interaction with Alfvén waves (Hughes *et al.* 1978; Zonca *et al.* 2007). In this work we investigate the conditions and mechanism for these α particles to resonate with shearing Alfvén waves.

2. Screw-pinch equilibrium

The screw pinch configuration is suitable to study the bounce drift resonance from basic principles due to the simplicity of the drifts involved. In the MHD screw pinch equilibrium the magnetic surfaces are concentric cylinders and the field lines lay on these surfaces at given constant radius r with a given helicity defined by parameter

$$q = \frac{\int dz}{2\pi} = \frac{\int_0^{2\pi} B_z r d\theta}{2\pi B_\theta} = \frac{B_z r}{B_\theta}. \tag{2.1}$$

In this equilibrium configuration, for an imposed and constant longitudinal component B_z, the magnetic field in cylindrical coordinates reads

$$\begin{aligned} \vec{B}_0 &= B_z \frac{\sqrt{r^2+q^2}}{q} \hat{b}_0, \\ \hat{b}_0 &= \left(0, \frac{r}{\sqrt{r^2+q^2}}, \frac{q}{\sqrt{r^2+q^2}}\right). \end{aligned} \tag{2.2}$$

The resulting drifts, namely the curvature drift and the gradient drift, are all directed parallel to the magnetic surfaces, thus the gyro-centre of drifting particles lies on the same magnetic surfaces.

3. Gyrokinetic approach

We simulated the gyro-centre motion of our test particles in this configuration leveraging on the relevant equations of motion derived by Littljohn (Littlejohn 1983) for $\vec{x}$ position and U momentum parallel to the equilibrium magnetic field lines. In Littlejohn's approach the drifts up to first order in the gyro-radius are included and the equations read

$$\begin{aligned} \dot{\vec{x}} &= \frac{\hat{b} \times (\mu \nabla B - \vec{E}^*) + U \vec{B}^*/m}{\hat{b} \cdot \vec{B}^*} \\ \dot{U} &= \frac{\vec{B}^* \cdot (\vec{E}^* - \mu \nabla B)}{\hat{b} \cdot \vec{B}^*} \end{aligned} \tag{3.1}$$

where

$$\vec{B}^* = q_e \vec{B} + U \nabla \times \hat{b} \tag{3.2}$$

$$\vec{E}^* = q_e \vec{E} - U \dot{\hat{b}} \tag{3.3}$$

with m and q_e respectively the mass and the charge of the followed particle. The frequency of the shearing Alfvén waves is much lower than the gyrofrequency and allows us to solve only the motion of the gyro-centre without following the particle in its full gyromotion around the field lines, saving computational time. As shown in fig.1 the simulated trajectory lies on the same cylindrical surface of the equilibrium field line but with drift velocity on the z direction.

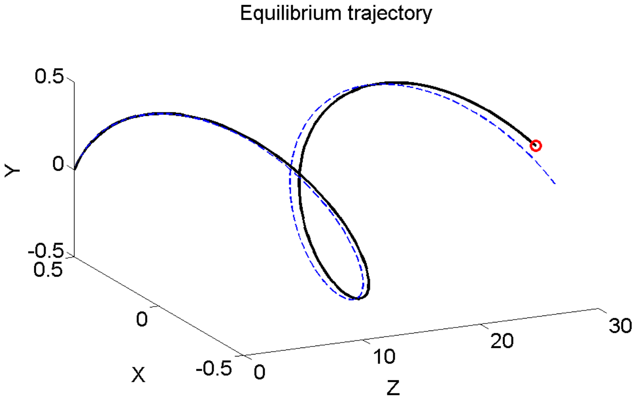

Figure 1: Trajectory described by the test particle gyro-centre (solid-black) in presence of the screw pinch equilibrium field, field line (dashed-blue).

4. Shearing Alfvén wave superimposition

In presence of Shearing Alfvén waves the motion of the particles may be modified and we investigated this possibility solving numerically the gyro-centre equations of motion in presence of a perturbing shearing Alfvén wave. Shearing Alfvén waves follows the dispersion relation condition $\omega = \kappa_{||} V_A$ where $V_A = B/\sqrt{\mu_0 \rho}$, μ_0 the vacuum permeability and ρ the plasma mass density. The electromagnetic field of the wave has been obtained imposing an amplitude much smaller than the equilibrium field, and a phase given by the Shearing Alfvén wave dispersion relation for a general wave-vector $\vec{k} = k_r \hat{n} + k_{||} \hat{b}_0 + k_p \hat{p}$. We express the fields in terms of the orthonormal base of versors indicated by the equilibrium magnetic field lines, $\hat{b}_0$ parallel to the field line, $\hat{n}$ in the direction perpendicular to the magnetic iso-surfaces and $\hat{p} = \hat{b}_0 \times \hat{n}$ defining the bi-normal plane. The field $\vec{B}_1$ is imposed with some constrains while the field $\vec{E}_1$ is calculated consistently from Faraday's law.

$$\vec{B}_1 = \xi B_0 e^{i(\vec{x}\cdot\vec{k}-\omega t)} \hat{b}_1 \tag{4.1}$$

$$\vec{E}_1 = B_1 V_A \hat{e}_1 \tag{4.2}$$

given the conditions $\vec{k} \cdot \hat{b}_1 = 0$ and $\hat{b}_1 \cdot \hat{b}_0 = 0$ follows

$$\hat{b}_1 = \frac{\vec{k} \times \hat{b}_0}{|\vec{k} \times \hat{b}_0|} = \frac{k_r}{k_\perp}\hat{p} - \frac{k_p}{k_\perp}\hat{n} \tag{4.3}$$

$$\hat{e}_1 = \frac{k_r}{k_\perp}\hat{n} + \frac{k_p}{k_\perp}\hat{p} \tag{4.4}$$

being $\xi \sim 10^{-4}$ a small scale factor indicating the relative amplitude of the wave compared to the equilibrium field. We can separate the effects of the perturbation and the equilibrium fields on the drifts since magnetic field and the differential operators in eq.3.1 are approximately

$$\vec{B} = \vec{B}_0 + \vec{B}_1 \quad \text{and} \quad \hat{b} = \vec{B}/B \simeq \vec{B}/B_0 \tag{4.5}$$

$$\nabla B \simeq \nabla B_0 \tag{4.6}$$

$$\dot{\hat{b}} \simeq \frac{\dot{B}_1}{B_0}\hat{b}_1$$

$$\nabla \times \hat{b} \simeq \nabla \times \hat{b}_0 + \frac{B_1}{B_0}\nabla \times \hat{b}_1 + \frac{\nabla B_0 \times \hat{b}_0}{B_0} + \frac{\nabla B_1 \times \hat{b}_1}{B_0}.$$

Solving the equations of motion for the gyro-centre with the superimposed wave, we computed whether our test particle is in resonance or not with the wave $\vec{k}\cdot\dot{\vec{x}}-\omega = 0$, and the power transfer to the particle $\mathit{\Gamma}_E = \vec{E}\cdot\dot{\vec{x}}$ thus its energy growth rate. In cylindrical coordinates we cannot solve the aforementioned equations. In fact the position vector, that links the origin with the actual position of the particle, can not be represented with the cylindrical versors base without losing information on the angular position of the particle.

$$\vec{x} = \sum_{i=1}^{3} x_i\hat{e}_i, \quad \hat{e}_i = \hat{e}_{r,\theta,z} \quad \vec{x}\cdot\hat{e}_\theta = 0. \tag{4.7}$$

The position can be represented stepping through the Cartesian coordinate or more conveniently using the covariant formalism. For cylindrical geometry the metric tensor reads:

$$g_{\mu,\nu} = \begin{pmatrix} 1 & 0 & 0 \\ 0 & r^2 & 0 \\ 0 & 0 & 1 \end{pmatrix} \tag{4.8}$$

and the transformation from cylindrical components to the covariant or contravariant components is given by

$$A^\mu = \sqrt{g^{\mu,\nu}}A_{(\nu)}, \quad A_\mu = \sqrt{g_{\mu,\nu}}A_{(\nu)}, \tag{4.9}$$

given the metric tensor being diagonal $g^{\mu,\nu} = g^{-1}_{\mu,\nu}$, wave-vector and electric field $\vec{k}$, $\vec{E} \to$ covariant and velocity $\dot{\vec{x}} \to$ contravariant.

5. Results

This approach does not account self consistently for the non linear interaction wave-particle, thus the wave is not damped, our results are limited to the early times of the interaction and we followed our particle for no more than 10 wave cycles. In the early time of the interaction the particle drift velocity is not affected by the wave perturbation since its magnitude is small compared to the equilibrium field. In this scenario, after few wave cycles, it is possible to take an "instantaneous picture" of the energy rate gained by the particle during its interaction with the wave.

In fig. 2 we show the condition for a particle to be in resonance with the wave, as a function of the wave mode perpendicular to the equilibrium field $k_\perp$ and of the initial energy of the particle in units of $mV_A^2/2$. If there are no transverse modes, $k_\perp = 0$, the only particles allowed to be in resonance with the wave are the ones travelling at V_A along the field lines, as represented in fig. 2. This characteristic is also obtained if we substitute in the inner product the drift velocity due to the equilibrium fields, in case of

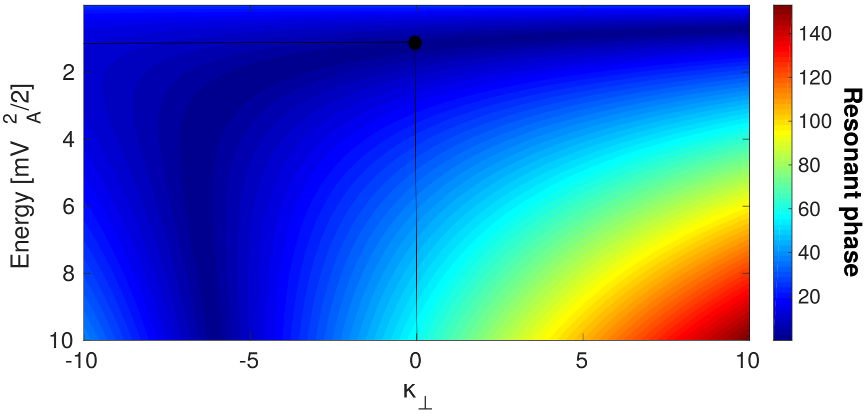

Figure 2: The resonant condition requires $\vec{k}\cdot\dot{\vec{x}}-\omega=0$, highlighted by the dark-blue region of this picture, here expressed as a function of the perpendicular k of the wave and of the initial energy of the particle. For $\kappa_\perp=0$ the resonant particles are the ones travelling at V_A along the field lines as expected (black dot).

negligible radial component of k

$$\begin{aligned}\omega &= \vec{k}\cdot\hat{\vec{x}}\\ V_A k_{\|} &= (k_{\|}\hat{b}_0 + k_\perp \hat{p})\cdot\frac{\hat{b}_0\times\mu\nabla B_0 + U\vec{B}^*/m}{\hat{b}_0\cdot\vec{B}^*}\\ k_\perp &= k_{\|}\left(\frac{mV_A}{U}-1\right)\frac{\hat{b}_0\cdot\vec{B}^*}{\hat{p}\cdot\vec{B}^*}\end{aligned}\tag{5.1}$$

with all vectors expressed with their covariant/contravariant components. Equation 5.1 shows that in order for a particle, travelling at the Alfvén speed, to be resonant with the wave $k_\perp$ must be 0.

Given the particles being in resonance one can compute their energy growth rate for early times, sufficiently small for the particle not to gain enough energy to escape the resonance. This energy growth rate is shown in fig. 3 where is shown that more energetic particles possess a higher energy growth rate. This higher growth rate indicate that the more energetic particles will leave the resonance with the wave earlier than the less energetic ones. The estimate of the net energy gain during the whole resonant interaction function of the initial energy of the particle is left to future efforts. On the line of the resonance one can extract a curved line-out from fig.3 that shows the energy growth rate for the particle in perfect resonance $\vec{k}\cdot\dot{\vec{x}}-\omega=0$, it is shown in fig. 4. The energy growth rate is linear with respect to the particle initial energy, since both curvature and gradient drift velocities are proportional to the particle energy. The energy gain rate is higher for faster particles as in the same period of time the electric field of the wave is able to exert a larger work as their travelled distance is higher.

6. Conclusions

In this work we investigated the bounce-drift resonance of energetic α-particles with shearing Alfvén waves. In the scenario of large tokamaks, shearing Alfvén modes transverse to the equilibrium field are allowed and play a decisive role in the particle resonance mechanism. These modes permit the electric field of the wave to effectively perform work on the resonant particles due to their drift velocity. This is possible as not only particles

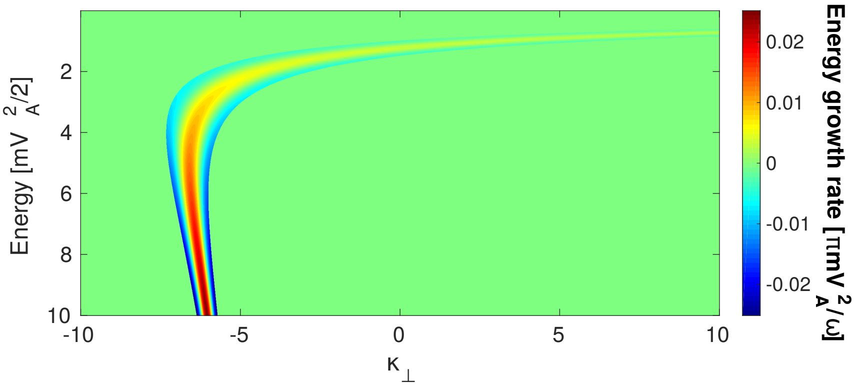

Figure 3: Energy gain rate function of the perpendicular wave mode $k_\perp$ and initial energy of the resonant particles.

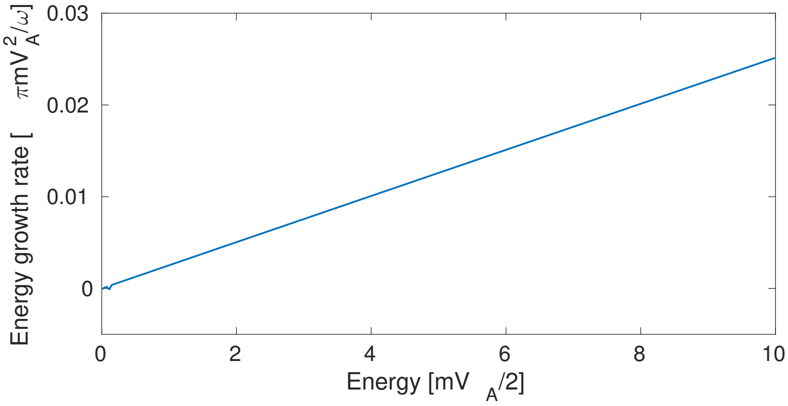

Figure 4: Energy gain rate function of initial energy for perfectly resonant particles.

travelling at the Alfvén speed along the field lines are resonant with the wave. In this work, we calculated the resonance condition numerically and analytically and computed the relevant energy growth rate of the bounce drift resonance for shearing Alfvén waves and energetic α-particles.

Acknowledgements

The author thanks the financial support for IST activities received from the Fundação para a Ciência e Tecnologia through project UID/FIS/50010/2013.

REFERENCES

Chen, L. & Zonca, F. 2007 Theory of alfvn waves and energetic particle physics in burning plasmas. *Nuclear Fusion* **47** (10), S727.

Hughes, W. J., Southwhood, D. J., Mauk, B., Mcpherron, R. L & Barfield, J. N. 1978 Alfven waves generated by an inverted plasma energy distribution. *Nature* **275** (5675), 43–45.

Littlejohn, Robert G. 1983 Variational principles of guiding centre motion. *Journal of Plasma Physics* **29**, 111–125.

Zonca, F., Buratti, P., Cardinali, A., Chen, L., Dong, J.-Q., Long, Y.-X., Milovanov, A.V., Romanelli, F., Smeulders, P., Wang, L., Wang, Z.-T., Castaldo, C., Cesario, R., Giovannozzi, E., Marinucci, M. & Ridolfini, V. Pericoli 2007 Electron fishbones: theory and experimental evidence. *Nuclear Fusion* **47** (11), 1588.

Update of the IPFN High-temperature Spectral database for CO_2

João F. Vargas

Instituto de Plasmas e Fusão Nuclear (IPFN), Instituto Superior Técnico, Avenida Rovisco Pais, 1049-001 Lisboa, Portugal

e-mail: joao.francisco.vargas@gmail.com

Abstract. Mars has been a tempting target for space exploration due to it's proximity to Earth. Due to the high contents of carbon dioxide in the atmosphere it is of considerable interest to understand radiation by this molecule to compute the radiative heating caused by the atmosphere upon spacecraft entering. In this work, the in-house IPFN spectral database for CO_2 is updated and some preliminary checks are done to ensure the consistency of this database. A Beer-Lambert solver, to compute radiation transfer through a gas, was also developed to check for this consistency. It is found that the absorption and emission coefficients of the updated database must be checked against other databases before proceeding further.

Short bio. João studied Physics Engineering at IST finishing his MSc in 2015 with the thesis titled “Improvement of state-resolved kinetic models applied to N2-CH4 hypersonic entry flows”.

In the past, João has participated in the activities of the Physics Students Board of IST, first as a volunteer, later as Vice-President and now as a member of the Fiscal and Disciplinary Board of this organization. A space exploration enthusiast, he is focused in modelling on aerothermodynamics and hopes one day to go to space.

1. Introduction

As the interest in Mars exploration arises, there is a need to update and check High-Temperature spectral databases for CO_2. The database currently used at IPFN was scanned in the early 2000's using an Optical Character Recognition (OCR) scan from the known HITRAN database published by Rothman *et al.* (1992). Since this scan was never double-checked for possible scanning errors, these errors persisted through the years and were featured in the digital version of the database. The errors started being detected as features on the CO_2 spectrum which should not exist. The first step of this work was then to rescan the database and compare it with the current digital version in order to minimize the number of errors. The second part of this work was to validate the new database by simulating the radiative transfer in two distinctive cases. For this, a radiative transfer code was developed in Fortran and two test cases were selected. The first test case represents an easy and simple way to observe the desired characteristics and performance of the developed code. The second test case concerns a real life application of a plasma torch (Depraz *et al.* 2012).

In this work, the spectral region of interest is in the infrared region, around 2.7 μm. Transitions of CO_2 that emit radiation on this region are between vibrational-rotational levels:

$$\mathrm{CO_2(v',j')} \longrightarrow \mathrm{CO_2(v'',j'')} + \mathrm{h}\nu.$$

The HITRAN database is divided in two parts: Spectroscopic Data and Intensity Parameters. Spectroscopic Data contains the information on how to compute all levels of $\mathrm{CO_2(v',j')}$ and Intensity parameters that relate the existing vibrational transitions with the intensity and frequency of the radiation. For detailed information consult Rothman *et al.* (1992).

2. Methods

2.1. *Scanning and checking the Database*

The first approach to scanning the database was to perform an OCR scan on a digital scan of the original document. Three different OCR softwares were tried, including a trial version of a commercially available software instead of a free software, but failed to produce a scan with sufficient quality of the database. Instead, the database was converted to a digital format manually. After digitizing the database, the new digital version was compared with the old one and checked for agreement. Table 1 summarizes the number of disagreements (errors) found in each part of the database (Spectroscopic Data and Intensity Parameters). The old version (Previous scan errors) had a greater number of errors than this work's hand digitizing (this work's errors). Do note that it is still possible that the current version of the database still contains errors due to the possibility that the same error was done while manually digitizing the database and by the OCR software in the past. While comparing both entries to the database a disagreement would not show and the error would persist.

The next step after updating the database is to use the in-house IPFN code to compute the absorption and emission spectra of the gas. This was performed at temperatures of 1000 K and 3000 K. Figures 1-2 plot the Infrared (IR) band of interest of CO_2 absorption and emission spectra for a 1000 K pure CO_2 gas. The red lines were created using the old database while the blue lines were done using the new. The main discrepancy in these figures is the existence of a high peak using the old database which disappears with the new one. This was the main error that motivated this work. The two databases superimpose except in a small region near the 0.35×10^{-6} m wavelength in which the

	Entries	Errors detected	Previous scan errors	This work's errors
S.D.	556	129	96	33
I.P.	603	19	13	6

Table 1: Summary of the work done on the HITRAN database (Rothman *et al.* 1992). The database is divided in Spectroscopic Data (S.D.) and Intensity Parameters (I.P.).

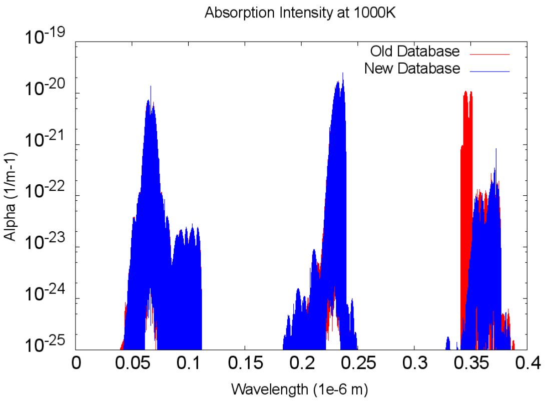

Figure 1: Absorption spectra of CO_2 at 1000K in the IR region.

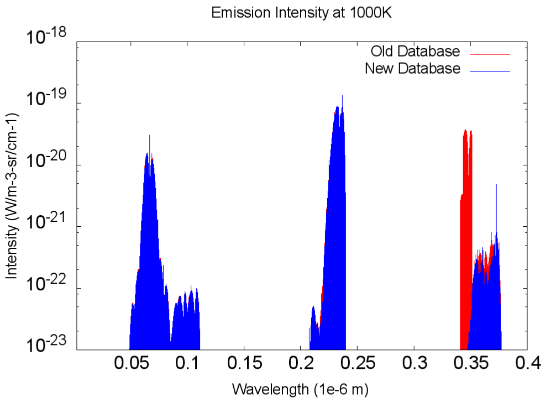

Figure 2: Emission spectra of CO_2 at 1000K in the IR region.

old database overestimates the coefficients of CO_2. The same happens in figures 3-4 in which the absorption and emission spectra are plotted for a 3000 K pure CO_2 gas. In the latter figures a shoulder on the region of 0.2×10^{-6} m wavelength also disappears.

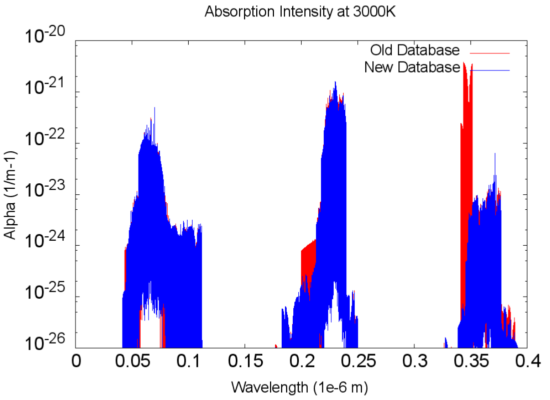

Figure 3: Absorption spectra of CO_2 at 3000K in the IR region.

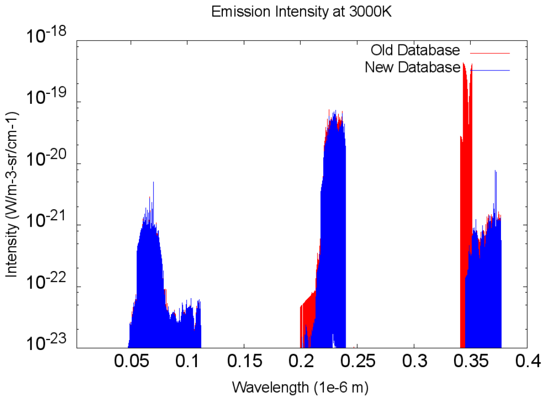

Figure 4: Emission spectra of CO_2 at 3000K in the IR region.

2.2. *Radiation Transfer*

For this work, two test cases were chosen to ensure that no major errors were still in the database. In the first case 1 mole of CO_2 at 3000 K precedes 1 mole of CO_2 at 1000 K. Both cells are considered to be 1 meter long. This case will be referred to as the Academic Case and it was designed to check for the smoothness of the curve and the absorption of the central peaks of the hotter gas (which are broader by Doppler broadening) by the colder gas.

The second case was taken from an experiment performed by Depraz *et al.* (2012). In this work by Depraz, some theoretical calculations are also presented. These calculations are the same as in this work although with different codes and with different databases. Depraz uses databases CDSD-4000 (Tashkun & Perevalov 2011) and HITELOR (Scutaru *et al.* 1994). A CO_2 plasma torch at atmospheric pressure is lit inside a cylindrical tube, the light emitted by the plasma is then collimated and analyzed by a Fourier Infrared spectrometer. Light used for this analysis was captured at 6 cm from the torch's base using a sapphire or a quartz window. Absorption from the sapphire window is considered to be constant in the relevant spectrum region while in the quartz window a correction must be accounted for. Figure 5 displays the experimental setup used while figure 6 a typical radial profile for the molar density of relevant species in the intended spectral window and temperature of the plasma torch. The profile used for the simulations looks much alike the one in figure 6 with the difference that this one was obtained using a quartz window and the one used in this work was obtained with a sapphire one. The only species considered in the calculations for this case are CO_2 and CO since these are also the ones considered by Depraz *et al.* (2012).

In order to use these databases in ray tracing applications (for example) a previous test is required. As such a numerical solver was developed to solve the following equation, Beer-Lambert's law:

$$\frac{dI(\nu)}{dl} = \epsilon(\nu) - \alpha(\nu)I(\nu) \tag{2.1}$$

where $I(\nu)$ is the radiation intensity (W/sr/cm^{-1}), $\epsilon(\nu)$ the emission coefficient (W/sr/cm^{-1}/m) and $\alpha(\nu)$ the absorption coefficient (1/m). Intuitively, a group of photons with intensity I and frequency ν has it's value changed according to the properties of the gas which can emit some radiation by itself ($\epsilon(\nu)$) and can absorb some ($\alpha(\nu)$) depending on how much there is to start with. A continuous gas profile is discritized and divided into cells where the properties of the gas are considered to be constant. Integrating along the path and discretizing the solution yields the numerical scheme as it is done in da Silva *et al.* (2008):

$$I_n(\nu) = \frac{\epsilon_n(\nu)}{\alpha'_n(\nu)}\left[1 - \exp\left(-\alpha'_n(\nu)x_n\right)\right] + I_{n-1}(\nu)\exp\left(-\alpha'_n(\nu)x_n\right) \tag{2.2}$$

with x_n being the length of cell n and $\alpha'_n(\nu)$ being the absorption coefficient corrected for self-absorption by the plasma:

$$\alpha'_n(\nu) = \alpha_n(\nu)\left[1 - \exp\left(-\frac{h\nu}{k_B T_n}\right)\right], \tag{2.3}$$

with h the Planck constant, k_B the Boltzmann constant and T_n the temperature of the gas in the cell. The developed code takes as input a spatial 1D profile with information on the temperature, spectral emission and absorption profiles and the length of each cell. The code outputs the spectral profile of emitted intensity after each cell absorption and emitted radiation. By integrating the result along the spectrum the total intensity of the radiation is computed. The emission and absorption spectral profiles are provided by the in-house IPFN line-by-line radiation code SPARTAN (da Silva *et al.* 2016).

3. Results

In figure 7 the results for the radiative transfer of the so called Academic Case is presented for the considered spectral region with the red line being the radiation from the 3000 K gas and the blue line the 1000 K gas. The interesting part is the selected

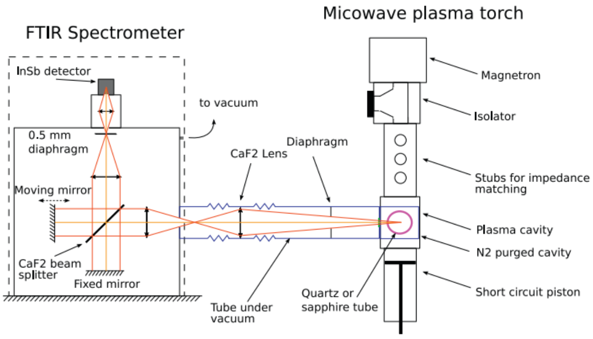

Figure 5: Experimental setup of the work by Depraz *et al.* (2012). A microwave plasma torch is turned on inside a tube.

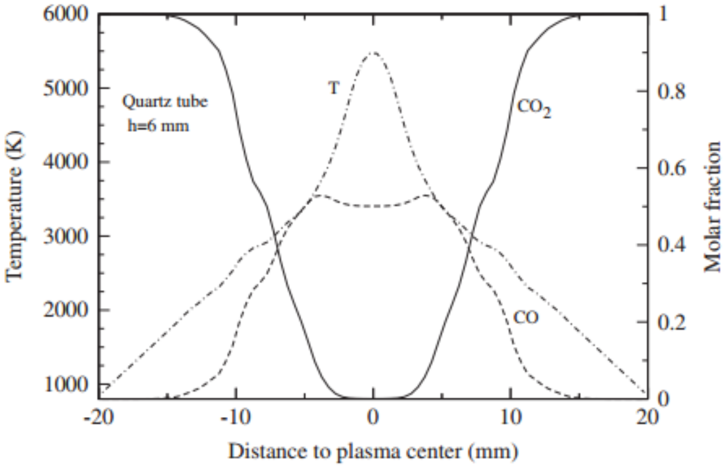

Figure 6: Equilibrium radial profile example obtained in the work of Depraz *et al.* (2012).

detail in figure 8 with the same colour code. It features a smaller part of the same spectral region focusing on the radiation peaks. As the radiation lines coming out of the hotter gas (in red) have a larger Doppler broadening than the absorption and emission lines of the colder gas (in blue) the central peaks are absorbed by the colder gas but not the rest of the broadened line. The net result is the blue line in which one line is apparently divided in two but actually, radiation lines are absorbed by the colder gas differently than they were emitted by the hotter gas. This feature in figure 8 was expected and this test-case was thought out to have this kind of result. This configuration allows us to see the resolution and the smoothness of the developed code.

Figure 9 presents the radiative transfer of the plasma torch experiment by Depraz *et al.* (2012). Presented lines represent theoretical calculations (yellow and blue) and the experimental result (green) and this work's result (purple). Although the order of magnitude is the same, the shape of the first three lines are not in agreement with this work's calculations. As it is, a single reason cannot be pinpointed for the unsatisfactory result. The first thing that should be done is to compare the emission and absorption coefficients of each database to check if they are compatible. When this comparison is done, several reasons could be the cause of the mismatch between this work and Depraz *et al.* (2012).

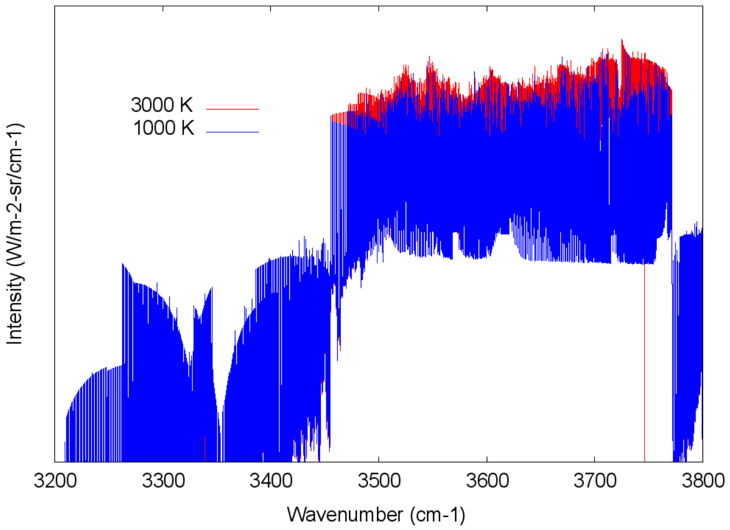

Figure 7: Radiative transfer in the whole examined spectral region for the Academic Case. The red line is the radiation from the 3000 K gas and the blue line is the 1000 K gas.

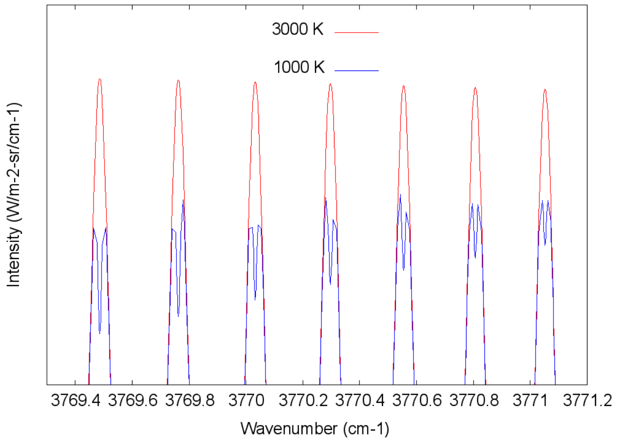

Figure 8: Radiative transfer for the Academic Case detail. The red line is the radiation from the 3000 K gas and the blue line is the 1000 K gas.

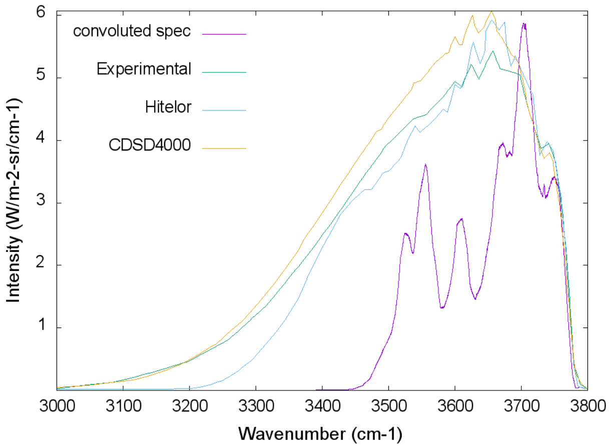

Figure 9: Radiative transfer on the examined spectral region.

4. Conclusions

Though in this work we were not successful in the application of the second test case, IPFN's spectral database for CO_2 has been successfully updated and corrected save if the exact same mistake was done when digitizing the database before and in this work. This updated version of the database was used to produce a spectrum for CO_2 radiation which did not contain any obvious errors unlike the previous version of the database. A Beer-Lambert 1D code was successfully developed although not yet optimized, it was used to observe the features that are expected for such an input with such a code in the first studied case and served as a warning for future applications of the database without further study and comparison of the available databases. Such comparison must start with the absorption and emission coefficients of the different databases and the interpretation of these comparisons.

REFERENCES

Depraz, S., Perrin, M.Y., Rivire, Ph. & Soufiani, A. 2012 Infrared emission spectroscopy of {CO2} at high temperature. part i: Experimental setup and source characterization. *Journal of Quantitative Spectroscopy and Radiative Transfer* **113** (1), 1 – 13.

Rothman, L.S., Hawkins, R.L., Wattson, R.B. & Gamache, R.R. 1992 Energy levels, intensities, and linewidths of atmospheric carbon dioxide bands. *Journal of Quantitative Spectroscopy and Radiative Transfer* **48** (5), 537 – 566.

Scutaru, D., Rosenmann, L. & Taine, J. 1994 Approximate intensities of co2 hot bands at 2.7, 4.3, and 12m for high temperature and medium resolution applications. *Journal of Quantitative Spectroscopy and Radiative Transfer* **52** (6), 765 – 781.

da Silva, M. Lino, Lopez, B. & Espinho, S. 2016 Spartan code. *User Manual* Retrieved, 5th May at esther.ist.utl.pt.

da Silva, M Lino, Vacher, D, Dudeck, M, Andr, P & Faure, G 2008 Radiation from an equilibrium co 2 n 2 plasma in the [250850nm] spectral region: Ii. spectral modelling. *Plasma Sources Science and Technology* **17** (3), 035013.

Tashkun, S.A. & Perevalov, V.I. 2011 Cdsd-4000: High-resolution, high-temperature carbon dioxide spectroscopic databank. *Journal of Quantitative Spectroscopy and Radiative Transfer* **112** (9), 1403 – 1410.

Edge instabilities between ELMs at JET

Luís Gil

Instituto de Plasmas e Fusão Nuclear (IPFN), Instituto Superior Técnico, Avenida Rovisco Pais, 1049-001 Lisboa, Portugal

e-mail: luis.gil@tecnico.ulisboa.pt

Abstract. Edge inter-ELM quasi-coherent modes in density have been observed in the JET tokamak. These were measured in high performance baseline and hybrid scenarios with reflectometry and interferometry diagnostics at the low-field side of the machine, but are not detected by magnetic coils. The modes are not universal occurrences, as they do not appear before every ELM, but they may play a role in turbulent transport at the pedestal for some situations, possibly affecting the ELM cycle.

Short bio. Luís has an MSc degree in Engineering Physics from IST with a thesis on nuclear fusion titled ‘Investigation of the effect of divertor geometry on the L-H transition using reflectometry diagnostics”. Before the start of APPLAuSE he participated in the experimental campaigns of the Joint European Torus to study instabilities in fusion plasmas.

His interest in plasmas and nuclear fusion started from concerns about energy sustainability and climate change. This interest grew stronger after his first course in plasma physics at the Polytechnic University of Milan during the Erasmus Programme. It was strengthened with further courses at IST and eventually led him to work at IPFN from the MSc thesis onwards.

Besides science, he loves sports and pursues a healthy lifestyle, practicing ultimate frisbee and weightlifting. He also enjoys music and has been playing the electric guitar since he was ten years old.

1. Introduction

The high confinement state known as H-mode is the preferable operational regime for a fusion reactor (Wagner 2007) and it is characterized by a region of reduced particle and energy transport at the edge of the plasma called the pedestal (Urano 2014). Steady state operation in H-mode is generally accompanied by bursty edge perturbations known as edge localized modes (ELMs) (Leonard 2014). Although small ELMs have the beneficial effect of flushing impurities out of the plasma, they limit the achievable pedestal pressure and large ELMs can deliver unacceptably high heat loads to the divertor. Since the pressure at the top of the pedestal has a strong impact on fusion performance (Kinsey *et al.* 2003), it is crucial to determine under what conditions a high pedestal may be achieved in conjunction with tolerable ELMs. This requires the physics understanding of the processes in play to be improved.

The H-mode pedestal is characterized by a strong pressure gradient and large current, as illustrated in figure 1. These are driving forces of the peeling-ballooning (P-B) instability, which is believed to be the cause of ELMs (Snyder *et al.* 2002). This view is supported by different reasons, including the fact that no device has been observed to operate above the P-B instability threshold and numerous observations of ELMs which are triggered when this threshold is achieved (Groebner *et al.* 2013).

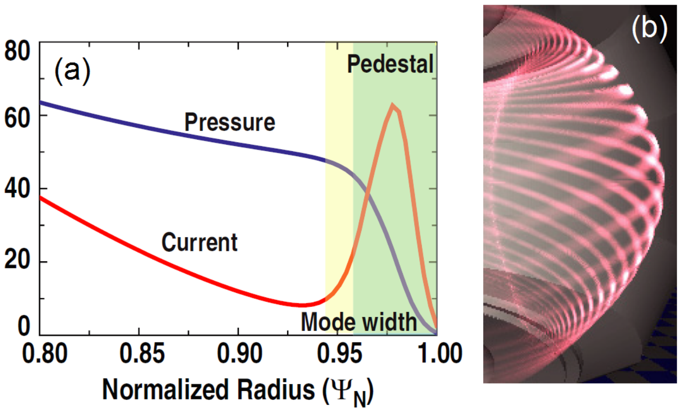

Figure 1: (a) Typical H-mode pressure and current profiles with the pedestal region dark shaded and the P-B mode width light shaded. (b) Calculated 3D structure of an n = 18 P-B mode in the DIII-D tokamak (Snyder *et al.* 2011).

The pedestal structure and ELM cycle are also believed to be affected by other types of instabilities, namely small-scale localized instabilities such as kinetic-ballooning modes (KBMs) (Dickinson *et al.* 2012; Groebner *et al.* 2010). The hypothesis used in EPED, the leading model in predicting pedestal width and height of present devices, is that KBMs cause significant transport in the pedestal, providing a local limit of pressure gradient due to their stiff onset (Snyder *et al.* 2011). The pedestal height and width then evolve along the KBM stability boundary until the P-B threshold is reached and an ELM occurs. These hypotheses allow a unique determination of the pedestal height and width before the ELM onset. Although many EPED predictions have been successfully compared against experimental data, there are some unexplained cases and direct observations of the underlying instabilities remain difficult and rare. Experimental studies of edge instabilities are thus required to achieve an accurate physics understanding of the pedestal structure and ELM cycle.

This paper presents measurements of edge inter-ELM instabilities in high performance pulses of the JET tokamak using reflectometry and other diagnostics. It is worth noting that inter-ELM instabilities compatible with KBMs have been previously detected with reflectometry in DIII-D (Diallo *et al.* 2015*b*) and C-Mod (Diallo *et al.* 2015*a*), but not in JET. The structure of the paper is as follows. Section 2 briefly describes the KG8C reflectometer at JET, which was the main diagnostic used in this work. Section 3 characterizes the measured fluctuations between ELMs and discusses their universality and correlation with the evolution of edge electron temperature. Finally, a brief summary and conclusions are presented in section 4.

2. Diagnostic setup

The main diagnostic used for this work was an X-mode hopping reflectometer at JET called KG8C. It features 2 channels with a probing frequency range of 75 to 110 GHz, sampling frequency up to 200 MHz with I/Q detection and 2 possible antenna angles, one with normal incidence for conventional reflectometry and the other with oblique incidence for Doppler backscattering. In this work only the normal incidence angle, whose corresponding line of sight is represented in figure 2, was used.

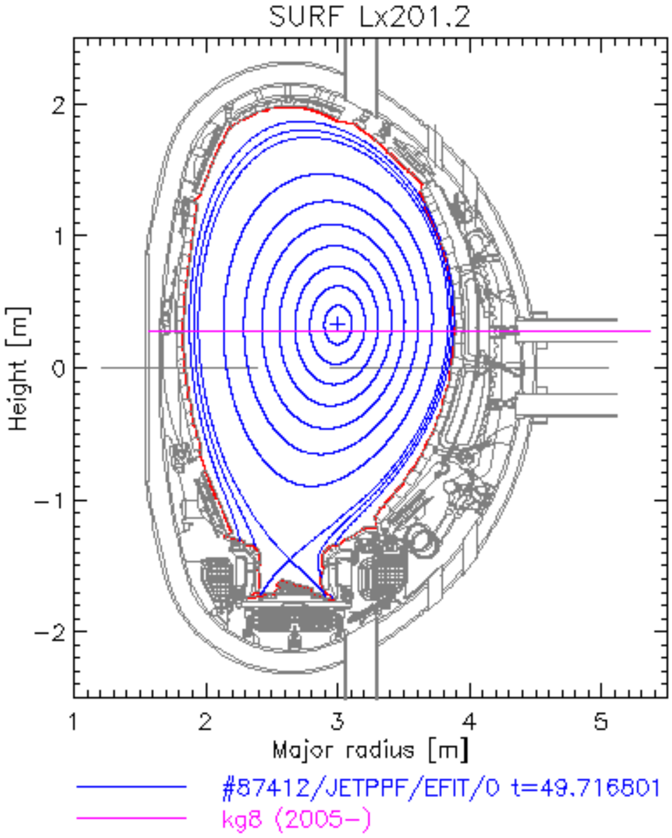

Figure 2: Cross-sectional view of JET showing the line of sight of the KG8C antenna (purple).

The X-mode cutoff depends on density and magnetic field, which implies that the probing location of the KG8C reflectometer depends on the radial profiles of both quantities. Figure 3 shows the plasma parameters accessible by the reflectometer, with the top axis showing the local magnetic field at the cutoff layer and the bottom axis representing the corresponding magnetic field at the center of the device, assuming a magnetic field inversely proportional to the major radius and reflection of the waves occurring at 3.8 meters, which is the usual location of the pedestal in JET. Since the pedestal density can typically cover a range of about 1 to $7 \times 10^{19}\,\mathrm{m}^{-3}$, a magnetic field of at least 2.5 T at the centre is desirable to probe a significant portion of the pedestal. However, with the current probing frequency range, the reflectometer cannot usually cover the entire pedestal for a single magnetic field value.

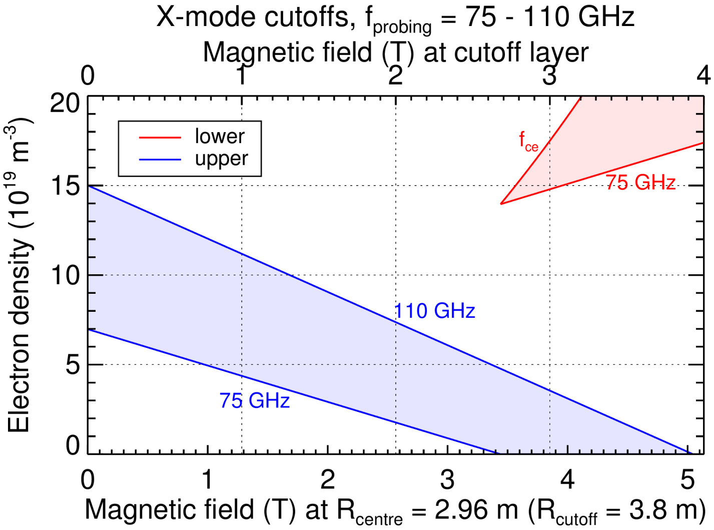

Figure 3: Plasma parameter space accessible by the KG8C reflectometer in terms of electron density and magnetic field. The solid lines show the X-mode cutoffs at the minimum and maximum probing frequencies of the reflectometer, delimiting the shaded areas at in-between frequencies. The blue and red colors correspond to the upper and lower cutoffs, respectively. The white areas are not accessible with the current setup.

3. Results and discussion

The 12 pulses analyzed for this work are presented in table 1 with the corresponding main plasma quantities and operation parameters taken from the control room pulse summaries. These belong to two high performance experiments from the C32-33 campaign of 2014: the M13-31 baseline scenario (pulses 87381-87412) and the M13-33 hybrid scenario (pulses 86603-86615). They were chosen for having a high heating power for a significant amount of time and achieving a high beta.

An example of strong edge density fluctuations between ELMs detected with the KG8C reflectometer is presented in figure 4(a). A quasi-coherent mode with central frequency of about 110 kHz appears about 20 ms before two ELMs during the 95 GHz and 100 GHz probing periods, respectively. The ELMs are easily identified by the spikes in the Be II line radiation, shown in the bottom plot. The red line of figure 5 shows the power spectrum of the complex reflectometry signal before the ELM during the 100 GHz period. The mode has a broad spectrum covering a frequency range of about 110 ± 40 kHz and harmonics. The figure also shows another spectrum of reflectometry, in blue, with the same probing frequency, which corresponds to a time period before a different ELM of the same pulse. In this case, the mode is not clearly visible, there being only a slight peak at the fundamental frequency and no harmonics. This illustrates the fact that the amplitude of the mode can be very different, even for apparently similar plasma conditions. In fact, for most ELMs the mode is not even detected.

One of the challenges associated with detecting inter-ELM instabilities with hopping reflectometry is the impossibility of probing all locations simultaneously. When the mode

Pulse	B_t (T)	I_p (MA)	P_{NBI} (MW)	P_{ICRH} (MW)	P_{tot} (MW)	$n_e\,dl$ ($10^{19}\,\mathrm{m}^{-2}$)	T_e (KeV)	β_N	KG8C	KG1
87412	3.3	3.5	27.2	3.7	30.9	23.7	5.9	1.4	6	9
87398	2.8	3.0	26.0	3.9	29.9	15.3*	7.6*	1.4	0	1
87392	2.6	2.8	27.3	4.0	31.3	14.7*	8.0*	1.7	0	3
87385	3.3	3.6	25.9	4.4	30.3	22.3*	5.3*	1.3	0	0
87384	3.3	3.6	23.9	4.1	28.0	21.2*	4.7*	1.1	0	0
87381	3.0	3.2	23.7	4.0	27.7	18.6*	4.9*	1.4	0	0
86615	2.9	2.5	15.1	4.6	19.7	13.7	7.9	2.0	0	6
86614	2.9	2.5	22.2	3.8	26.0	16.1	8.2	2.2	8	16
86613	2.9	2.5	21.2	4.1	25.3	13.8	8.1	2.1	0	0
86612	2.9	2.5	22.3	4.0	26.3	13.0	7.5	2.0	0	4
86608	2.9	2.5	22.5	3.6	26.1	16.5	7.5	1.9	8	20
86603	2.9	2.5	24.9	4.9	29.8	12.6	7.1	1.9	5	8
Total	-	-	-	-	-	-	-	-	27	67

Table 1: Main plasma quantities and operation parameters of the analyzed pulses (from left to right): pulse number; magnetic field at the device center; plasma current; neutral beam injection (NBI) power; ion cyclotron resonance heating (ICRH) power; total external power (NBI + ICRH); core line-integrated electron density; core electron temperature; normalized Beta (normalized ratio of plasma pressure to magnetic pressure). The last two columns contain the number of ELMs before which a quasi-coherent mode was detected in the KG8C reflectometer and KG1 interferometer, respectively.

*value not available in the pulse summary and therefore taken from the time instant where the electron pressure at the magnetic axis was maximum

is localized in space and time, it may be missed due to the use of the wrong probing frequency at the right time or vice-versa. To mitigate this limitation, an edge chord of the KG1 interferometer was also used to measure density fluctuations. It cannot precisely localize the mode in space, but it can always localize it in time. The spectrogram of figure 4(b) shows that the mode seen by the interferometer is in agreement with reflectometry, except for its harmonics, which are absent in the former. This suggests that the harmonics are artifacts caused by nonlinear reflectometry phenomena.

The mode is not detected by magnetic coils in the low-field side, as the spectrogram of figure 4(c) shows. However, there are many other fluctuations at different frequencies correlated with the ELM cycle in the magnetic signal, both broadband and coherent, and some also appear to be correlated with the density quasi-coherent mode. The absence of the mode in the magnetic signals suggests that it is not a KBM and may be an electrostatic instability, but this will addressed in future work.

To study the impact of the mode on pedestal transport and structure, the edge electron temperature was measured by electron cyclotron emission (ECE) at different radial positions. The time evolution of the temperature measured by 3 ECE channels is presented in figure 4(d). There is an apparent correlation between the appearance of the mode and the saturation or decrease of electron temperature. This suggests the mode may intensify turbulent transport, causing increased energy losses and possibly playing a role in the pedestal structure and ELM cycle. However there are cases when the mode does not appear and the temperature still saturates, so this requires further investigation.

It must be stressed that these observations are not universal, since the mode does not appear before most ELMs. The frequency of the mode is not always the same and in

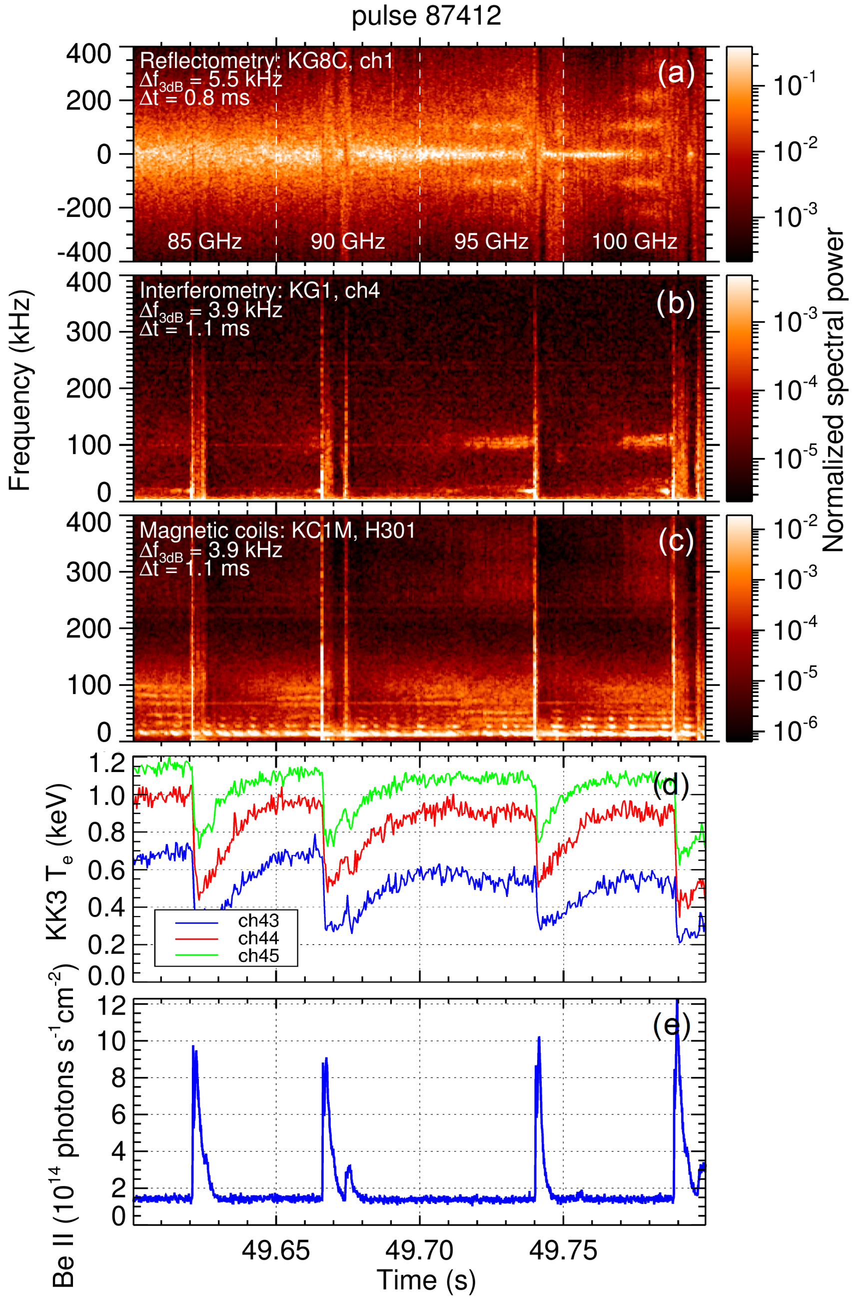

Figure 4: Spectrograms of reflectometry (a), interferometry (b) and magnetic coils (c), edge electron temperature (d) and Be II line radiation intensity (e), across three ELM cycles.

some pulses it is around 60 kHz. The last two columns of table 1 indicate the number of ELMs before which a quasi-coherent mode was detected in the KG8C reflectometer and KG1 interferometer, respectively, for the 12 pulses analyzed in this work. There were 4 pulses without any detection and 5 with less than 10 detections, but each pulse has dozens of ELMs.

4. Summary and conclusions

To summarize, edge inter-ELM quasi-coherent modes in density have been detected in high performance baseline and hybrid scenarios at JET with reflectometry and interferometry diagnostics. These are not universal occurrences, but may play a role in certain

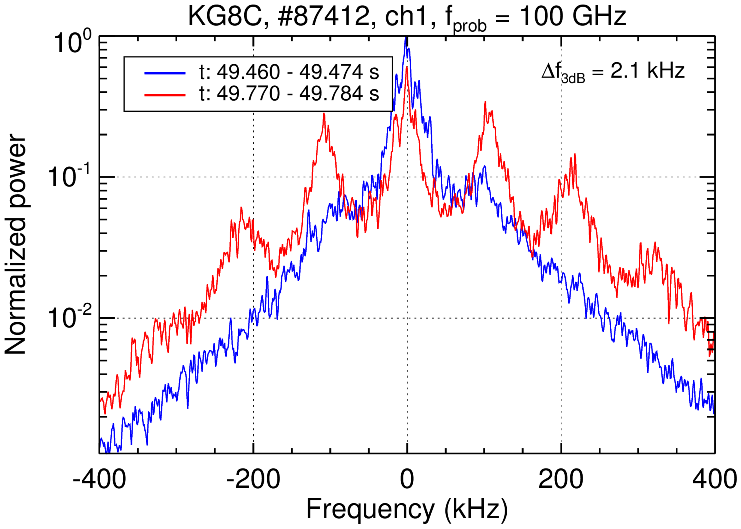

Figure 5: Reflectometry spectra of two time periods between different ELMs.

regimes. Further work must be done to figure out what type of pulses the mode appears in, namely the analysis of many shots with similar and different parameters, followed by a detailed comparison of cases with and without the mode. Hopefully this will clarify the importance of this mode and further motivate its characterization, localization and determination of its relation with plasma conditions, in order to identify the underlying instability, which may also require gyrokinetic simulations. Ultimately this will unravel the impact of the mode in turbulent transport, pedestal structure and ELM cycle.

Acknowledgments

The author gratefully acknowledges contributions from Carlos Silva, Luís Meneses, Jon Hillesheim and Costanza Maggi. This work has been carried out within the framework of the EUROfusion Consortium and has received funding from the Euratom research and training programme 2014-2018 under grant agreement No 633053. IST activities also received financial support from 'Fundação para a Ciência e Tecnologia' through project UID/FIS/50010/2013. The views and opinions expressed herein do not necessarily reflect those of the European Commission.

REFERENCES

Diallo, A., Groebner, R. J., Rhodes, T. L., Battaglia, D. J., Smith, D. R., Osborne, T. H., Canik, J. M., Guttenfelder, W. & Snyder, P. B. 2015*a* Correlations between quasi-coherent fluctuations and the pedestal evolution during the inter-edge localized modes phase on DIII-Da). *Physics of Plasmas* **22** (5), 056111.

Diallo, A., Hughes, J.W., Baek, S-G., LaBombard, B., Terry, J., Cziegler, I., Hubbard, A., Davis, E., Walk, J., Delgado-Aparicio, L., Reinke, M.L., Theiler, C., Churchill, R.M., Edlund, E.M., Canik, J., Snyder, P., Greenwald, M. & White, A. 2015*b* Quasi-coherent fluctuations limiting the pedestal growth on Alcator C-Mod: experiment and modelling. *Nuclear Fusion* **55** (5), 053003.

Dickinson, D, Roach, C M, Saarelma, S, Scannell, R, Kirk, A & Wilson, H R 2012 Kinetic instabilities that limit β in the edge of a tokamak plasma: a picture of an H-mode pedestal. *Physical review letters* **108** (13), 135002, arXiv: 1110.0619.

Groebner, R.J., Chang, C.S., Hughes, J.W., Maingi, R., Snyder, P.B., Xu, X.Q., Boedo, J.A., Boyle, D.P., Callen, J.D., Canik, J.M., Cziegler, I., Davis, E.M., Diallo, A., Diamond, P.H., Elder, J.D., Eldon, D.P., Ernst, D.R., Fulton, D.P., Landreman, M., Leonard, A.W., Lore, J.D., Osborne, T.H., Pankin, A.Y., Parker, S.E., Rhodes, T.L., Smith, S.P., Sontag, A.C., Stacey, W.M., Walk, J., Wan, W., Wang, E.H.-J., Watkins, J.G., White, A.E., Whyte, D.G., Yan, Z., Belli, E.a., Bray, B.D., Candy, J., Churchill, R.M., Deterly, T.M., Doyle, E.J., Fenstermacher, M.E., Ferraro, N.M., Hubbard, A.E., Joseph, I., Kinsey, J.E., LaBombard, B., Lasnier, C.J., Lin, Z., Lipschultz, B.L., Liu, C., Ma, Y., McKee, G.R., Ponce, D.M., Rost, J.C., Schmitz, L., Staebler, G.M., Sugiyama, L.E., Terry, J.L., Umansky, M.V., Waltz, R.E., Wolfe, S.M., Zeng, L. & Zweben, S.J. 2013 Improved understanding of physics processes in pedestal structure, leading to improved predictive capability for ITER. *Nuclear Fusion* **53** (9), 093024.

Groebner, R.J., Snyder, P.B., Osborne, T.H., Leonard, A.W., Rhodes, T.L., Zeng, L, Unterberg, E.A., Yan, Z, McKee, G.R., Lasnier, C.J., Boedo, J.A. & Watkins, J.G. 2010 Limits to the H-mode pedestal pressure gradient in DIII-D. *Nuclear Fusion* **50** (6), 064002.

Kinsey, J. E., Bateman, G., Onjun, T., Kritz, A. H., Pankin, A., Staebler, G. M. & Waltz, R. E. 2003 Burning plasma projections using drift-wave transport models and scalings for the H-mode pedestal. *Nuclear Fusion* **43** (12), 1845–1854.

Leonard, A. W. 2014 Edge-localized-modes in tokamaks. *Physics of Plasmas* **21** (9), 090501.

Snyder, P.B., Groebner, R.J., Hughes, J.W., Osborne, T.H., Beurskens, M., Leonard, A.W., Wilson, H.R. & Xu, X.Q. 2011 A first-principles predictive model of the pedestal height and width: development, testing and ITER optimization with the EPED model. *Nuclear Fusion* **51** (10), 103016.

Snyder, P. B., Wilson, H. R., Ferron, J. R., Lao, L. L., Leonard, A. W., Osborne, T. H., Turnbull, A. D., Mossessian, D., Murakami, M. & Xu, X. Q. 2002 Edge localized modes and the pedestal: A model based on coupled peeling-ballooning modes. In *Physics of Plasmas*, , vol. 9, pp. 2037–2043.

Urano, Hajime 2014 Pedestal structure in H-mode plasmas. *Nuclear Fusion* **54** (11), 116001.

Wagner, F 2007 A quarter-century of H-mode studies. *Plasma Physics and Controlled Fusion* **49** (12B), B1–B33.

Complete characterization of L2I laser system ultra short pulse

Mario Galletti

Instituto de Plasmas e Fusão Nuclear (IPFN), Instituto Superior Técnico, Avenida Rovisco Pais, 1049-001 Lisboa, Portugal

e-mail: mario.gall22@gmail.com

Abstract. The complete characterization of an ultra short intense laser was performed. The Laboratory of Intense Lasers (L2I), at Istituto Superior Técnico in Lisbon, hosts a Chirped Pulse Amplification (CPA) laser system that delivers 1ps pulses at 1032nm wavelength with an energy of 50mJ and 1Hz repetition rate. The temporal pulse characterization was performed using a Scanning Auto-Correlation (AC) diagnostic tool. Moreover, the complete pulse characterization was retrieved using a 1-D conjugate gradient minimization algorithm able to analyse the traces of a scanning Second Harmonic Generation (SHG) Frequency Resolved Optical Gating (FROG) diagnostic tool. The complete characterization was performed for different parameters of the compression stage (pulse incident angle, Θ and gratings distance, L) and the shortest pulse achivable (around 600 fs) was obtaind for an angle within $[294, 294.5]$ deg and a L around 64 cm.

Short bio. Mario has a Master Degree in Physics from the University of Pisa. He is passionate about laser science, laser-plasma interaction, laser-matter interaction, ultrafast optics, ultrafast and high-power laser science, and nonlinear optics.
He has lived in different European cities for his studies. In his free time, Mario enjoys travelling, playing musical instruments (specially the guitar), playing football, watching movies, working with computers and reading books.

1. Introduction

The characterization of the ultra short laser pulses is essential for studying many physical process, among which: photo-dissociation that is more efficient in the case of using chirped pulses; non-linear phenomena such as self-focusing, self-phase modulation and others which modify the laser beam. Moreover, the characterization of this type of pulses is useful to test theoretical models about laser physics and to succeed in the successive possible production of even shorter pulses. Our major interest in the characterization of ultra short laser pulses is the evaluation of the temporal pulse shape (presence of a pedestal, pre pulses, etc.) for the employment of this type of pulses in plasma physics experiments about laser-plasma interaction (M. Litos 2014), inertial fusion (H.-S. Park 2014) and so on. Though it is essential in many research topics, the characterization of the ultra short laser pulses has always been a challenge. The measurements require the use of completly optical diagnostic tool because electronic ones are not sufficiently fast. The tools also require using the same pulse to measure itself, because it does not exist a shorter event to compare to. There are many other difficulties to take into account, concerning the pulse itself (non-linear effects, distortion, etc.) and the complexity of the setup required to perform the measurements. In this report we present measurements relative to the pulse duration performed with an AC diagnostic tool (Trebino 2012). Measurements relative to the pulse intensity, shape and phase both in temporal and spectral domain were performed with the SHG FROG diagnostic tool (P. OShea & Trebino 2001; R. Trebino 1997; Trebino 2012; Kane & Trebino 1993; D.J. Kane & DeLong 1994), that works simultaneously in both domains. Moreover, regarding the spectral phase, we determined the non-linear coefficient (Trebino 2012; Rulliere 1998) to estimate some distortions undergone by the pulse. The analysis of the FROG traces was performed with a non-commercial single shot algorithm, based on the 1-D conjugate gradient minimization method, instead of other commercial algorithms (R. Trebino 1997) like the Basic Frog algorithm (DeLong & Trebino 1994; Kane & Trebino 1993; D.J. Kane & DeLong 1994), General Projection algorithm (K.W. DeLong & Wilson 1994; R. Trebino 1997), Composite algorithm (DeLong & Trebino 1994; K.W. DeLong & Wilson 1994) because of: problem of convergence, velocity of convergence and high flux of data needed.

2. Laser Diagnostic

2.1. *Scanning Auto-Correlation*

In the temporal domain, one of the most used diagnostic tools is the scanning AC (Kintzer & Rempel 1987; Sala & Hall 1980; Trebino 2012); it is based on the comparison of the pulse with itself. In figure 1a a general AC setup is shown and in figure 1b a schematic representation of the optical path of the pulses in the AC setup used is presented. The input pulse (red) is split into two copies with a Beam Splitter (BS): one part goes through a fixed path length (orange) and the other is periodically delayed, with a 0.1 ps, step by a mechanical shaker (salmon); at the end, both are focused and overlapped, thanks to a lens inside a Second Harmonic Generation (SHG) crystal. In the non-linear medium, a SHG radiation (green), with the frequency doubled respect to the initial one, is produced and it is sent to a photo-multiplier. The intensity of the AC signal varies as a function of the delay τ between the two copies: $I_{SHG} \propto I(t)I(t-\tau)$. Since detectors, even streak cameras, are too slow to time-resolve I_{SHG}, this measurement produces the time integral

$$A^2(\tau) = \int I(t)I(t-\tau)dt \tag{2.1}$$

called Auto-Correlation intensity. The $A^2(\tau)$ signal presents some peculiarities like temporal symmetry respect to τ and the maximum of the signal is reached for the condition $\tau = 0$. The only information that we can retrieve from this measurement is the pulse duration, in fact when there is no more temporal overlapping between the two pulse copies the SH emission disappears. The AC trace does not produce accurate information about the structure of the pulse and it gives no information about the temporal phase.

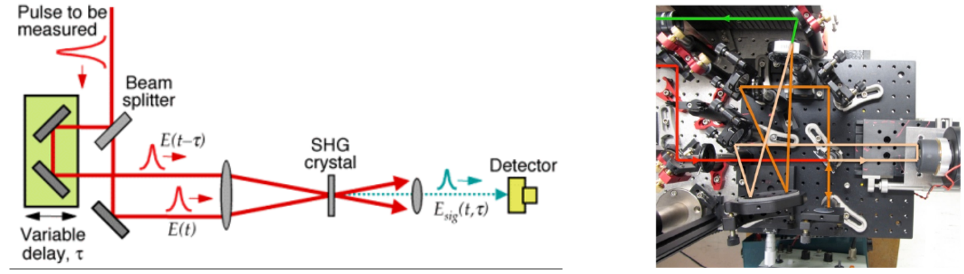

(a) General Scanning Auto-Correlation setup

(b) Scanning AC diagnostic tool installed in our setup

FIGURE 1. Scanning AC diagnostic tool

2.2. *SHG Frequency Resolved Optical Gating*

FROG (Kane & Trebino 1993; D.J. Kane & DeLong 1994; R. Trebino 1997; Trebino 2012) is a technique that operates simultaneously in the temporal and spectral domain. SHG FROG is a spectrally resolved Auto-Correlation. Mathematically this is translated with the signal $E_{SHG} = E(t)E(t-\tau)$, as the integrand in equation 2.1, that is Fourier transformed to obtain the AC signal spectrally resolved. It has the same setup of the AC (figure 1) but at the end of the optical path the signal is received by a spectrometer (R. Trebino 1997), like in figure 2a, instead of a detector (photo-multiplier, etc.).

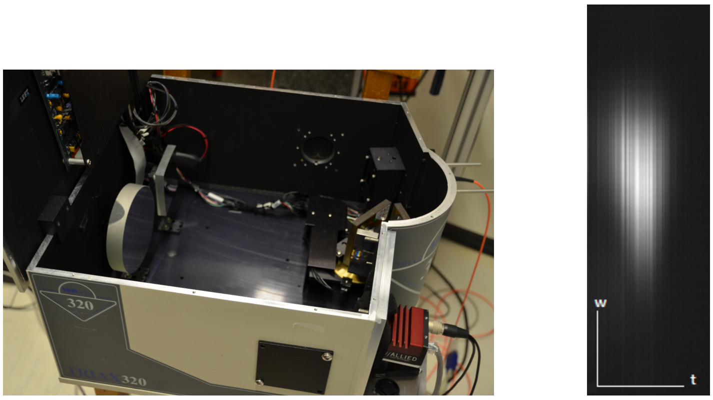

(a) Spectrometer diagnostic tool installed in our setup

(b) FROG trace retrieved

FIGURE 2. FROG diagnostic tool setup and trace.

In our setup the AC signal is coupled in a fiber (orange cable in figure 2a) that permits the signal to propagate to the spectrometer to estimate its spectrum. The setup consists mainly in a diffraction grating that splits the incident light into several beams with different λ. The diffracted beams are imaged onto a detector, a CCD camera in our case, for the analysis. By saving the AC signal spectrum in an array and doing this procedure for different delays between the two pulse copies, we are able to build a matrix $M(\tau, \omega)$ that is our SHG FROG trace, like in figure 2b. FROG is able to provide us all the information, both temporal and spectral about the pulse (Baltuska 1999), necessary for a complete characterization.

2.2.1. *FROG Pulse Retrieval Algorithm*

This innovative laser pulse algorithm (M.Galletti 2016) for the diagnostics is based on the 1-D conjugate gradient minimization method. It consists in the acquisition of an experimental image $M(\tau, \omega)$, which is subtracted from the background, centered in the maximum of the intensity and re-scaled to have the needed dimensions before being used and reconstructed by the program, $I(\tau, \omega)$; succesively the image will be compared to the calculated analytic image produced, $S(\tau, \omega)$, starting from an arbitrary reasonable pulse $E(t)$, thanks to the SHG FROG formula:

$$I_{FROG}^{SHG} = \left| \int E(t)E(t-\tau)e^{-i\omega t}dt \right|^2 \tag{2.2}$$

In the second stage, by using an iterative loop, the algorithm varies at each step the arbitrary pulse minimizing the differences between the two images, finally succeeding to obtain a reconstructed pulse as similar as possible to the real one.
This second part, consisting of the iterative loop, is made up by two main parts:

- calculation of: the SHG FROG signal (equation 2.2); the modified distance χ^2 (equation 2.3), consisting in the real distance between the experimental and the calculated image plus a term added to maintain the temporal barycenter in the middle of the trace so to permit a better reconstruction of the experimental SHG FROG trace

$$\begin{aligned} \chi^2 = \int \int \left| I(\tau,\omega) - S(\tau,\omega) \right|^2 d\tau d\omega + \\ \eta \left(\int t|E(t)|^2 dt - N/2 \int |E(t)|^2 dt \right)^2 \end{aligned} \tag{2.3}$$

with $\eta = \alpha \frac{\bar{\chi}^2}{\sum_j |Ej|^2|_{in}}$ (weighting function), $\alpha < 1$ a variable coefficient and NxN image dimensions (pixel number); the gradient of the χ^2 with respect to $E(t)$; the minimum of the χ^2 function in the gradient direction.

- updating of the new field with the minimum position (according to Conjugate Gradient method).

The process is repeated until it reaches a set value of the χ^2 "modified distance" or a field variation or a χ^2 variation of the order of 10^{-3} for which the reconstructed laser pulse field does not vary significantly anymore.

3. Experimental Setup

The laser setup used was the one described in the references (C. P. Joao & Figueira 2014; Hariton 2016) with the addition of the AC and FROG diagnostics after the compression stage. The pulses available at the compressor exit had a wavelength of 1032nm, a duration of 1ps, an energy of 50mJ (due to the compressor losses) at 1Hz repetition rate. The AC and FROG measurements were not performed at full energy but just with 25mJ of energy, around half the energy available after the compression stage. Obviously, to avoid damages in the diagnostic optics (e.g. SHG crystal damage threshold is around tens GW/cm^2), the energy sent to the diagnostic was not 25 mJ so we took a mirror leak (about 0.7% of the original pulse) before the compressor for the characterization. After the leak compression, the measurements was performed guiding the pulse through an optical path into the two different diagnostic tools.

4. Data Analysis: Temporal and Spectral Characterization

4.1. *Scanning AC*

The pulse at the exit of the compressor was measured. Using a spectrometer, we measured the spectrum (Rulliere 1998; Trebino 2012) of the pulse, in figure 3a. We retrieved from the spectrum the transform-limited pulse, figure 3b, that is usually understood as the lower limit for the pulse duration which is possible for a given optical spectrum of a pulse.

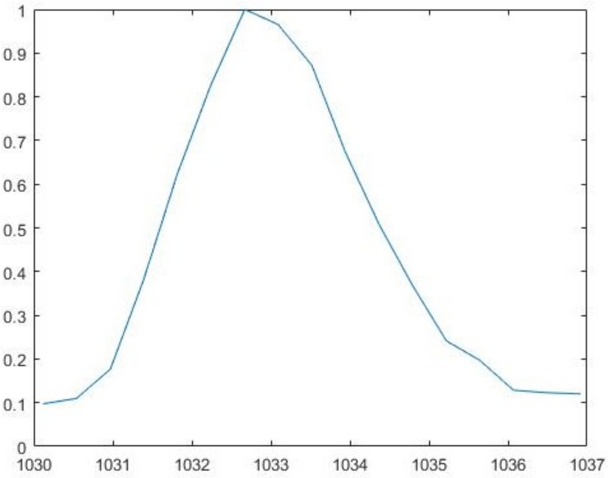

(a) Pulse spectrum I(A.U.) vs λ (nm)

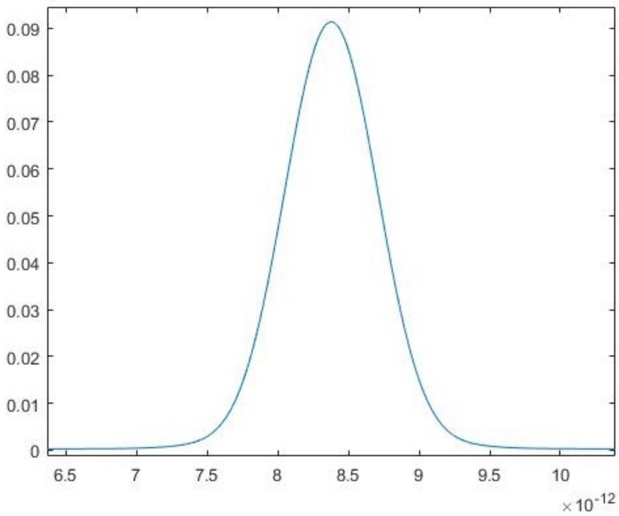

(b) Transform limited pulse I(A.U.) vs t(s)

FIGURE 3. Spectrum measurement.

The 2.8nm spectral bandwidth can support a 564 fs pulse that is translated into 773fs AC FWHM. The experimental data taken from the photo-multiplier are plotted in figure

4, AC intensity vs Time Delay. The temporal width of the compressed pulse can be retrieved thanks to the formula

$$\Delta t^{AC}_{FWHM} = \sqrt{2}\Delta t^{PULSE}_{FWHM} \tag{4.1}$$

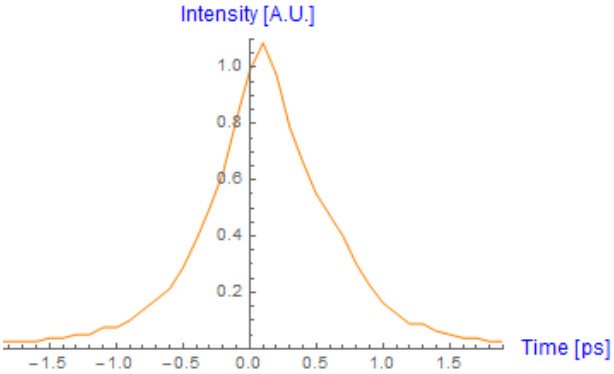

FIGURE 4. Scanning AC Intensity vs Time

From the data we found $\Delta t^{AC}_{FWHM} = 0.882$ ps and by using the equation 4.1 we retrieved 624 fs pulse length.

4.2. *SHG FROG*

4.2.1. *Pulse Retrieval Algorithm Results*

The compressor has two degrees of freedom: the pulse incident angle on the compressor grating and the distance between the gratings. The three SHG FROG experimental traces depend on these two parameters of the compressor (Rulliere 1998). We managed to completly characterize these three different pulses with different conditions on the compressor, in order to understand which is the best angle and distance to reach better pulse compression. The initial values for L and Θ were the one setted in the experimental setup. Successively, we modified Θ with steps of 0.5deg and subsequently finding an L that was roughly maximizing the intensity of the AC signal for that Θ. In figure 5,6 and 7 we report the complete characterization of the pulse for the three different angles Θ and length L. The error of these retrieved measurements is given by the value of the distance χ^2 (Section 2.2.1, equation 2.3) that is less than 1, this means that the measures are really accurate. We crosschecked these results retrieving the marginals from the FROG experimental trace that provided us the spectral SHG signal width and the AC signal width and also using a commercial algorithm provided from the FROG diagnostic company. All the results are in a really good agreement.

Moreover, we analyzed in particular the spectral phases (Rulliere 1998; Trebino 2012), in figure 5(b), 6(b), 7(b), deducing its coefficients to understand the distortions to which the pulse is subjected to. Fitting the spectral phase data with:

$$\phi(\omega) = \phi_0 + \phi_1\omega + \frac{1}{2}\phi_2\omega^2 + \frac{1}{3}\phi_3\omega^3 + ... \tag{4.2}$$

we retrieved: ϕ_2 which is the second order dispersion, the Group Delay Dispersion (GDD) and represents a symmetric distortion of the signal. It is interpreted as a temporal stretch of the pulse if the GDD value is positive or as a temporal compression if the value is negative; ϕ_3 which is the third order dispersion (TOD). It introduces pre or post pulses to the signal. In table 1 all the parameters are resumed.

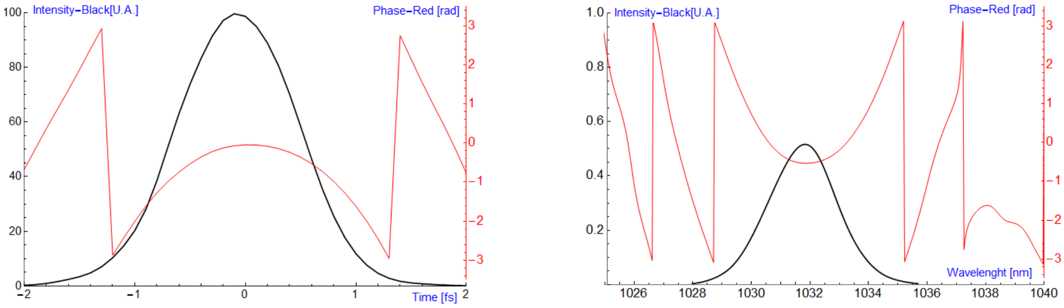

(a) Temporal intensity and phase at $\Theta = 293.5$ *deg.*

(b) Spectral intensity and phase at $\Theta = 293.5$ *deg.*

FIGURE 5. Complete characterization at $\Theta = 293.5$ *deg.*

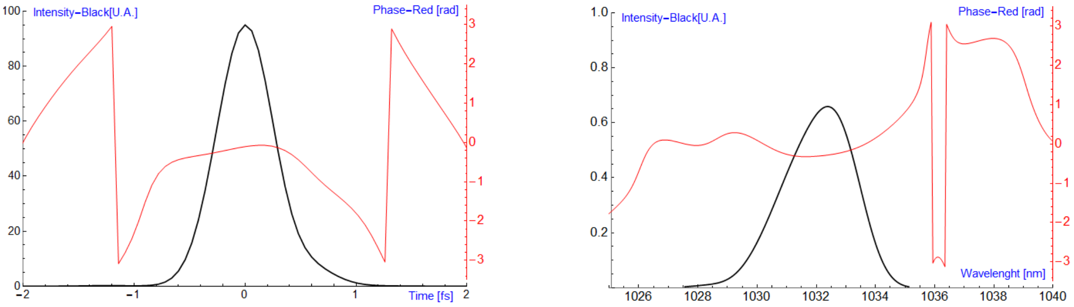

(a) Temporal intensity and phase at $\Theta = 294$ *deg.*

(b) Spectral intensity and phase at $\Theta = 294$ *deg.*

FIGURE 6. Complete characterization at $\Theta = 294$ *deg.*

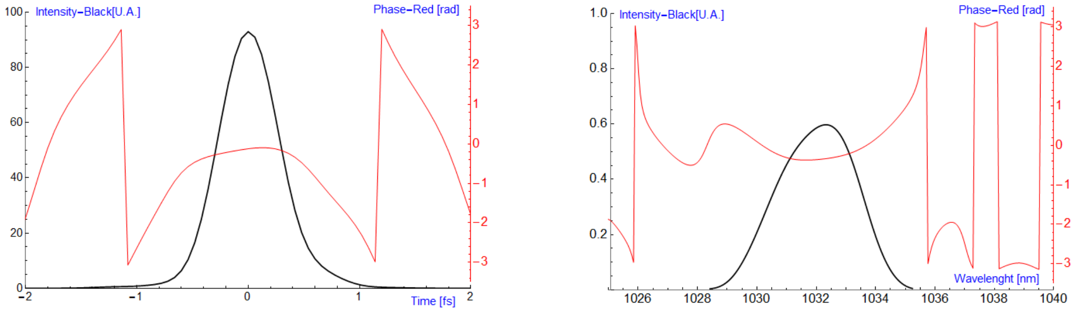

(a) Temporal intensity and phase at $\Theta = 294.5$ *deg.*

(b) Spectral intensity and phase at $\Theta = 294.5$ *deg.*

FIGURE 7. Complete characterization at $\Theta = 294.5$ *deg.*

5. Conclusion

We notice from the FROG trace retrieved parameters that we reach the best pulse compression for an angle within $[294, 294.5]$ deg and a L around 64 cm. The GDD is bigger for the pulse at the 294.5 deg angle respect to the 294 deg angle, but on the contrary the TOD is almost zero for the 294.5 deg angle. Within this interval we can find an angle that minimizes in the best way both distortions to which the pulses are subjected to. In the near future the analysis will be extended to other sets of data taken at full power whilst implementing some modifications to the algorithm. These modifications consist in the implementation of functions analysing information derived by other diagnostic tools (like SPIDER (C. Iaconis 1998), Spectrum (Rulliere 1998; Trebino 2012), Autocorrelation (Rulliere 1998; Trebino 2012)), to obtain more precise pulse characterization.

Θ (deg)	L (cm)	ΔT (fs)	ΔS (nm)	$\phi_3(fs^3)$	$\phi_2(fs^2)$
293.5	60	1250	2.75	0.34	105.25
294	64	614.7	2.8	0.89	29.86
294.5	64	633.5	3.1	0.06	35.73

Table 1. Parameters of the three retrieved pulses for different compression angles.

REFERENCES

Baltuska, A; Pshenichnikov, MS; Wiersma DA 1999 Second-harmonic generation frequency-resolved optical gating in the single-cycle regime. *IEEE J Q EL* **35(4)**, 459–478.

C. Iaconis, I.A. Walmsley 1998 Spectral phase interferometry for direct electric-field reconstruction of ultrashort optical pulses. *Opt. Lett.* **23**, 792.

C. P. Joao, H. Pires, L. Cardoso T. Imran & Figueira, G. 2014 Dispersion compensation by two-stage stretching in a sub-400 fs, 1.2 mj yb:caf2 amplifier. *OPTICS EXPRESS* **22(9)**.

DeLong, K.W. & Trebino, R. 1994 Improved ultrashort pulse-retrieval algorithm for frequency-resolved optical gating. *J. Opt. Soc. Am. A* **11**, 2429.

D.J. Kane, A.J. Taylor, R. Trebino & DeLong, K.W. 1994 Single-shot measurement of the intensity and phase of a femtosecond uv laser pulse with frequency-resolved optical gating. *Opt. Lett* **19**, 1061.

H.-S. Park, O.A. Hurricane, D.A. Callahan D.T. Casey E.L. Dewald T.R. Dittrich T. Dppner D.E. Hinkel L.F. Berzak Hopkins S. Le Pape T. Ma P.K. Patel B.A. Remington H.F. Robey J.D. Salmonson J.L. Kline. 2014 *Physical Review Letters* **112**, 055001.

Hariton, V. 2016 Feasibility study and simulation of a high energy diode-pumped solid-state amplifier.

Kane, D.J. & Trebino, R. 1993 Single-shot measurement of the intensity and phase of an arbitrary ultrashort pulse by using frequency-resolved optical gating. *Opt. Lett.* **18**, 823.

Kintzer, E.S. & Rempel, C. 1987 Near-surface second-harmonic generation for autocorrelation measurements in the uv. *Applied Physics B* **42**, 91–95.

K.W. DeLong, D.N. Fittinghoff, R. Trebino B. Kohler & Wilson, K. 1994 Pulse retrieval in frequency-resolved optical gating based on the method of generalized projections. *Opt. Lett.* **19**, 2152.

M. Litos, et al. 2014 http://dx.doi.org/10.1038/nature13882. *Nature* **515**, 95.

M.Galletti, M.Galimberti, D.Giulietti A.Curcio 2016 Ultra short pulse reconstruction software: Grog. *Journal of Instrumentation* **11**, C07011.

P. OShea, M. Kimmel, X. Gu & Trebino, R. 2001 Highly simplified device for ultrashort-pulse measurement. *Opt. Lett.* **26**, 932.

R. Trebino, K.W. DeLong, D.N. Fittinghoff J.N. Sweetser M.A. Krumbugel et al. 1997 Measuring ultrashort laser pulses in the time-frequency domain using frequency-resolved optical gating. *Rev. Sci. Instrum.* **68**, 3277.

Rulliere, C. 1998 *Femtosecond Laser Pulses: Principles and Experiments*.

Sala, K.L., G.A. Kenney-Wallace & Hall, G.E. 1980 Cw autocorrelation measurements of picosecond laser pulses. *IEEE Journal of Quantum Electronics* **16(9)**, 990–996.

Trebino, R. 2012 *Frequency Resolved Optical Gating: The Measurement of Ultra-shortLaser Pulses*.

A review of the MARTe control framework

Pedro Deus Lourenço

Instituto de Plasmas e Fusão Nuclear (IPFN), Instituto Superior Técnico, Avenida Rovisco Pais,
1049-001 Lisboa, Portugal

e-mail: plourenco@ipfn.tecnico.ulisboa.pt

Abstract. The Multi-threaded Application Real-Time executor (MARTe) is a software framework oriented towards the design, testing and deployment of real-time control applications. It supplies a complete set of tools and ready to use code modules that expedite system commissioning. The framework was employed with success on several known machines of the controlled nuclear fusion community and proved itself as a reliable and powerful solution for critical systems. This review provides a comprehensive analysis over the framework structure and development followed by two specific applications. Finally, the implementation footprint and integration with the Discharge Control System (DCS) and the Experimental Physics and Industrial Control System (EPICS) frameworks is also addressed.

Short bio. Pedro obtained his MSc Degree in Physics Engineering in 2015 from IST.

During the master thesis and afterwards he worked at IPFN as a research fellow, where he developed a control and data acquisition system for a beam-plasma interaction device. Besides gaining experience in these fields, he developed a special interest in radiofrequency-based diagnostics and wave propagation inside plasmas. It became clear that these fields would therefore shape his future research career.

Pedro was an active member of the Physics Students Board (NFIST) since 2010, first as Treasurer in the same year and later as member of the Fiscal and Disciplinary Board in 2013.

1. Introduction

In real-rime control systems (RTCS) it is essential that critical tasks are performed within time intervals which must fall below the characteristic time of the processes under control. With the increasing complexity of physical systems requiring control, it becomes necessary to find new technological solutions in order to address multiple complex task in very short time intervals. A case of interest can be found in the Controlled Nuclear Fusion community. Large and complex endeavours such as the Joint European Torus (JET) present a direct connection over the past decades to the development of new approaches and paradigms on this technological field. Achieving performance optimization at the expense of specific tailored hardware and operating systems carries with it a closed and frequently proprietary development environment. Also, the more specific the control system becomes, the more difficult it is to include or upgrade new features. These impairments raised the need for frameworks that are not committed to a particular problem or experiment but instead, empower system designers with code modularity and portability between applications. Since different operating systems and hardware are frequently used, such framework must rely on a multi-platform compliant code library which allows to implement software layer abstraction and transparency while keeping hard real-time performance. This was achieved with the Multi-threaded Application Real-Time executor (MARTe).

1.1. *JETRT*

MARTe is a development from the previous real-time framework called JETRT. It is built upon the same principles of portability between platforms and to provide effective tools for system design and commissioning (G. De Tommasi & Contributors (2005)). Different RTCSs were implemented and tested on JET (Krom (1999); G. De Tommasi & Contributors (2005)) over its operational life during which several constrains were noticed, e.g., hardware and software applications were not separated, making it hard and time consuming to upgrade system components. Therefore, migrating to a new platform implied an almost complete re-writing of the code (G. De Tommasi & Contributors (2005)).

The JETRT was a framework based upon a cross-platform class-library created to optimize the development of real-time systems (G. De Tommasi & Contributors (2005)). It was designed upon two major ideas: to use as much components on the shelf as possible and ensure enough processing power to meet the timing constrains (G. De Tommasi & Contributors (2005)). Employing this solution meant that the majority of time spent on a certain system could be allocated to algorithm testing since the framework already provided a real-time optimization structure by itself. This was achieved by separating the algorithms from the interfaces (G. De Tommasi & Contributors (2005)) which enable the possibility to test and correct the system before introducing it into the actual machine environment. Using stored signals from live machine operation as an input to the algorithms and running the framework on a test environment was a clear advantage over conducting all tests online (G. De Tommasi & Contributors (2005)).

As a framework, the JETRT application (JETRTApp) provided major components as the supervisor state-machine, real-time thread, external boards interface, communication treads and a real-time collectors system (G. De Tommasi & Contributors (2005)). Also, a timing module was available in order to synchronize the tasks on the framework. The external time triggering service object managed the external timing triggering synchronization hardware while the internal CPU timing service object provided the high-resolution information (G. De Tommasi & Contributors (2005)). Different clock sources could be employed, such as the CPU internal counting register or any external hardware timer line. This multiple clock source feature is possible since the drivers can either provide timing services, data source or data sink (G. De Tommasi & Contributors (2005)). Finally, the internal debugger based on the command line C/C++ interpreter (CINT) enabled to query the system about the internal value or status of a variable in both JETRTApp and the User Application. The debugger allows for the application to be aware of its own data structures, thus making it simple to interact with the program (G. De Tommasi & Contributors (2005)).

2. MARTe Framework

MARTe was designed using C++, a wide spread object oriented language. This constitutes an excellent paradigm for application development, enforcing modularity, data abstraction and inheritance. As a direct outcome, the amount of reusable units of code is maximized (A. Neto & Contributors (2009)). Furthermore, a special real-time C++ library called BaseLib2 (Barbalace (2009)) was built to ensure that the same code could run over different operating systems. The library is divided into seven hierarchic dependent levels labelled from 0 to 6 (Barbalace (2009)). OS and hardware dependent operations lay on level 0 while application level operations such as GAMs and state machine run on level 5. This way, the developed application does not rely on OS dependent calls (A. Neto & Contributors (2009)). Today, the BaseLib2 has been already ported to VxWorks, Linux, Linux/RTAI, Solaris, OS X and MS Windows, following the rules present in the Portable Operating System Interface (POSIX) standards for real-time application interfaces (A. Neto & Contributors (2009)).

2.1. *Interfaces and Tools*

Knowledge about the target OS is not required when developing applications using MARTe due to data streaming and I/O operation classes, present on the library (A. Neto & Contributors (2009)). Moreover, the standard protocol used to query objects is Hypertext Transfer Protocol (HTTP) which is directly provided on library as a multi-threaded server. This allows to build a database containing the tree of application objects connected via their own HTTP interface, making it easy to map and browse through the system (A. Neto & Contributors (2009)). The resulting network also enables the exchange of messages between objects synchronously or asynchronously. The HTTP server may be accessed form a web browser (I. Carvalho & Contributors (2014)), providing information about the configuration and the current state of the system and allowing to change system configuration. HyperText Markup Language (HTML) may also be used to develop practical human-machine interface (HMI) (I. Carvalho & Contributors (2014)).

The logger is a fundamental tool to monitor the behaviour of the application under operation. It consists on a Java based application with a graphical interface that is capable of handling messages issued by one or more machines. Messages can be organized according to the level of priority, issuing object or running thread (A. Neto & Contributors (2009)). These may also be stored into persistent memory files for posterior analysis. BaseLib2 includes a series of logging functions that can be embedded into the code modules. These can be used to flag that a certain value was received or that a required task was accomplished. Apart from the message itself, it is also possible to append other relevant information such as time stamp, thread, module name and location in memory (A. Neto & Contributors (2009)). Since these messages are intended for the logger and not for other real-time code modules, they are not constrained by real-time demands. Furthermore, issuing and transfer these messages must carry a minimum impact on the system since the logger must not comprise the real-time performance under any circumstances (A. Neto & Contributors (2009)). To accomplish this feature, sent messages are stored on a first-in-first-out (FIFO) buffer and managed by a low priority consumer. These are only broadcasted to the logger application when there is available processor time. By default configuration, messages are sent using User Datagram Protocol (UDP) to a specific external or internal address (A. Neto & Contributors (2009)).

2.2. *Components*

The MARTe framework is constituted by a complete set of modules that allow to develop and deploy a RTCS where the fundamental element is a block of code which implements an interface specified on the library (A. Neto & Contributors (2009); Barbalace (2009)), the Generic Application Module (GAM). Any application developed on MARTe will have GAMs as core units as they are unrestricted in terms of functionality (A. Neto & Contributors (2009)). These fundamental code units have one mandatory entry point for configuration. However, only one data input and one data output points can also be present, imposing clear boundaries into the system. GAMs are versatile modules as they can be used for executing algorithms, store data or interface with hardware, among other features. A specific type of GAMs, the IOGAM, is also present to provide high-level interface with the hardware drivers that communicate with the hardware itself. Such high-level communication is based (A. Neto & Contributors (2009)) on the generic module acquisition class(Barbalace (2009)), which may be configured to return the last acquired value or to wait for the arrival of a new sample. The transfer of data between GAMs is performed using an optimized memory bus called Dynamic Data Buffer (DDB). It monitors the coherence of the exchanged data and alerts for the occurrence of errors and competing writing situations (A. Neto & Contributors (2009)).

Each MARTe application must contain at least one real-time thread. These threads contain a group of GAMs and operate as a sequential execution scheduler (A. Neto & Contributors (2009)), enabling to configure the execution sequence and frequency. Alongside, it also keeps track of the time spent on the execution of each GAM and reports an error (Barbalace (2009); A. Neto & Contributors (2009)) when the total time overlaps the cycle time defined by the designer. Accessing these individual time registers is also possible in order to retrieve information on the execution time of each module (Barbalace (2009)). The synchronization of threads requires a timing source which may be provided by external hardware or by the CPU clock itself. Although generic modules are available, MARTe already supplies a series of timing emulation modules for project development stages which are optimized for different operating systems (A. Neto & Contributors (2009)).

3. The JET Application

The first target application for MARTe was the plasma Vertical Stabilization system (JET VS) in JET (A. Neto & Contributors (2008)). There, it is required that the shape of the plasma is elongated to enhance fusion performance. However, this shape makes the plasma column unstable (A. Neto & Contributors (2009)) and to compensate it, the system must drive the poloidal field coils to create a stabilizing radial magnetic field. In practice, this control action must be done in closed-loop within a cycle time of 50μs and with a maximum jitter of 2.5μs (A. Neto & Contributors (2009, 2008)). This was achieved using Field Programmable Gate Array (FPGA) based Advanced Telecommunication Computing Architecture (ATCA) boards with multiple-input-multiple-output (MIMO) architecture which was able to achieve a control-cycle time around 30μs by employing a Intel Quad-Core x86 processor. Also, the MARTe framework was installed on Linux OS with Real-Time Application Interface (RTAILinux) module and using PCI Express fabric (A. Batista & Contributors (2009)). This combination of software and Quad-Core hardware enabled to isolate the cores so that interrupts and OS treads are allocated to one core exclusively, leaving the remaining three for MARTe threads. One of those cores runs the high priority real-time thread, whereas the remaining two are used for less critical MARTe operations, as shown in figure 1.

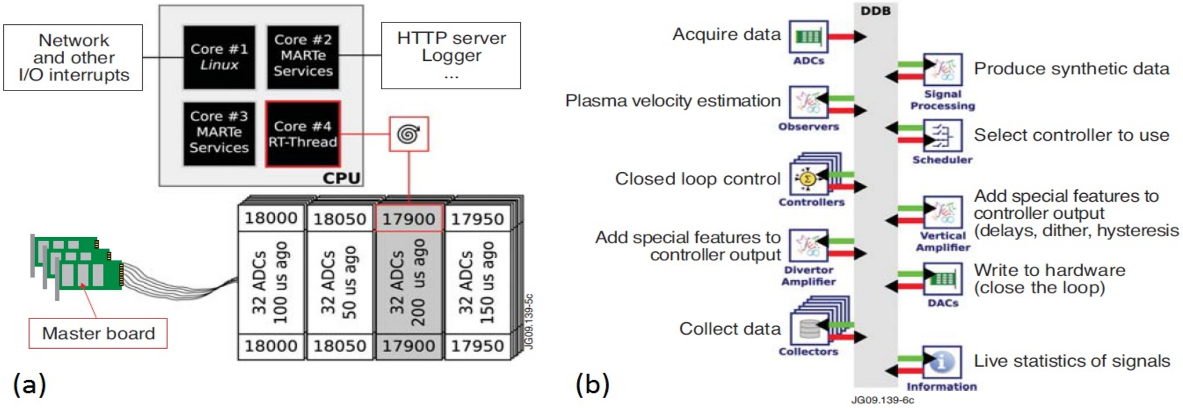

FIGURE 1. Schematics of the JET VS system based on the MARTe framework. It can be observed (*a*) how different threads are allocated on the four CPU cores so that real-time performance is not compromised by competing processes such as interrupts from the Linux core system. Alongside, on (*b*), is displayed the detailed sequence of GAMs that are executed within each control cycle (50μs) by the real-time thread. Figures taken from A. Neto & Contributors (2009).

For the final JET VS application, the control cycle was tuned to the initial 50μs exhibiting a measured jitter below 800ns (A. Batista & Contributors (2009)). Although the system is meant to work during discharges with a duration of approximately 2min, the decision was made (A. Neto & Contributors (2009, 2008)) to have the system constantly running in order to ensure high availability and real-time operation. These are critical requirements that will be essential in steady state operation machines like ITER. As a result, it was possible to run the system with no faults for consecutive weeks, during which several configuration changes were made by the machine operators (A. Neto & Contributors (2009)). This level of performance was a direct result from the uncommitted and transparent ways MARTe was designed (A. Neto & Contributors (2009)). Besides this application, the MARTe framework is also deployed in other JET systems such as the Error Field Correction Coils, Real-time Protection Sequencer and Plasma Wall Load System (A. Neto & Contributors (2011*a*)).

4. The ISTTOK Application

On ISTTOK the whole real-time control and data acquisition system (CODAS) was implemented using MARTe, running on an hardware system similar to the JET VS previously described (I. Carvalho & Contributors (2013)). It employs the same FPGA-ATAC boards and Core-Quad processor technology with tread isolation. The main objective was to extend the duration of the discharges by controlling the stability of the plasma. This also meant the operation reliability is increased. Several conducted tests showed that the real-time code uses approximately 50μs to run (I. Carvalho & Contributors (2013)). However, setting the closed loop cycle time exactly to this value becomes a major risk in case some unforeseen delay takes place. Therefore, the control cycle was set to 100μs with a jitter generally inferior to 0.4μs and with an

Device	Cycle time	System/sub-system	Operating system	Architecture
JET	50μs-10ms	Several sub-systems	Linux/RTAI/VxWorks	ATCA/VME/PC
COMPASS	50μs/500μs	Fast and slow PS	Linux	ATCA
FTU	250μs	Lower hybrid power	RTAI	VME
RFX	200-250μs	Magnetic control system	Linux(PreemptRT)	PXI
ISTTOK	100μs	Tokamak RT control	Linux	ATCA

Table 1. List of working systems using MARTe framework (I. Carvalho & Contributors (2013); A. Neto & Contributors (2011*b*)).

observed maximum of 6μs (I. Carvalho & Contributors (2013)). The framework also enabled the development of HTTP based HMI which simplified the configuration of discharges capable to handle complex events. Moreover, it can either be configured for time deterministic as well as event-driven operation. The implementation of the last paradigm was critical to extend the number of stable AC cycles (I. Carvalho & Contributors (2013)). Improvements on discharge stability can be observed on figure 2.

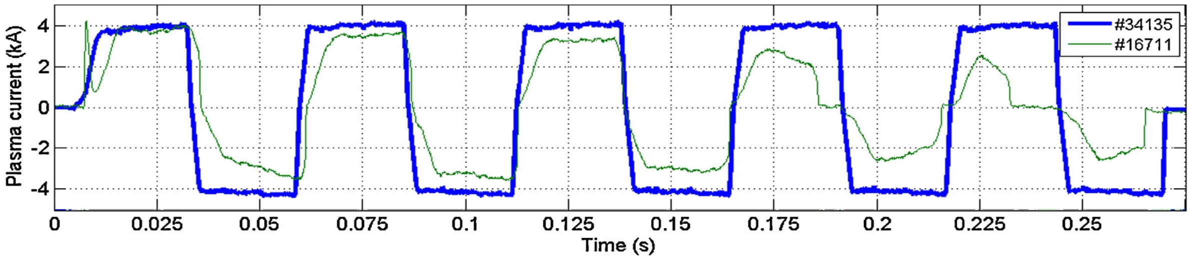

Figure 2. ISTTOK discharges before (#16711) and after (#34135) the real-time control system upgrade for the same pulse duration and plasma current. Figure adapted from I. Carvalho & Contributors (2013).

5. Present and Future Endeavours

Due to the unique features it presents, the MARTe has been employed along or together with other frameworks on the development of solutions for a number of devices (A. Neto & Contributors (2011*b*)). On table 1 is a comprised list of devices employing MARTe on their hard real-time control systems or subsystems. The framework is maintained by a strong community (A. Neto & Contributors (2008)) constituted by engineers and physicists that continue to develop new applications, enriching its scope by providing new drivers and support. A new version called MARTe2 is already under testing phase and is expected to be released in the beginning of next year.

The MARTe framework can also work together with other frameworks like the Discharge Control System (DCS). The DCS is a real-time framework based on C++, developed for ASDEX Upgrade (W. Treutterer & Contributors (2014)) which presents similar architecture to MARTe (C. Rapson & Contributors (2014)). Both employ modular code - GAMs in MARTe, Application Processes (APs) in DCS - in application design where the communication between modules is secured by passing signals. Also, it is not required to recompile the application code to change its configurations (C. Rapson & Contributors (2014)). Moreover, the frameworks distinguish between non-real-time and real-time operation employing a state machine. Unlike MARTe, where GAMs exchange signals in the primitive form of scalars and arrays, DCS APs include metadata along with the signals for security reasons(C. Rapson & Contributors (2014)). Comparatively, MARTe is easier to understand and to deploy application with than DCS. Although GAMs only communicate directly with other GAMs in the same thread, IOGAMs can be used to change data with hardware, different treads or other applications like the DCS. Interfacing with DCS is achieved through a shared memory mapping implementation between the two frameworks(C. Rapson & Contributors (2014)) while maintaining real-time performance. This achievement was critical for the future application the two frameworks on the ITER project. Finally, the Experimental Physics and Industrial Control System (EPICS) is a control framework which provides a set of tools to build distributed control systems that can also be integrated alongside with MARTe using memory sharing(S. Yun & Contributors (2014)).

6. Conclusions

MARTe is the result of a long road to answer the demanding control needs of nuclear fusion devices. The clear boundary between hardware interfacing, system configuration and algorithms makes MARTe a suitable multi-platform framework for designing and implementing real-time systems. It provides a powerful logger system and introspection tools that are essential either for debugging stages during application development or monitoring during operation itself. Code modularity and portability are only possible due to the introduced concept of GAM and to the fact that the framework lays over the C++ Baselib2 library. The same code can run on different architectures requiring only that the drivers to the hardware are developed. Moreover, separating real-time treads and other services allow for maximum advantage from multi-core technology. Successful implementation cases, where the target specifications of the application were met frequently using out-of-the-shelf (OOTS) hardware and open-source operating systems, constitute a strong indicator that the framework will keep up with the future technological challenges.

REFERENCES

A. Batista, A. Neto & Contributors, JET-EFDA 2009 Atca control system hardware for the plasma vertical stabilization in the jet tokamak. *2009 16th IEEE-NPSS Real Time Conference* .

A. Neto, D. Alves & Contributors 2011*a* Marte framework: A middleware for real-time application development. *Proceedings of ICALEPCS* .

A. Neto, D. Alves & Contributors, JET-EFDA 2011*b* A survey of recent marte based systems. *IEEE Transactions on Nuclear Science* **58** (4), 1122 1126.

A. Neto, F. Sartori & Contributors, JET-EFDA 2008 Linux real time framework for fusion devices. *EFDAJETCP(08)04/09* .

A. Neto, F. Sartori & Contributors, JET-EFDA 2009 Marte: a multi-platform real-time framework. *EFDAJETCP(09)01/02* .

Barbalace, A. 2009 Marte/baselib2 - software design analysis/code development guide. *Tech. Rep.*. PPCC-JET.

C. Rapson, P. Carvalho & Contributors 2014 Coupling dcs and marte: two real-time control frameworks incollaboration. *Fusion Engineering and Design* **89**, 31253130.

G. De Tommasi, F. Piccolo & Contributors, JET-EFDA 2005 Flexible software for real-time control in nuclear fusion experiments. *EFDAJETPR(05)12* .

I. Carvalho, P. Duarte & Contributors 2013 Isttok control system upgrade. *Fusion Engineering and Design* **88**, 1122 1126.

I. Carvalho, P. Duarte & Contributors 2014 Isttok real-time architecture. *Fusion Engineering and Design* **89**, 195203.

Krom, J. 1999 The evolution of control and data acquisition at jet. *Fusion Engineering and Design* **43**, 265273.

S. Yun, A. Neto & Contributors 2014 A shared memory based interface of marte with epics for real-time applications. *Fusion Engineering and Design* **89**, 614617.

W. Treutterer, R. Cole & Contributors 2014 Asdex upgrade discharge control systema real-time plasmacontrol framework. *Fusion Engineering and Design* **89**, 146154.

Carbon monoxide electron-neutral scattering cross sections

Polina Ogloblina

Instituto de Plasmas e Fusão Nuclear (IPFN), Instituto Superior Técnico, Avenida Rovisco Pais, 1049-001 Lisboa, Portugal

e-mail: polina.ogloblina@tecnico.ulisboa.pt

Abstract. This article is presenting the role of carbon monoxide (CO) molecule in atmosphere of Mars and Earth, showing the importance of its dissociation. Existing cross sections sets of electron collisions with carbon monoxide, proposed by Itikawa and Phelps, were compared. Swarm parameters were calculate, using two-therm Boltzmann solver, were compared with experimental data and corrections to the existing sets were proposed. The importance of rotational excitation cross sections is shown and they were added to the final set. It is described the inconsistency of eective and rotational cross sections.

Short bio. Polina comes from Ukraine, where she received her BSc and MSc degree in applied physics from Kharkiv National University. Since her childhood she has been fascinated with science. At the university she chose plasma physics because of its wide spectrum of applications.

During her studies, she participated in summer schools and conferences, took part in organizing science festivals, and was a teacher at outreach interactive educational lectures. She also worked as a tutor of physics and mathematics for high-school students.

Polina has a strong interest in low-temperature plasmas but she is keen to learn more and become involved in the latest advances in plasma physics research.

1. Introduction

For the decades people are exploring the space, expanding horizons of knowledge. Mars is the next step of the voyage into the universe. Red planet has resources that can be used for a sustainable settlement. Using only in-situ resources (that can be found locally) will solve problems of oxygen and fuel for coming back on earth as soon as any additional launch or lander mass will increase risks to the crew and mission by reducing logistics, increasing shielding, and providing increased self-sufficiency, or reduce costs by needing less launch vehicles to complete the mission (Sanders *et al.* 2015). The main component of the atmosphere of Mars is carbon dioxide (CO_2) at 95.9% which is also an important part of our atmosphere. CO_2 can be converted directly into oxygen (O_2) and carbon monoxide (CO), witch was proposed to use in a propellant mixture in rocket vehicle (Landis & Linne 2001):

$$2\ CO_2 \rightarrow\ 2\ CO + O_2 \tag{1.1}$$

Not only Mars atmosphere is filled with carbon dioxide and monoxide, Earth's atmosphere each year suffers from bigger and bigger amounts of carbon dioxide emitted into it. Several months ago South Pole Observatory on the most remote continent in the world fixed new negative record of 400 parts per million (ppm) of carbon dioxide in the atmosphere. This means that our planet needs a practical solution of reducing of carbon dioxide emission or complete decomposition of it:

$$CO_2 \rightarrow C + O_2 \tag{1.2}$$

The complete dissociation (1.2) requires not only the decomposition (1.1), but also destruction of the carbon monoxide molecules, which is somewhat difficult because of the extremely high (11 eV) bond energy of this molecule (Rusanov *et al.* 1981). For complete model of CO_2 discharge cross sections of all products that may appear, such as CO, O, O_2 and it's ions, are needed. One of the step is to have the complete and consistent set of electron-CO cross sections. Furthermore, cross sections for electron collisions with carbon monoxide are required for modeling plasmas containing CO, such as in gas discharge lasers (Adamovich *et al.* 2002). Moreover, electron collisions with CO play an important role in the physics of space craft reentry into atmospheres of Mars and Venus (Land 1978), as well as in the study of processes occurring in those planets (Campbell *et al.* 2011) and comets (Campbell & Brunger 2009), what is also important for future space missions. Electron collisions with carbon monoxide therefore play an important role in the study of these subjects.

Most of the experimental or theoretical works are presenting only one of the cross sections or small region of the energy, e.g. low-field region. Land (1978) obtained cross sections for momentum transfer and for rotational, vibrational, and electronic excitation from an analysis of experimental data for electron drift velocity, characteristic energy, and ionization coefficient which are mostly discussed in present work. His work is based on method described by Hake & Phelps (1967), where he solves Boltzmann equation neglecting collisions of second kind. Land's set of electron collisions with carbon monoxide cross sections is one of the interests of the present work as it was not verified by author and has some missing cross sections, i.e. attachment and dissociation.

More recent work made by Itikawa (2015) collected in it previously known experimental and theoretical results for electron collisions with carbon monoxide cross sections. Itikawa compared experimental and theoretical cross sections and composed a set which is more recent and complete, as it includes dissociation and dissociative attachment. But the verification of swarm parameters as well as comparison with Land's set were not performed. His compilation is one of the largest collections of cross sections to date.

Hake & Phelps (1967) made theoretical work on rotational excitation for low energies, which should be taken into account for comparison with swarm parameters.

The aim of this article is to compare sets, made by Land and Itikawa. We want to verify those sets by calculating swarm parameters, using two-therm Boltzmann solver and propose corrections to the existing sets. The final set should be complete, i.e. all inelastic, momentum transfer and electron number changing processes should be properly described. The electron energy distribution function can be calculated in PIC or Boltzmann solver codes using a complete set. The consistency of set is defined in terms of reproducing the experimentally measured electron transport parameters. In our case the existing sets are verified by comparing the swarm parameters calculated by the two-term Boltzman solver BOLSIG+(Hagelaar & Pitchford 2005) with available experimental data on free website LXCat.net. The comparison was performed including as well rotational excitation cross sections.

The organization of the paper is as follows. The next section is devoted to the comparison of Itikawa's and Land's electron impact cross sections sets for CO. The comparison of the two-term Boltzmann calculations of the swarm parameters with the existing measurements is presented and discussed in section 3, where the importance of rotational excitations at low reduced electric fields are shown. Cross sections for rotational excitations as well as population for those states are calculated in section 4, where the final comparison and future recommendations are made.

2. The cross section set

In this section the existing electron impact cross sections set is discussed and our changes proposed. As a source of cross sections we used free to use LXCat website. There are three different sources that we used in our work: Phelps database (www.lxcat.net/Phelps), that uses carbon monoxide cross sections calculated by Land (1978), Itikawa (www.lxcat.net/Itikawa), based on review from Itikawa (2015) and Quantemol (www.lxcat.net/QUANTEMOL), although the last one has only ionization cross sections. As it was mentioned before first two are not complete or not verified with experimentally calculated swarm parameters. The Table 1 shows which cross sections given in each database.

An effective cross section, which is the sum of elastic and inelastic processes, is presented only in Phelps database. An elastic cross section does not have necessarily to be present in input file for two-term Boltzmann solver BOLSIG+, because it can be calculated automatically by subtraction from the effective all inelastic processes. Ionization cross sections are presented in each database and will be compared later. Attachment and dissociation as important processes as ionisation and excitation and will be added to our new set. One of the biggest interests in the different sets relates to the electronic excitation cross sections because of verity of different available experimental data. Phelps and Itikawa databases are using different sources (Land 1978; Itikawa 2015), both grounded on experimental measurements. In other gases previously studied Phelps' database proved to be more reliable, so it was decided to get acquainted with it and try to modify this set. In Phelps database some of the cross sections should be prolongated until 1 keV because it is a limit of our calculations and some of the experimental data that we are using. Also the $C^1\Sigma$+and $E^1\Pi$ cross sections have a similar thresholds, energy loss, and shape, and they were combined into one cross section by Land (1978), but will be separated to obtain more precise data.

	Phelps	Itikawa	Quantemol
Effective	✓		
Elastic		✓	
Ionization	✓	✓	✓
Attacment		✓	
Dissociation		✓	
Excitation	✓	✓	
Vibrational			
V1	✓	✓	
V2-V10	✓		
Electronic (threshold energy, eV)			
$A^1\Pi$	7.9	8	
$a^3\Pi$	6.2	6	
$a'^3\Sigma+$	6.8	6.8	
$b^3\Sigma+$	10.4	10.4	
$B^1\Sigma+$	not presented	10.7	
$C^1\Sigma+$	combined with	11.4	
$E^1\Pi$	$E^1\Pi$, 10.6	11.5	

Table 1: The list of available electron impact cross-sections with CO molecule with corresponding thresholds for electronic excitation

3. Swarm parameters

The possible cross sections sets were validated from the comparison of the and measured values of the electron transport parameters, which are reduced mobility μN, transverse characteristic energy D_T/μ, longitudinal characteristic energy D_L/μ and reduces Townsend effective ionization coefficient α_{eff}/N. The calculations were performed using free two-term Boltzmann solver BOLSIG+ (Hagelaar & Pitchford 2005). BOLSIG+ is an application for the numerical solution of the Boltzmann equation for electrons in weakly ionized gases in uniform electric fields, conditions which typically appear in the bulk of collisional low-temperature plasmas. Under these conditions the electron distribution is determined by the balance between electric acceleration and momentum loss and energy loss in collisions with neutral gas particles. The region of reduced electric field was from 10^{-3} to 1000 Td with exponentially growing grid and 2000 iterations. Comparison was made with available data from databases on open-access website LXCat.net (www.lxcat.net/Dutton, www.lxcat.net/LAPLACE).

The choice of growth model for electron density is important because electron swarm parameters can depend on electron density changing. Two variants are possible ”steady-state Townsend” which considered exponential growth of the density between electrodes and used to calculate reduced mobility, transverse characteristic energy and reduces Townsend effective ionization coefficient; and ”pulsed Townsend” with exponential growth of density in time and used to calculate longitudinal characteristic energy.

First, we checked the existing set. For present day the most complete set of the electron-

CO collisions that is available in LXCat is made by Phelps. For reduced field values higher than 3 Td, experimental values of the characteristic and longitudinal energies agree well with simulations performed with cross section set of Phelps. Lower this value calculated and measured values have no agreement.

The same problem was detected for mobility reduced field value around 1 Td. Replacing ionization cross section with the ones from Itikawa or Quantemol database gives difference in the calculated values less than 1%. The results obtained from the preliminary analysis of characteristic energy and mobility calculations shows that some processes for low fields are missing.

4. Rotational excitation

Hake and Phelps Hake & Phelps (1967) proposed to include rotational excitation cross sections and received good comparison for low fields with experimental data. They analysed rotational excitation process by finding effective dipole moment. The rotational cross sections were calculated by following formula:

$$\sigma_{J,J+1}(\epsilon) = \frac{(J+1)R_y\sigma_r}{(2J+1)\epsilon} ln\frac{[\epsilon^{1/2} + (\epsilon - \epsilon_J)^{1/2}]}{[\epsilon^{1/2} - (\epsilon - \epsilon_J)^{1/2}]}, \tag{4.1}$$

where $\sigma_r = 8\pi\mu^2 a_0^2/3$, μ is the electric dipole moment in units of ea_0 (in our case $4.6 \cdot 10^{-2} ea_0$), a_0 is the Bohr radius, J is the rotational quantum number of the initial state, and R_y is the Rydberg (13. 6 eV). $B_0 = 2.4 \cdot 10^{-4} eV$.

The fraction of the molecules in particular rotational state are given by formula:

$$Q_{J,J+1} = (p_J \sigma_{J,J+1}/P_r) exp[-J(J+1)B_0/kT], \tag{4.2}$$

where

$$P_r = \sum_J p_J exp[-J(J+1)B_0/kT] \tag{4.3}$$

and $p_J = (2J+1)$. Superelastic process is considered by including the inverse rotational mechanism. Calculated cross sections were added in BOLSIG+ as separate input file, i.e. we are creating the mixture of two gases: CO on a grounded state and rotational excited levels of CO.

On figure 1a transverse characteristic energy is presented. Adding the rotational excitation cross section gives comparison with experimental data within 15% for field range 0.1 - 1 Td and less than 10% for lower and higher fields. For gas temperature 300 K (1b) the differences between measurements and experiment reach 10%.

For low gas temperature 77 K population on higher levels decreasing rapidly and reaches 10^{-5} already for 16 considered levels. But for temperature of 300 K this value can be reached if 30 rotational excited levels are considered. On figure 3 presented experimental data and two types of calculations - considering 16 or 30 excited levels. For low field 0.1 Td good agreement is seen for 30 level approximation, but for 1 Td both calculations have agreement within 10%.

As it was noted before (fig. 2b) mobility has great difference with measured values for fields lower than 1 Td.

The problem of low fields can be solved by looking at effective cross sections together with rotational including a fraction of molecules in the initial rotational level Hake & Phelps (1967). On the figure 3b the problem is clearly seen. The effective and rotational cross sections are intersecting and, as effective cross section is a sum of all elastic and inelastic processes, effective cross sections should be above rotational. As far as we are

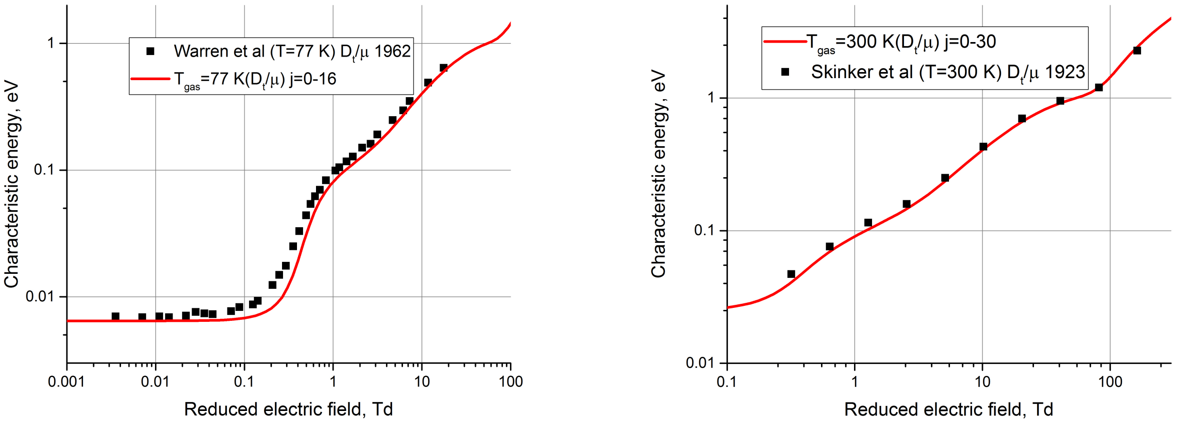

(a) (b)

Figure 1: Transverse characteristic energy (a) T_{gas}=77 K (b) T_{gas}=300 K.

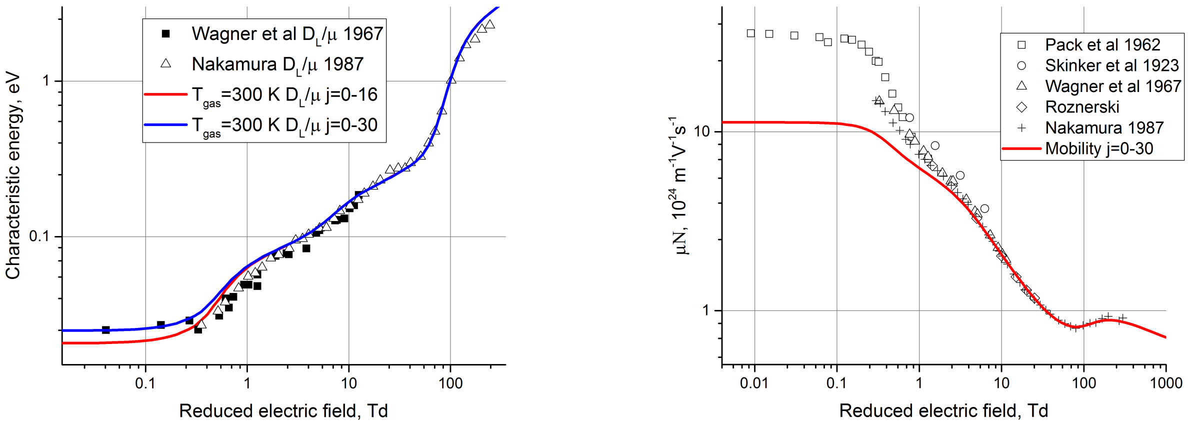

(a) (b)

Figure 2: Longitudinal characteristic energy for T_{gas}=77 K (a) and mobility (b) calculated with rotational cross sections.

not creators of Bolsig+ and we don't know how exactly it treats rotational cross sections, the possible solution of the problem could be using another solver to calculate swarm parameters. The lack of knowledge about code cannot be decided in terms of this work. Also more deep and detailed study needed to decide which of the cross sections for CO ionization and excitation in case of several possibilities (as it was in our case for Itikawa and Phelps) should be taken as defaulted.

5. Conclusions

In the presents work the existing cross sections set for carbon monoxide were studied. The cross sections sets from different databases, available online, were compared and rotational excitation as well as population for 16 and 300 levels for 77 and 300 K were calculated. This work also adresses the problem of mobility for low fields. Mostly the

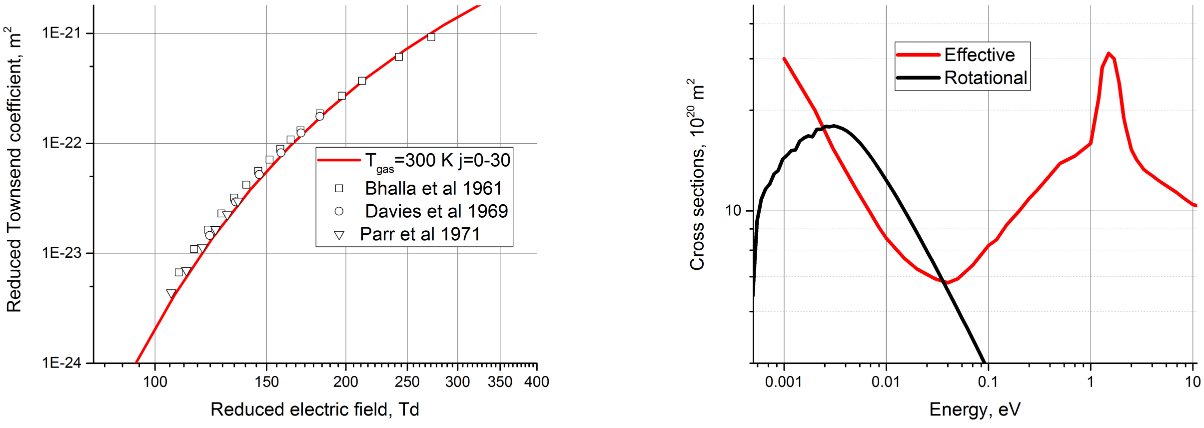

(a) (b)

Figure 3: (a) Reduced Townsend effective ionization coefficient (b) Effective and rotational cross sections

solution of the problem is lie in the understanding how does BOLSIG+ deals with mixtures of ground state gas and rotationally excited states of the same gas. This issue cannot be decided because of the limits of the code. Bolsig+ can be used for simpler systems, where such processes as rotational excitation play less important role and can be neglected. The deeper understanding of the mechanism of electron impact with CO molecule needed in order to perform the process of dissociation with minimum energy applied.

REFERENCES

Adamovich, Igor V. & others 2002 Electron-mediated vibrationelectronic (VE) energy transfer in optically pumped plasmas. *Chemical Physics* **279**, 43–54.

Campbell, L., Allan, M. & Brunger, M. J. 2011 Electron impact vibrational excitation of carbon monoxide in the upper atmospheres of mars and venus. *Geophys. Res. Lett. A09321* **116**.

Campbell, L. & Brunger, M. J. 2009 Electron impact excitation of carbon monoxide in comet hale-bopp. *Geophys. Res. Lett. L03101* **36**.

Hagelaar, G. J. M. & Pitchford, L. C. 2005 Solving the boltzmann equation to obtain electron transport coefficients and rate coefficients for fluid models. *Plasma Sources Sci. Technol.* **14**, 722–733.

Hake, R. D. & Phelps, A. V. 1967 Momentum-transfer and inelastic-collision cross sections for electrons in 0_2 co, and co_2. *Phys. rev.* **158**, 70–84.

Itikawa, Yukikazu 2015 Cross sections for electron collisions with carbon monoxide. *Journal of Physical and Chemical Reference Data* **44**, 013105.

Land, James E. 1978 Electron scattering cross sections for momentum transfer and inelastic excitation in carbon monoxide . *Journal of Applied Physics* **49**, 5716.

Landis, Geoffrey A. & Linne, Diane L. 2001 Mars rocket vehicle using in-situ propellants. *Journal of Spacecraft and Rockets* **38** (5), 730–735.

Rusanov, V. D., Fridman, A. A. & Sholin, G. V. 1981 The physics of a chemically active plasma with nonequilibrium vibrational excitation of molecules. *Sov. Phys. Usp.* **24** (6).

Sanders, Gerald B & others 2015 Mars isru for production of mission critical consumables options, recent studies, and current state of the art. *AIAA SPACE 2015 Conference and Exposition* .

Thesis list

André Lopes | Supervision team: Dr. Raúl Luís and Prof. Bruno Gonçalves

Title: Collective Thomson scattering and plasma position reflectometry systems for ITER and DEMO: neutronics performance assessment and optimisation

---

Doménica Corona | Supervision team: Prof. Horácio Fernandes and Dr. Nuno Cruz

Title: Tokamak magnetic control simulations: applications to JT-60SA and ISTTOK operation

---

Egor Seliunin | Supervision team: Prof. Carlos Silva

Title: Experimental investigation of the scrape-off layer enhanced radial transport using reflectometry diagnostics

---

Fábio Cruz | Supervision team: Prof. Luís O. Silva and Dr. Thomas Grismayer

Title: Multiscale modeling of pulsar magnetospheres

Fabrizio Del Gaudio | Supervision team: Dr. Thomas Grismayer and Prof. Luís O. Silva

Title: Numerical study of light-pair plasmas interaction mechanisms in relativistic and high-field scenarios

---

João F. Vargas | Supervision team: Prof. Mário Lino da Silva and Dr. Bruno Lopez

Title: High-Temperature Non-Equilibrium CO2 Kinetic and Radiation Processes

---

Luís Gil | Supervision team: Prof. Carlos Silva

Title: Edge instabilities across the L-H transition and in H-mode

---

Mario Galletti | Supervision team: Prof. Gonçalo Figueira and Dr. Marco Galimberti

Title: Ultrashort optical parametric oscillator up to the mid-infrared pumped by a femtosecond Ytterbium laser

---

Pedro Deus Lourenço | Supervision team: Prof. Horácio Fernandes and Dr. Jorge Santos

Title: Real-time plasma position reflectometry employing MARTe framework

---

Polina Ogloblina | Supervision team: Prof. Vasco Guerra and Prof. Luís Lemos Alves

Title: In situ resource utilization on Mars using non-equilibrium plasmas

ipfn
INSTITUTO DE PLASMAS
E FUSÃO NUCLEAR

FCT
Fundação para a Ciência e a Tecnologia
MINISTÉRIO DA CIÊNCIA, TECNOLOGIA E ENSINO SUPERIOR

PD F
FCT PhD
PROGRAMMES

TÉCNICO
LISBOA

U LISBOA
UNIVERSIDADE
DE LISBOA